
UNIVERSITÀ
degli STUDI
di CATANIA

Dipartimento
di Fisica
e Astronomia
*"Ettore Majorana"*

PhD programme in physics

---

Giorgio Finocchiaro

# X-ray imaging and spectroscopy of space- and time-dependent phenomena in magnetically confined plasma

PhD thesis

Supervisors:
Prof. F. Rizzo
Prof. D. Mascali

Co-Supervisors:
Dr. E. Naselli
Dr. A. Pidatella

---

academic year 2025/2026

# Contents

# Introduction

The physics of Electron Cyclotron Resonance (ECR) laboratory plasmas represents a complex and multidisciplinary field, combining aspects of atomic and nuclear physics, astrophysics, and advanced technology.

Such plasmas offer a wide range of applications, ranging from ion sources for particle accelerators to fundamental investigations of plasma dynamics under conditions of astrophysical relevance. In particular, the study of ECR plasmas provides a unique opportunity to reproduce, within a controlled laboratory environment, some of the mechanisms governing highly ionized matter in both terrestrial and cosmic scenarios.

Within this framework, the **PANDORA** (**P**lasmas for **A**strophysics, **N**uclear **D**ecays **O**bservation and **R**adiation for **A**rchaeometry) project has been conceived with the ambitious goal of employing ECR plasmas as an experimental environment for innovative experiments in nuclear physics and nuclear astrophysics.

The main objective of the project is to investigate $\beta$-decay physics in ionized media, mimicking specific conditions of astrophysical importance that cannot be reproduced through conventional approaches.

To this aim, the project foresees the construction of the homonymous plasma research facility at INFN-LNS. This facility will be based on a magnetically confined ECR ion source (ECRIS), uniquely designed to enable the observation and characterization of the plasma through a wide variety of diagnostic systems.

Plasma diagnostics, in particular, play a crucial role in the PANDORA context. Access to a broad set of intrinsic plasma observables is indeed

the key to ensuring an experimental environment where both the electromagnetic and thermodynamic properties of the plasma can be precisely monitored and controlled.

This capability ensures the reproducibility of experimental conditions and provides a basis for new insights into the interplay between nuclear processes and plasma physics, bridging the gap between laboratory experiments and astrophysical phenomena.

Within the PANDORA framework, this thesis is specifically focused on the development and application of advanced diagnostic systems, in accordance with the stringent requirements for plasma monitoring and characterization.

The complete and reliable reconstruction of plasma thermodynamics, in fact, cannot rely solely on conventional approaches, but rather requires space-resolved techniques.

X-ray diagnostics are particularly valuable, as they provide non-invasive access to the plasma dynamics. In this respect, a dedicated method for the application of X-ray pinhole camera imaging has been developed within the present work, representing a central element of the thesis.

Nevertheless, these techniques must be extended beyond their current capabilities, since a reliable monitoring of PANDORA plasmas will be mandatory under gas-mixing conditions, which are expected to represent the standard operational regime of the experiment.

The physics cases of PANDORA, in fact, rely with high mass isotopes (Nb, Cs, Lu) which will be injected after their vaporization inside a buffer plasma made of oxygen or argon. Hence, typical operations of PANDORA will deal with a mixture of species in the same plasma, whose dynamics of ionization and spatial distribution are needed to be known, as precisely as possible, by appropriate diagnostics techniques.

In addition to spatial resolution, temporal dynamics are equally crucial. Fast transients, such as afterglow decay and kinetic instabilities, play a central role in ECR plasma behavior, yet remain poorly understood and thus insufficiently exploited to improve device performance in terms of extracted current and charge state distribution. Their investigation calls for dedicated adaptations of both the diagnostic setup and the associated data analysis techniques.

Beyond their immediate relevance for the success of PANDORA, these

studies bear a broader scientific impact. Gas mixing, transient decay phenomena, and instabilities represent long-standing open issues in the context of ECR ion sources, and their systematic investigation has the potential to deepen our understanding of plasma confinement and to suggest new routes for optimization.

Against this background, the present thesis is devoted to addressing these open questions by building up a robust diagnostic methodology based on space- and energy-resolved X-ray measurements. This approach provides unique access to bremsstrahlung and fluorescence plasma emission, enabling the probing of plasma confinement structures under different operational regimes.

Several experimental campaigns have been carried out for this purpose at the 14 GHz ECR ion source facility (Atomki, Debrecen, Hungary) between 2018 and 2024.

Through these campaigns, the effects of gas mixing and afterglow transients in pulsed plasmas have been systematically investigated. Furthermore, the proposed diagnostic method has proven to be an insightful tool to explore the spatial and energetic distribution of plasma, allowing for the reconstruction of local values of warm electron density and temperature.

This thesis will particularly report on the preparation, testbench measurements and then direct ECR plasma characterization in Atomki, performed during the experimental campaign of November 2024 in Hungary, including the data analysis and interpretation that, in addition to the present thesis, is now under preparation for several papers that will be submitted to high impact factor journals.

These results mark a significant step toward establishing a diagnostic standard that will be mandatory to achieve PANDORA's overarching goal: the study of nuclear processes in a fully controlled plasma environment.

The contents of the thesis are divided into five chapters, arranged according to the following structure: Chapter 1 introduces the principles of plasma physics, with a main focus on the mechanisms governing the dynamics of plasmas confined in magnetic traps and excited by electromagnetic waves. The chapter then presents the fundamentals of plasma

self-emission, whose observation provides the basis for the application of the aforementioned diagnostic methods.

Chapter 2 addresses the experimental aspects of ECR sources, providing a comprehensive overview based on the most recent literature. An introduction to ECR sources is first provided, followed by a description of the well-established diagnostic systems, and then the main aspects of the PANDORA project are presented.

The chapter also frames the techniques for measuring the thermodynamic parameters of plasmas, a key component of plasma diagnostics, and concludes by highlighting the open issues concerning ECR plasma dynamics, which form the foundation of the experimental work described in this thesis. The primary experimental goals are outlined at the end of the chapter.

Chapter 3 describes the experimental methodology, focusing specifically on the energy-resolved X-ray pinhole camera technique as an imaging diagnostic.

A detailed characterization of the diagnostic system is presented, together with the Single Photon Counting (SPhC) analysis technique that enables the extraction and calibration of the energy information from the CCD images.

Chapter 4 focuses on the experimental setup for applying the technique to the ECRIS facility at the Atomki ECR laboratory. All relevant aspects of the facility are described, including the peculiarities of the plasmas produced and confined therein, as well as the detailed configuration of the pinhole camera measurement system.

Finally, Chapter 5, reporting the main and original outcomes and contributions of this thesis, presents space- and time-resolved measurements of the previously outlined physical scenarios, carried out using the experimental methods and apparatus described in the preceding chapters.

The chapter is organized into three main sections, each focusing on a specific type of measurement: investigations of gas-mixing effects, time-resolved studies of pulsed plasma transients, and the application of the developed method for reconstructing local thermodynamic parameters. Each section is further subdivided into three subsections, which cover: the experimental configuration, the results, and the discussion, the latter including a comparison with the relevant literature.

Before presenting the scientific content, it is important to highlight that the diagnostic techniques described in this thesis are the outcome of several years of collaborative effort by the entire research team, on which significant developments represents original contributions of this work.

Key developments reported in this thesis include the refinement of the X-ray imaging technique, including the enhancement of energy-resolved analysis for space- and time-resolved measurements, and the procedures for reconstructing local thermodynamic parameters of the plasma.

The application of these techniques provides valuable insights into the physical mechanisms governing plasma dynamics and offers benchmark results that can support the synergistic development and validation of theoretical and computational plasma models.

Chapter 1

# Introduction to plasma physics

Known as the *fourth state of matter*, plasma constitutes the 98% of visible matter in the Universe.

It is defined as a quasi-neutral ionized gas which exhibits collective behaviours, independent on local conditions. Consequently, a relevant number of atoms in a plasma has to be ionized.

The quasi-neutrality condition indicates the property of a plasma to be globally "neutral." The Debye length is then defined, which indicates the distance beyond which the field produced by a charged particle is effectively screened by the other particles. Its expression is as follows:

$$\lambda_D = \frac{\epsilon_0 k_B T_e}{n_e e^2} \tag{1.1}$$

where $\epsilon_0$ is the vacuum permittivity, $k_B$ the Boltzmann constant, and $e$ the electron charge.

At distances on the order of $\sim 5\lambda_D$, the electrostatic potential generated by a single charge is effectively screened.

Accordingly, a plasma differs from an ordinary ionized gas when its characteristic size satisfies $L \gg \lambda_D$. Under these conditions, the bulk of the plasma is largely unaffected by external electric fields.

An additional consequence is that, within a plasma, the ion density is nearly equal to the electron density.

The concept of temperature in a plasma is a delicate matter: thermodynamic equilibrium can be approximately reached between particles of

the same type (electrons or ions), because of the different collisionality in relation of the huge mass difference. This carries to the definition of different temperatures for the respective particle species.

When a plasma is magnetized, also the same particle species can be affected by a split of thermodynamic conditions that become anisotropic. In fact the responsible mechanism of thermalization can be somehow limited by the interaction of plasma with magnetic field, bringing to the definition of a parallel and an orthogonal temperature $T_{\parallel}$, $T_{\perp}$ relatively to the B-filed direction $\vec{B}$.

Supposing to have thermodynamic equilibrium conditions, the state of ionization due to thermal effects can be generally described by Saha equation [1]:

$$\frac{n_i n_e}{n_n} = \frac{2(2\pi m_e k_B T)^{\frac{3}{2}}}{h^3} e^{-\frac{E_i}{k_B T}} \tag{1.2}$$

where $n_i$, $n_e$, $n_n$ are, respectively, the density of ions, electrons and neutrals; $m_e$ is the mass of the electron, $E_i$ the ionization energy, $T$ is the temperature, $k_B$ the Boltzmann constant and $h$ the Planck's constant.

This ratio is very low for a room temperature gas ($T \sim 300\ K$), and it is the reason why the plasma state in the earth is extremely rare. Whilst, in a plasma it can reach a vast spectrum of values, depending on the temperature. Typical plasma electron densities and temperatures span a very large scale, with temperature differences of up to 7 orders of magnitude and even up to 25 orders of magnitude for densities, as summarized in table 1.1.

| | $n_e[m^{-3}]$ | $T_e[keV]$ |
|---|---|---|
| Fusion plasmas (magnetic confinement) | $\sim 10^{20}$ | $\sim 10$ |
| Fusion plasmas (inertial confinement) | $\sim 10^{31}$ | $\sim 10$ |
| Solar wind | $\sim 5 \cdot 10^{6}$ | $\sim 0.2$ |
| Earth ionosphere | $\sim 5 \cdot 10^{12}$ | $\sim 10^{-4}$ |
| ECRIS plasmas | $\sim 10^{17} - 10^{19}$ | $\sim 0.1 - 100$ |

Table 1.1: Typical plasma electron density and temperature scales

The present work is focused on ECR (Electron Cyclotron Resonance) laboratory plasmas, obtained in compact magnetic traps by exciting low-

pressured gases ($\sim 10^{-5} - 10^{-2} mbar$), with typical densities and temperatures of the order of $n_e \sim 10^{17} - 10^{19} m^{-3}$, $T_e \sim 0.1 - 100\ keV$.

These devices have been historically employed as particle accelerators' injector, the so-called ECR Ion Sources, making the production of multicharged ion beams possible.

Very recently, these systems have been re-designed and conceived as plasma-based research infrastructures paving the way for novel interdisciplinary studies in nuclear and atomic physics. Details about the ECRIS and ECR-plasma based infrastructures will be given in the section 2.1.

The role of magnetic field in ECR plasmas is relevant since it determines the confinement conditions and the electromagnetic resonances, responsible of the ignition.

Another relevant parameter in an ECR plasma is the confinement time $\tau_c$, which determines the probability of a multiple ionization and thermalization of the ions before being neutralized. This can usually vary in the range of $10^{-5} - 10^{-3}$ seconds.

The behavior of a plasma is described by magnetohydrodynamics, the branch of knowledge which deals with all the properties of such fluids that respond to the electromagnetism and kinematics laws.

In the following, more details will be provided on the electromagnetic coupling of charged particles to plasma along with a description of their magnetic and collisional confinement mechanisms.

## 1.1 Motion of a charged particle in a magnetized plasma

The first aspects of an electromagnetic system are the kinematics and dynamics of a free electric particle [2].

Although being a strong simplification, the free electric particle physics is a helpful step to understand the behavior of a plasma.

The motion is governed by the Lorentz force, generated by the external magnetic field:

$$\vec{F} = q\vec{v} \times \vec{B} \tag{1.3}$$

where $q$ is the electric charge, $\vec{v}$ the velocity and $\vec{B}$ the external magnetic

field.

By a proper choice of the coordinate system ($|\vec{B}| \equiv B_z$), it's easy to show that the resulting motion is uniform circular along the directions perpendicular to the magnetic field $\vec{B}$. By decomposing the vector equation into the three components we obtain the following system of three equations:

$$\begin{aligned} \dot{v}_x &= \frac{qB}{m} v_y \\ \dot{v}_y &= -\frac{qB}{m} v_x \\ \dot{v}_z &= 0 \end{aligned} \tag{1.4}$$

which highlights that $v_z$ is a constant of motion.

The pulsation of the circular motion is defined *cyclotron frequency*:

$$\omega_c = \frac{|q|B}{m} \tag{1.5}$$

with a radius equal to the *Larmor radius*, defined by:

$$R_L = \frac{v_{0\perp}}{\omega_c} = \frac{m v_{0\perp}}{qB} \tag{1.6}$$

The resulting motion of a particle with an initial velocity $v_0$ is helicoidal along the direction of $\vec{B}$, as $v_z$ is a constant of the motion (see figure 1.1). It is in fact given by the composition of a uniform rectilinear motion along the direction of the magnetic field, and of a uniform circular motion on the xy plane orthogonal to the field.

The particle results to be confined along the directions perpendicular to the $\vec{B}$ field.

**Drift motions** A component of the motion, perpendicular to the $\vec{B}$ field line can occurr in presence of an external **electric field**, a **gradient** or a **curvature** of the $\vec{B}$ field lines.

The first case is exampled in the beam extraction from ECRIS, where an extraction voltage is applied in order to extract the ion content of the plasma to be accelerated.

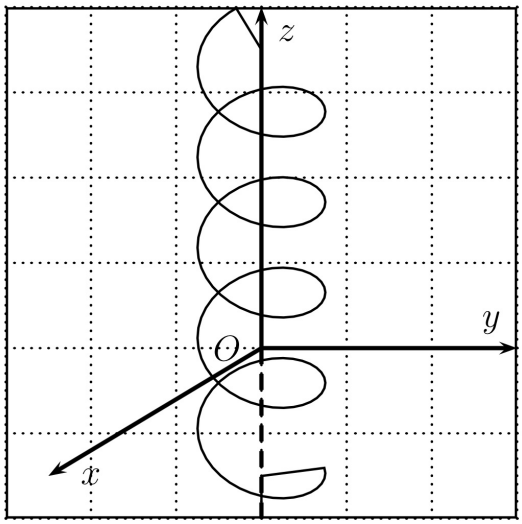


Figure 1.1: Helicoidal motion of a charged particle into an external magnetic field $B_z$

In presence of an **electric field** $\vec{E}$, the motion equation becomes:

$$m\frac{d\vec{v}}{dt} = q\left(\vec{E} + \vec{v} \times \vec{B}\right) \tag{1.7}$$

whose component along the $\vec{B}$ direction is:

$$\dot{v}_z = \frac{q}{m}E_z \tag{1.8}$$

The drift motion $\vec{v_E}$, perpendicular to the magnetic field, is independent on the electric charge and is described by [1]:

$$\vec{v_E} = \frac{\vec{E} \times \vec{B}}{B^2} \tag{1.9}$$

The case of a **magnetic gradient** can be exemplified by a gradient perpendicular to the $\vec{B}$ field:

$$\nabla B \perp \vec{B} \tag{1.10}$$

which determines a gradient of the Larmor radius $R_L$.

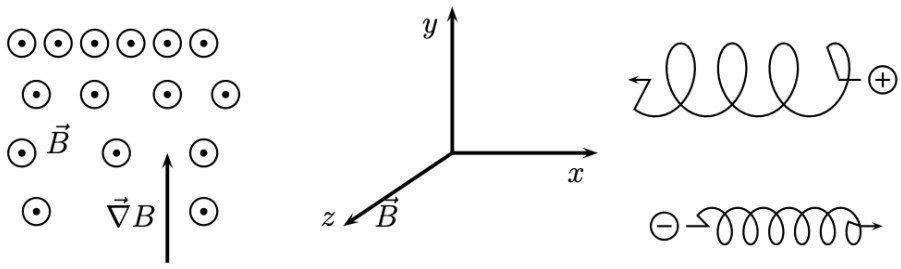


Figure 1.2: Sketch showing the drift motion of an electric charge in a magnetic field gradient $\nabla B \perp \vec{B}$

The resulting motion, described in figure 1.2, is affected by a non-uniformity of the helicoidal motion that determines a drift perpendicular to the gradient.

The **gradient drift velocity** $\vec{v}_{\nabla B}$ is described by the equation:

$$\vec{v}_{\nabla B} = \pm\frac{1}{2} v_{\perp} R_L \frac{\vec{B} \times \nabla B}{B^2} \tag{1.11}$$

The $\pm$ sign is related to the electric charge: opposite charges have opposite drift directions.

In presence of a magnetic field, a **curvature drift motion** takes place. It can be described by considering the average centrifugal force $\vec{F}_c = m v_{\parallel}^2 \frac{\vec{R}_C}{R_C^2}$ of a particle in its helicoidal motion around a curved B-field line.

Applying the expression of the drift velocity $\vec{v}_f$ of a generic force $\vec{F}$:

$$\vec{v}_f = \frac{1}{q} \frac{\vec{F} \times \vec{B}}{B^2} \tag{1.12}$$

the resulting curvature drift velocity $\vec{v}_R$ in a field line of curvature $R_C$ would be:

$$\vec{v}_R = \frac{1}{q} \frac{\vec{F}_c \times \vec{B}}{B^2} = \frac{m v_{\parallel}^2}{q B^2} \frac{\vec{R}_C \times \vec{B}}{R_C^2} \tag{1.13}$$

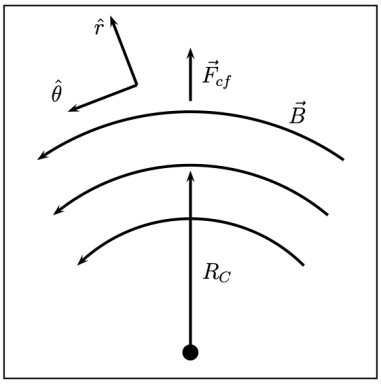


Figure 1.3: Sketch of the drift motion of an electric charge in a curved magnetic field

## 1.2 Magnetic confinement of a plasma

Having defined the drift motions of particles in different magnetic field conditions, it is possible to show how these phenomena can determine the confinement of a plasma.

The easiest case is exemplified by a magnetic gradient parallel to the magnetic field:

$$\nabla B \parallel \vec{B} \tag{1.14}$$

The **simple mirror** configuration provides an axial symmetry with a radial component of magnetic field, as shown in figure 1.4.

Such a configuration can be obtained by a pair of solenoids faced axially in front of each others, with a concordant electric current inside.

All the components of $\vec{B}$ satisfy the Maxwell equation $\vec{\nabla} \cdot \vec{B} = 0$.

In cylindrical coordinates:

$$\frac{1}{r}\frac{\partial}{\partial r}(rB_r) + \frac{\partial B_z}{\partial z} = 0 \tag{1.15}$$

Neglecting the dependence of $\frac{\partial B_z}{\partial z}$ on $r$, the following expression is obtained:

$$B_r = -\frac{1}{2} r \left[\frac{\partial B_z}{\partial z}\right]_{r=0} \tag{1.16}$$

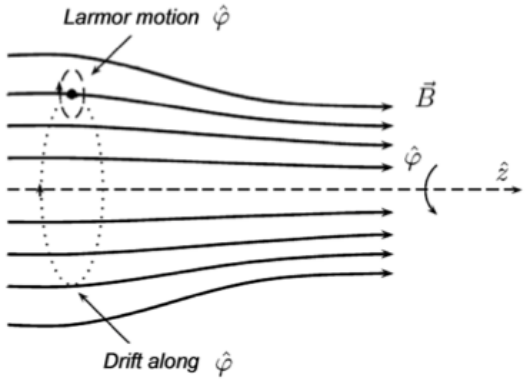


Figure 1.4: Motion of an electric charge in a simple mirror magnetic configuration

The radial gradient $\frac{\partial}{\partial r}(rB_r)$ causes a gradient-drift motion (figure 1.2) around $z$ axis.

The only force acting on the particle is the Lorentz force, whose components are:

$$\begin{aligned} F_r &= q(v_\varphi B_z - v_z B_\varphi) \\ F_\varphi &= q(-v_r B_z + v_z B_r) \\ F_z &= q(v_r B_\varphi - v_\varphi B_r) \end{aligned} \tag{1.17}$$

Considering that $B_\varphi = 0$, the components $F_r$ and $F_\varphi$ describe the Larmor motion, while the $F_z$ component is responsible of the magnetic reflection:

$$F_z = -qv_\varphi B_r = \frac{1}{2} qv_\varphi r \left( \frac{\partial B_z}{\partial z} \right) \tag{1.18}$$

The average on a Larmor gyro-period allows to define a magnetic moment for the charged particle:

$$\mu = \frac{1}{2} \frac{mv_\perp^2}{B} \tag{1.19}$$

so the force along $z$ can be written in a more general expression:

$$F_z = \mu \left( \frac{\partial B}{\partial z} \right) \tag{1.20}$$

This approximation is valid in the conditions of $R_L << L$: the Larmor radius is negligible in respect of the variation length of the magnetic field.

The magnetic mirror can be resumed by the following explanation: magnetic field can't do mechanical work, so the kinetic energy of particles is conserved. The Larmor motion along perpendicular axes takes places at the expense of the kinetic energy along the parallel axis, in respect of $\vec{B}$, consequently when $v_\perp$ increases $v_\parallel$ decreases.

This phenomenon carries to the inversion of the motion along $z$, determining the magnetic reflection.

**The loss cone** The confinement of particles by means of a magnetic bottle depends on the so called loss cone aperture [3]. As the effect of the magnetic mirror depends on the initial $v_\perp$, a particle with an initial velocity parallel to the magnetic field doesn't feel the mirror effect.

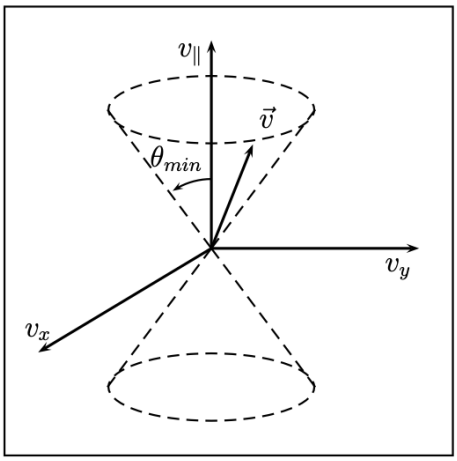


Figure 1.5: Schematic representation of the loss cone in the velocity space; $\theta_{min}$ indicates the cone aperture, the angle between $v^2_{\parallel 0}$ and $v_0$

The conditions for which the reflection can happen can be derived by the conservation of $\mu$, considering $B_0$ and $v_{\perp 0}$ the conditions far from the reflection, $B_{refl}$ and $v_{\perp refl}$ the ones at the reflection point:

$$\mu = \frac{1}{2}\frac{m v^2_{\perp 0}}{B_0} = \frac{1}{2}\frac{m v^2_{\perp refl}}{B_{refl}} \tag{1.21}$$

For the energy conservation:

$$v^2_{\perp refl} = v^2_{\perp 0} + v^2_{\parallel 0} = v^2_0 \tag{1.22}$$

consequently:

$$\frac{B_0}{B_{refl}} = \frac{v^2_{\perp 0}}{v^2_{\perp refl}} = \frac{v^2_{\perp 0}}{v_0} \equiv sin^2\theta_0 \tag{1.23}$$

If $B_m$ is the maximum value of the magnetic field, the condition for a reflection is that:

$$sin^2\theta_0 > \frac{B_0}{B_m} \equiv \frac{1}{R_m} \tag{1.24}$$

where $R_m$ is defined as **mirror ratio**.

By the equation 1.24 it is possible to determine the so called loss cone: i.e., the region in the velocity space ($\theta < \theta_{min}$) where particles that cannot be mirrored lie. The figure 1.5 shows a schematic representation of the loss cone shape in the velocity space. Below a minimum angle $\theta_{min}$ particles can't be confined by a magnetic mirror. We generally refer to them as "deconfinement losses".

### 1.2.1 Plasma confinement in magnetic traps

The **simple mirror** configuration in a typical cylindrical plasma trap can be obtained by a pair of solenoids generating a magnetic mirror on each side, as shown in figure 1.6. Plasma is confined in the middle part of the chamber and is reflected by the mirrors as explained before.

The confinement resulting from this configuration has some critical aspects: curvature drift motions (1.3) across magnetic field lines determine a radial loss in the middle plane, in addition, the thermal collisions continuously populate the *loss cone* (1.5), determining also an axial loss and a thermodynamic anisotropy in the velocity space called *loss cone instability*. Plasma results to be only partially confined, with a very short lifetime.

A more efficient magnetic configuration is called ***B-minimum***, obtained by the superposition of two magnetic systems:

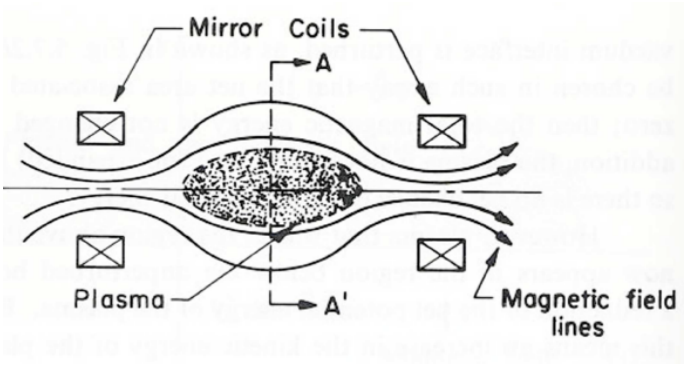


Figure 1.6: Simple mirror configuration of a plasma trap: magnetic field is generated by two solenoids.

- A pair of solenoids generating a *simple mirror* field, thus an axial confinement.
- An *hexapole* that surrounds the chamber, generating a radial field.

Figure 1.7 shows a sketch of the magnetic system for the B-minimum configuration, with magnetic hexapole and two coils, surrounding the plasma volume. This determines a magnetic gradient in every direction: the axial gradient by the simple mirror combined with the radial one from the hexapole.

The resulting magnetic field has a minimum in the center of the volume, which causes a better plasma confinement and an isotropic (local) thermodynamic equilibrium.

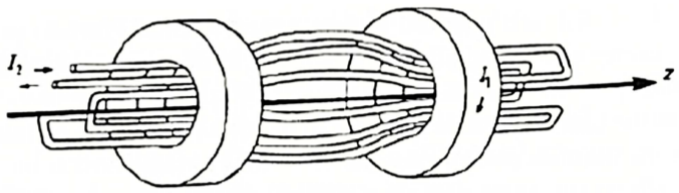


Figure 1.7: B-minimum configuration with the magnetic hexapole surrounding the plasma volume.

## 1.3 Propagation of waves in plasma

Wave propagation in plasmas is a fundamental topic in this study, being closely related to the generation and *heating* processes of the plasma itself.

One distinguishes between externally-launched waves and **self-generated** waves. Typically, plasma is generated through the direct interaction of plasma electrons with electromagnetic (EM) waves in the **microwave** range. Under suitable conditions, however, EM waves can generate electrostatic waves, which subsequently interact with the plasma particles, leading to heating.

The following sections describe the mechanisms that allow the propagation of these waves and the processes through which they transfer energy to the plasma.

### 1.3.1 Plasma oscillations and ion waves

A plasma can be seen as a collection of coupled **harmonic oscillators**. Since it consists of unbound charges of opposite signs, such as ions and electrons, the main form of oscillation can be modeled as an electric multipole.

Considering only the motion of **electrons** against the positive background of **ions**, the electric force between opposite charges causes an oscillatory motion whose characteristic angular frequency $\omega_p$ is called the **plasma frequency**:

$$\omega_p = \left( \frac{ne^2}{\epsilon_0 m} \right)^{1/2} \tag{1.25}$$

where $n$ is the electron density, and $e$ and $m$ are the electron charge and mass, respectively.

In this expression, the wave number $k$ does not appear, and the group velocity $v_g = \frac{d\omega}{dk}$ is therefore zero, so no wave propagation occurs.

The situation changes when **thermal motions** are present, which influence the characteristic frequency as:

$$\omega^2 = \omega_p^2 + \frac{3}{2} k^2 v_{th}^2 \tag{1.26}$$

called the **Langmuir frequency**, where $v_{th}$ is the thermal velocity.

Equation (1.26) includes a dependence on $k$, allowing the **propagation** of plasma oscillations.

**Ions** behave similarly, so thermal motions also enable the propagation of *Ion Waves*. These are analogous to acoustic waves as **pressure waves**, but unlike in a neutral gas where propagation occurs via molecular collisions, in a plasma ions transmit oscillations through their electric fields.

The **dispersion relation** for these waves is:

$$\frac{\omega}{k} = \left( \frac{KT_e + \gamma_i KT_i}{m_i} \right)^{1/2} \tag{1.27}$$

### 1.3.2 Electromagnetic waves in a magnetized plasma

Electromagnetic waves interact with all components of a medium. In plasmas, composed of **ionized** and **neutral** matter, wave propagation is mainly influenced by the ionized component, making interactions with neutrals negligible [2].

A magnetized plasma is **anisotropic**, and the **dielectric constant** $\epsilon_0$ becomes a **tensor quantity**.

The equation of motion of an electron in a **magnetized cavity** traversed by an **EM wave** is:

$$m_e \frac{d\vec{v}}{dt} = q_e \vec{E} + q_e \vec{v} \times \vec{B}_0 \tag{1.28}$$

Neglecting the Lorentz force due to the magnetic component of the EM wave in the non-relativistic limit ($v/c << 1$) and defining the **cyclotron frequency** $\omega_c$, the motion becomes:

$$\frac{d\vec{v}}{dt} = \frac{q_e \vec{E}}{m_e} + \omega_c \vec{v} \times \vec{z} \tag{1.29}$$

Assuming harmonic fields $\vec{E} = \vec{E}_0 e^{-i\omega t}$ and $\vec{v} = \vec{v}_0 e^{-i\omega t}$, one obtains:

$$-i\omega \vec{v} + \omega_c \vec{z} \times \vec{v} = \frac{q_e \vec{E}}{m_e} \tag{1.30}$$

Solving for components $v_x, v_y, v_z$, one finds the **current density vector** $\vec{J} = n q_e \vec{v}$, which is not parallel to the **electric field** $\vec{E}$. From Maxwell's

equations:

$$\vec{\nabla} \times \vec{H} = \vec{J} - i\omega\epsilon_0\vec{E} = -i\omega\overline{\overline{\epsilon}} \cdot \vec{E} = -i\omega\vec{D} \tag{1.31}$$

Thus, the **electric displacement** $\vec{D}$ is related to $\vec{E}$ by the **dielectric tensor**:

$$\vec{D} = \overline{\overline{\epsilon}} \cdot \vec{E} \tag{1.32}$$

In components:

$$\begin{aligned} D_x &= \epsilon_0 \left(1 - \frac{\omega_p^2}{\omega^2 - \omega_c^2}\right) E_x - i\epsilon_0 \frac{\omega_p^2 \omega_c}{\omega(\omega^2 - \omega_c^2)} E_y \\ D_y &= i\epsilon_0 \frac{\omega_p^2 \omega_c}{\omega(\omega^2 - \omega_c^2)} E_x + \epsilon_0 \left(1 - \frac{\omega_p^2}{\omega^2 - \omega_c^2}\right) E_y \\ D_z &= \epsilon_0 \left(1 - \frac{\omega_p^2}{\omega^2}\right) E_z \end{aligned} \tag{1.33}$$

The resulting dielectric tensor $\overline{\overline{\epsilon}}$ makes the plasma **birefringent**, splitting an incident EM wave into **ordinary** and **extraordinary** waves, each with different propagation constants $k$.

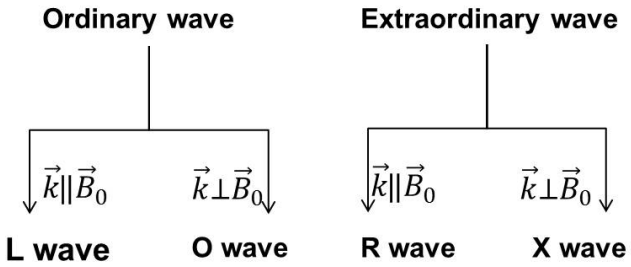


Figure 1.8: Schematic of waves propagating in plasma

Figure 1.8 shows cases where $\vec{k}$ is parallel or perpendicular to $\vec{B}_0$, highlighting the different polarizations of ordinary and extraordinary waves. Waves **L** and **R** have circular polarization along $\vec{B}_0$, while **O** and **X** are classified based on the orientation of the oscillating electric field relative to $\vec{B}_0$.

### 1.3.3 Resonances and Cut-offs

A wave exhibits a *resonance* when the medium's refractive index tends to infinity, while a *cut-off* occurs when it tends to zero. In a resonance, energy is transferred from the wave to electrons or other plasma oscillations; in cut-off, the wave is fully reflected.

Resonances are induced by an external magnetic field, whereas cut-offs also exist in unmagnetized plasmas. This is why magnetized plasmas allow more effective electron heating: resonances favor energy transfer from the EM wave to the plasma.

| Vector orientation | Refractive index $\eta^2$ | Wave type |
|---|---|---|
| $\vec{k} \parallel \vec{B}_0$ | $\eta^2 = 1 - \frac{\omega_p^2/\omega^2}{1+(\omega_c/\omega)}$ | L-wave |
| $\vec{k} \perp \vec{B}_0, \vec{E} \parallel \vec{B}_0$ | $\eta^2 = 1 - \frac{\omega_p^2}{\omega^2}$ | O-wave |
| $\vec{k} \parallel \vec{B}_0$ | $\eta^2 = 1 - \frac{\omega_p^2/\omega^2}{1-(\omega_c/\omega)}$ | R-wave |
| $\vec{k} \perp \vec{B}_0, \vec{E} \perp \vec{B}_0$ | $\eta^2 = 1 - \frac{\omega_p^2}{\omega^2}\frac{\omega^2-\omega_p^2}{\omega^2-\omega_h^2}$ | X-wave |

Table 1.2: Cut-offs and resonances of different wave types [3]

Ordinary waves (L, O) do not exhibit resonances. Extraordinary waves (R, X) resonate when:

- R-wave: $\omega = \omega_c$ (Electron Cyclotron Resonance, ECR)
- X-wave: $\omega^2 = \omega_c^2 + \omega_p^2 = \omega_h^2$ (Upper Hybrid Resonance, UHR)

Intermediate angles generate hybrid ECR-UHR oscillations. Cut-offs for X-wave are:

$$\begin{aligned} \omega_L &= \frac{1}{2}\left(\omega_c + \sqrt{\omega_c^2 + 4\omega_p^2}\right) \\ \omega_R &= \frac{1}{2}\left(-\omega_c + \sqrt{\omega_c^2 + 4\omega_p^2}\right) \end{aligned} \tag{1.34}$$

The CMA diagram 1.9 shows regions of plasma where resonances and cut-offs occur. $\omega_p^2/\omega^2 \propto n_e$ (electron density), $\omega_c/\omega \propto B$. Densities above the O-wave cut-off (overdense plasma) reflect the wave. Regions of ECR and UHR are indicated, as well as the R- and L-cutoffs for the X-wave.

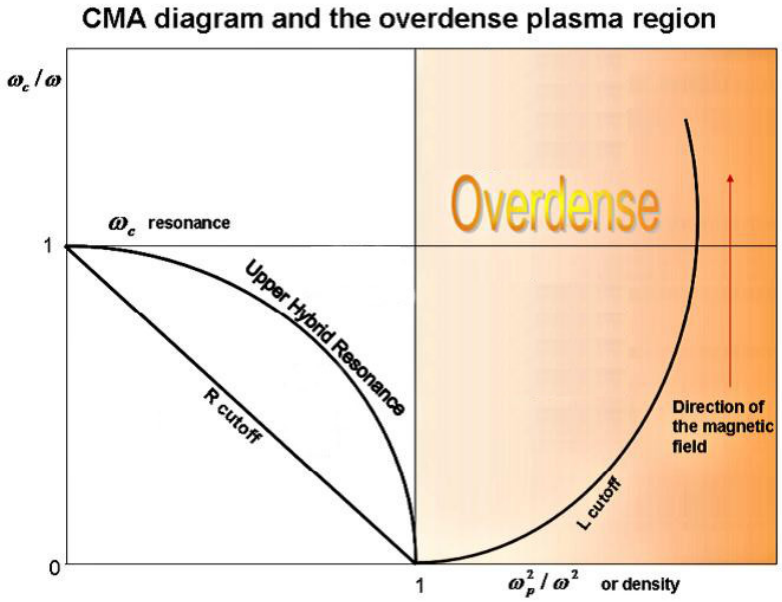


Figure 1.9: Clemmon-Mullaly-Allis (CMA) diagram [3]

### 1.3.4 The Electron Cyclotron Resonance

The cyclotron frequency introduced in section 1.1, results to be a resonant condition for a plasma, which can determine the energy absorption from a properly tuned electromagnetic wave [4].

The collisionality of a plasma particles determines the thermalization of the absorbed energy, causing the effective plasma heating.

In a magnetic trap, this phenomenon happens in a specific region called *ECR surface*, consisting on the magnetic isosurface that satisfies the resonant condition:

$$B_{ECR} = \frac{m_e \omega_{RF}}{|q|} \tag{1.35}$$

where $m_e$ and $q$ are respectively the mass and the charge of the electron, and $\omega_{RF}$ is the frequency of the incident EM wave. The width of the absorption law determines the thickness of this surface, which consequently results to be a thin layer with a volume $> 0$.

## 1.4 X-ray emission of a plasma

A plasma emits electromagnetic radiation over a broad spectral range, from the visible domain up to hard X-rays. In particular, the electronic component of the plasma is responsible for a significant fraction of the emission in the X-ray regime, typically spanning from a few keV up to several hundreds of keV.

The study of this spectral range is of particular interest, as X-ray radiation provides access to fundamental information on the plasma structure and dynamics, offering diagnostic capabilities that are not attainable through other regions of the electromagnetic spectrum.

The ECR plasma is typically characterized by non-LTE (Local Thermodynamic Equilibrium) conditions, because of the low density. In these conditions, the typical Electron Energy Distribution Function consists of three different electron populations that can be defined as *hot* ($> 30\ keV$), *warm* ($1 - 30\ keV$) and *cold* ($0 - 1\ keV$), sketched in figure 1.10. This affects the electromagnetic emission phenomena, which are strictly related to the energy distribution of electrons.

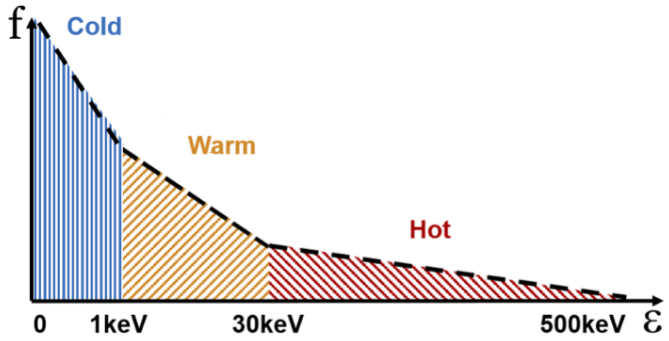


Figure 1.10: Non-LTE electron energy distribution: three main electron populations are defined - *hot* ($> 30\ keV$), *warm* ($1 - 30\ keV$) and *cold* ($0 - 1\ keV$).

The emission takes place by three main mechanisms:

- The Bremsstrahlung emission
- The atomic recombination

- The characteristic fluorescence emission

The first one is a *free-to-free* process, mainly dominated by the scattering of electrons into the electric fields of ions, generating a continuous spectrum which contains physical information about thermodynamics of plasma. The second one is a *free-to-bound* process, that involves both electrons and ions. The resulting spectrum is continuous but the mechanism is not dominant for high temperature plasmas. The third mechanism is the photon emission of specific wavelengths in *bound-to-bound* atomic radiative processes. The information revealed by the study of this phenomenon can show properties of both free electrons energy distribution and ions spatial distribution.

### 1.4.1 Bremsstrahlung electron emission

The Bremsstrahlung phenomenon takes place when an electric charge accelerates. In a plasma, this happens because of the thermal motion of electrons, which continuously scatter with other electrons or ions. The effect of ion-ion scattering is negligible because of the high masses and lower kinetic energies.

A simplified classical model is here explained.

The maximum acceleration of a single scattering process between an electron of mass $m_e$ and a ion of charge $Ze$ with an impact parameter $b$ is described by:

$$a = \frac{Ze^2}{m_e b^2} \tag{1.36}$$

This interaction can be considered constant for the crossing time $\tau$ of a distance $2b$ at the speed $v$:

$$\tau = \frac{2b}{v} \tag{1.37}$$

The energy irradiated by a single scattering can be approximated in the non relativistic case by:

$$\delta E \simeq \frac{2e^2 a^2 \tau}{3c^3} = \frac{4Z^2 e^6}{3c^3 m_e^2 b^3 v} \tag{1.38}$$

The integral of this expression over all the possible scattering gives the emission power per single electron:

$$w = \int_{b_{min}}^{b_{max}} \delta E 2\pi n_i v b db \simeq \frac{8\pi Z^2 e^6 n_i}{3c^3 m_e^2} \int_{b_min}^{b_max} \frac{db}{b^2} \tag{1.39}$$

$b_{min}$ and $b_{max}$ are, respectively, the De Broglie length $\frac{h}{2\pi m_e v}$ and the Debye length $\Lambda_D = \sqrt{\frac{\epsilon_0 k_B T_e}{ne^2}}$, corresponding to the Coulomb interaction range in plasma.

The result is:

$$w = \frac{16\pi^2}{3} \frac{Z^2 e^6 n_i}{c^3 m_e h} v \tag{1.40}$$

The total power is obtained by integrating on the electron distribution function:

$$W = \frac{8\pi}{3} \frac{Z^2 e^6 n_i}{c^3 m_e h} \int_0^\infty v f_e(v) dv \tag{1.41}$$

Assuming a maxwellian distribution function, the specific power density is described by:

$$W(\nu) = \frac{32\pi}{3} \frac{Z^2 e^6 n_i n_e}{c^3 m_e^2} \left( \frac{m_e}{2\pi k_B T_e} \right)^{\frac{1}{2}} e^{-\frac{h\nu}{k_B T_e}} \tag{1.42}$$

### 1.4.2 Fluorescence line emission

Atoms in a plasma are continuously ionized by the interaction with free electrons. When an electron of an inner atomic shell is stripped, a sequence of radiative emissions takes place to balance the electron hole. This sequence is characteristic of each element and its recognition by X-Ray Fluorescence (XRF) Spectroscopy makes possible the identification of the excited atomic species. XRF spectroscopy is primarily focused on electron shells K,L,M,N, as shown in figure 1.11.

When an electron vacancy in the K shell is filled by an electron from the L shell, the characteristic energy of the emitted photon is called the K-alpha ($K\alpha$) spectral line, and when the K shell vacancy is filled by an electron from the M shell, the characteristic energy of the emitted photon is called the K-beta ($K\beta$) line.

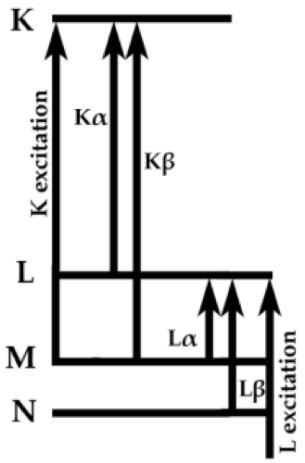


Figure 1.11: Atomic shells configuration and main XRF lines

The substitution of an L and/or M shell electron into a K shell vacancy creates a corresponding energy vacancy in the L and/or M shell, catalyzing an electrical cascade as electrons in the M and N shells emit energy/photons in order to fill the energy vacancies in these lower energy shells. The L-alpha ($L\alpha$) line is the characteristic energy of a photon emitted when an M shell electron fills a vacancy in the L shell and the L-beta ($L\beta$) line is the characteristic energy emitted when an N shell electron fills an L shell vacancy.

Alpha lines generally have a higher count rate than beta lines because electrons from the next higher energy level substitute into low energy vacancies with greater probability than those from energy shells farther away.

The ionization of atoms, which determines the XRF emission, is determined by the specific cross section, depending on both the electrons energy distribution and the atomic ionization cross-section.

The EEDF (Electron Energy Distribution Function) averaged cross section for a specific element is described by the equation 1.43:

$$< \sigma v >= \int_I^\infty \sigma(E) v(E) f(E) dE \tag{1.43}$$

where $\sigma(E)$ is the K-shell ionization cross-section as a function of collision energy, $v(E)$ is the collision speed, $f(E)$ is the EEDF and $I$ is the K-shell

binding energy of the specific element. This calculation is resumed for Ar, Cr and Fe at some typical values of plasma temperatures, by the two plots in figure 1.12.

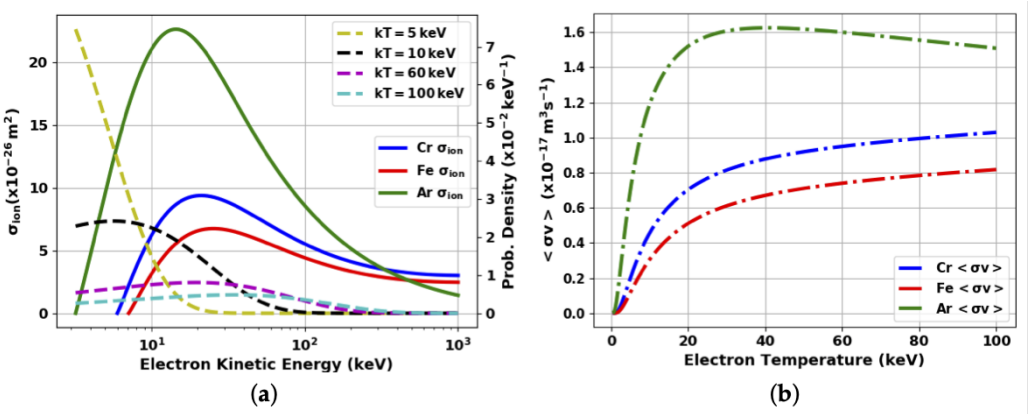


Figure 1.12: (a) Cross sections vs. Maxwell EEDFs of different kBTe; (b) EEDF averaged cross Section [5].

Plot (a) shows the $f(E)$ and $\sigma(E)$ distributions at different temperatures and for different elements separately, plot (b) is the related result of calculation 1.43.

### 1.4.3 Emissivity models: plasma parameters

As previously mentioned, through the analysis of plasma emission and by employing specialized diagnostic techniques (that will be discussed in details in section 2.2), it is possible to obtain valuable information about the plasma parameters.

In the case of X-ray emission, emissivity models are used to be compared with the acquired experimental data [5].

Specifically, it is possible to extrapolate the plasma thermodynamic parameters (namely, density and temperature) from the experimental emissivity energy distribution $J_{exp}$, defined by the equation:

$$J_{exp}(h\nu) = h\nu \frac{N^p(h\nu)}{t} \frac{4\pi}{\Delta E V_P \Omega_g} \tag{1.44}$$

where $h\nu$ is the photon energy, $N^p(h\nu)/t$ is the measured counting rate, $\Delta E$ is the energy bin width, $V_P$ the plasma volume, and $\Omega_g/4\pi$ the geometrical efficiency (defined in each point of the plasma volume as the ratio between the solid angle subtended by the detector and the total emitting angle $4\pi$).

Being $J_{exp}(h\nu)$ the total X-ray emission from both the bremsstrahlung processes and the fluorescence line emission (XRF), it can be decomposed by the sum of the two respective spectra:

$$J(h\nu) = J_{brem.}(h\nu) + J_{XRF}(h\nu) \tag{1.45}$$

The expression for the bremsstrahlung emissivity density is then given as:

$$J_{brem.}(h\nu) = \rho_e \rho_i h\nu \int_{h\nu}^{\infty} \frac{d\sigma_K(h\nu)}{dh\nu} v_e(E) f(E) dE \tag{1.46}$$

where $\rho_e\rho_i$ is the product of the electron and ion density, $v_e(E)$ is the electron speed, $\frac{d\sigma_K(h\nu)}{dh\nu}$ is the differential cross-section, $f(E)$ is the EEDF.

Using Kramer's formula [6] for the differential cross-section and the assumption of a Maxwell-Boltzmann distribution for $f(E)$, the bremsstrahlung emissivity density is described by the equation:

$$J_{brem.}^{M-B}(h\nu) = \rho_e \rho_i (Z\hbar)^2 \left(\frac{4\alpha}{\sqrt{6m_e}}\right)^3 \sqrt{\frac{\pi}{k_B T_e}} e^{-\frac{h\nu}{k_B T_e}} \tag{1.47}$$

By comparing the theoretical emissivity described by equation (1.47) with the experimentally measured one, it is possible to obtain the plasma parameters such as electron density and temperature through a fitting procedure.

This approach has been already widely employed in multiple ECR systems, typically for the volumetric measurement and characterization of parameters [7].

In the present work, a novel approach was used to enable application of this approach preserving local information. A diagnostic method capable of measuring the local X-ray emission and determining plasma parameters in various regions of interest was used.

Chapter 2

# Experimental physics in ECR plasma

The ECR magnetic traps are commonly used as ion sources for accelerators, optimized to produce, extract and accelerate ions from a plasma and generate beams at high charge state and intensity.

The plasma excited in these facilities can become itself an interesting environment for fundamental research in the plasma physics field, whose thermodynamical conditions can be scaled to relevant astrophysical contexts.

In this regard, the **PANDORA** (**P**lasmas for **A**strophysics, **N**uclear **D**ecays **O**bservation and **R**adiation for **A**rchaeometry) project provides to use ECR plasmas for fundamental research aim, studying for the first time in-plasma physical processes, involved in nuclear astrophysical context.

Moreover, the fundamental investigation on ECR plasmas can provide interesting enhancements on the ion sources performances in terms of intensity, stability and high charge state production of the extracted beams for accelerators [8].

A multi-diagnostic system has been specifically developed in this context, with the aim of operating in fully-controlled plasma environment conditions.

The theme of plasma diagnostics, indeed, is a complex and multidisciplinary field that spans various branches of physics, with the aim of understanding the mechanisms underlying plasma dynamics through

the observation of the electromagnetic and thermodynamic phenomena occurring in such environments.

A crucial point in the diagnostics on energetic plasmas is related to the opportunity to make non-intrusive, quantitative analysis of the thermodynamic plasma parameters, namely, electron density and temperature.

In this regard, the use of X-ray diagnostics as a non invasive tool to study hot plasmas is well known in literature, both for ion sources and plasma-based fusion facilities [9].

The present thesis work applies a newly developed X-ray diagnostic technique, capable of space-time-energy resolved measurements, to the investigation of phenomena of relevant interest in the field of ECR plasma dynamics. Several physical cases have been considered during different experimental campaigns on the Atomki plasma facility, specifically developed for ECR plasmas fundamental research [10].

## 2.1 Overview on ECR Ion Sources

The Electron Cylotron Resonance Ion Sources (ECRIS) are plasma devices producing highly charged ions through electron impact ionization [3].

They consist of a cylindrical vacuum chamber, typically made of stainless steel, where a gas mix can be injected at low pressure ($10^{-6} - 10^{-2} mbar$).

The chamber is surrounded by a magnetic system which can be a static magnet or a system of coils (also fully superconductive), providing a magnetic field gradient towards the plasma chamber walls. The principal role of magnetic field (of the order of some T) is the confinement of plasma, which is governed by magneto-hydro-dynamics, determining also the magnetic resonance conditions which allow the heating mechanism.

The heating process is obtained by the injection of microwaves into the chamber by a proper injection system. A proper tuning of the RF frequency in relation to the magnetic field defines the ECR surface, the magnetic region where the electron cyclotron resonance takes place (as explained in section 1.3.4).

A simplified sketch is shown in figure 2.1.

These kind of magnetic traps usually work with microwave frequen-

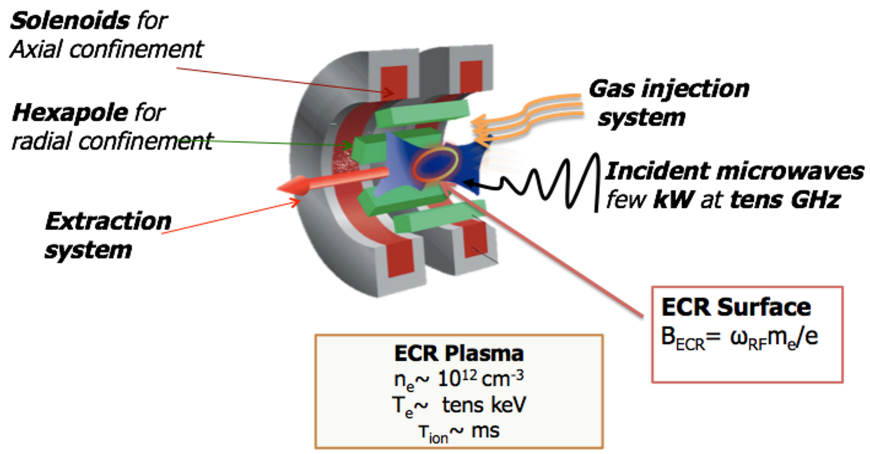


Figure 2.1: Simplified sketch of an ECRIS, highlighting the main components: microwave injection, magnetic confinement system in $B_{\text{minimum}}$ configuration, gas injection, and ion extraction system.

cies in a range between $2.4 - 28\ GHz$ with a power from few tens of W to some kW.

The plasma obtained can reach densities of $n_e \sim 10^{11} - 10^{13} cm^{-3}$ with electron temperatures of $T_e \sim 0.1 - 100\ keV$ ($10^6 - 10^9 K$). Ion temperature usually remain colder ($\sim eV$). The confinement time reaches $\sim 10^{-3} - 10^{-2} s$, allowing to generate high charge states.

Modern ECRIS are capable of producing intense beams of highly charged ions, representing one of the most advanced tools for the generation of multi-charged species. Depending on the frequency of operation, magnetic field configuration, and RF power injection, present-day sources can routinely deliver beam currents of the order of hundreds of microamperes up to several milliamperes for medium charge states (e.g. $O^{6+}$, $Ar^{8+}$, $Xe^{20+}$).

For very high charge states, typical extracted currents are lower but still significant: tens to a few hundreds of microamperes are achievable for ions such as $Xe^{30+}$ in the most advanced superconducting sources. These performances make ECRIS an essential technology for applications ranging from nuclear physics and accelerator facilities to interdisciplinary

fields such as materials science and astrophysics.

## 2.2 Diagnostics of ECR plasmas

Plasma diagnostics is a complex and multidisciplinary field that spans various branches of physics, with the aim of understanding the mechanisms underlying plasma dynamics through the observation of the electromagnetic and thermodynamic phenomena occurring in such environments.

Diagnostic systems can be broadly classified into invasive and non-invasive categories. A representative example of invasive diagnostics is provided by Langmuir probes, which allow localized probing of the electric potentials within the plasma. These systems enable a direct investigation of the electron density and temperature, although they inevitably perturb the plasma environment.

The ion extraction systems, coupled to a mass spectrometer, can provide information about the ion content of plasma, investigating the current extraction dynamics and the charge state distribution (CSD). These systems are likewise classified as invasive diagnostics.

Non-invasive diagnostic systems, on the other hand, involve the observation of plasma transport and self-emission phenomena across the entire electromagnetic spectrum.

Representative examples are detection systems operating in the visible and X-ray ranges, which probe the characteristics of plasma emission within their respective energy domains, and interferometric or polarimetric diagnostics in the microwave regime [11].

These diagnostics are especially valuable, as they permit access to morphological and thermodynamic properties of the plasma without perturbing it.

The plasma EM emission, indeed, covers a wide range of the electromagnetic spectrum. It can be studied through the detection of transmitted and self-emitted microwaves, visible light and X-ray radiation.

An example of multi-diagnostic system applied to ECR plasmas will be shown in the next section [2.3], introducing the PANDORA ECR facility.

Microwave interfero-polarimeters are able to measure the Faraday rotation angle of a probing wave crossing the plasma, allowing to estimate the line-integrated plasma electron density.

Optical spectrometers can analyze the low-energy emission ($\sim 1 - 100\ eV$) especially by recombination and fluorescence processes, also being able to probe the opacity mechanisms of the light transmission in plasma, while X-ray detectors can study higher energy phenomena in the range of $0.1 - 100\ keV$ (soft and hard X).

The X-ray plasma emission is particularly relevant since it allows to probe the high-energy components of plasma emission, mainly related to the dynamics of highly heated electrons.

Space-resolved measurements by pinhole based imaging techniques enable the morphologic study of different kinds of plasmas [12, 13, 14, 15].

These techniques have allowed along the years to investigate the dynamics of various kinds of magnetically confined plasmas, evidencing their overall structure and the spatial distribution of the warmer electrons, which play a main role in leading to X-ray emission via characteristic lines and bremsstrahlung radiation.

Energy-resolved measurements, tipically performed on ECRIS plasmas by silicon and HPGe detectors, allow to characterize the fluorescence and bremsstrahlung emission [16, 17, 18], thus determining the spectral temperature of the electrons, by analyzing the Electron Energy Distribution Function (EEDF) with appropriate plasma emissivity models ([7], section 1.4.3).

Coupling the energy-resolved X-ray measurement with the X-ray CCD imaging turns out to be a powerful technique: the quantitative evaluation of the experimental X-ray spectra can be provided in a space-resolved way, by means of a specifically developed analysis technique providing the Single Photon Counting (SPhC) acquisition from CCD devices [19].

Moreover, as will be better described in the next sections, the observation of plasma in the $\gamma$ energy range allows to probe the in-plasma radionuclides decay physics, which opens a wide and multidisciplinary field of the experimental physics.

The experimental techniques here described are finalized to study magnetized plasma properties by multi-diagnostic systems, installed on

ECR plasma traps specifically designed for research aims.

An example of such multi-diagnostic approach will be shown in the next section (2.3).

## 2.3 The PANDORA project: ECR plasmas for interdisciplinary measurements

Magnetized ECR plasmas in compact traps may become experimental environments for the investigation of phenomena of astrophysical and nuclear astrophysical interest.

The flexibility of a laboratory plasma environment makes possible to reproduce specific experimental conditions where to study the properties of such state of matter. The MHD dynamics and the transport of light in an electromagnetically active medium are examples of the kind of physics which can be investigated.

The **PANDORA** (**P**lasmas for **A**strophysics, **N**uclear **D**ecays **O**bservation and **R**adiation for **A**rchaeometry) project [20, 21] proposes a novel facility to emulate plasma conditions scalable to stellar-like environments.

The innovative facility consists of a B-minimum magnetic trap working on the principles of an ECR ion source, equipped with a multi-diagnostic system which allows to perform a complete monitoring of all the plasma observables relevant in the thermodynamics and magneto-hydrodynamics.

The plasmas of PANDORA facility will reach electron density and temperature of $n_e \sim 10^{11} - 10^{13} cm^{-3}, T_e \sim 0.1 - 100 keV$, respectively. The plasma is confined by a superconducting magnetic system reaching magnetic fields in the order of few Tesla and resonantly heated by some kWs of microwave power in the 18 - 21 GHz frequency range.

The trap will be surrounded by an array of 14 HPGe detectors, which represents the main focus of the facility, being able to perform the $\gamma$-tagging of nuclear decays in plasma.

Figure (2.2) shows a sketch of the facility, highlighting the main components of plasma ignition and confinement (the RF injection and mag-

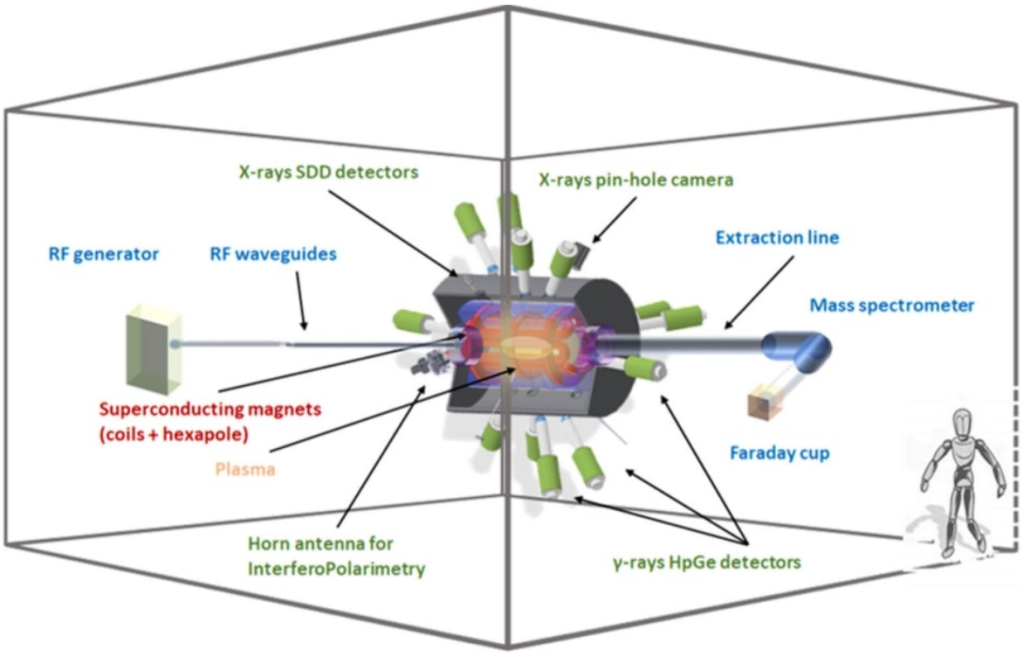


Figure 2.2: Sketch of the PANDORA facility with the main components about plasma ignition and confinement and part of the multi-diagnostic system - Adapted from [21].

netic systems) and the array of HPGe.

The main goal of the project is the investigation of $\beta$ decays in high-energy-density plasmas, which is an open issue in Nuclear Astrophysics: significative variations of the decay rate are expected in highly ionized environments, while terrestrial measurements involve, up to now, neutral species.

The decays involved in nuclear astrophysics should be investigated in peculiar plasma environments, where the charge states of ions can induce significant variations.

There is great interest in Nuclear Astrophysics for any attempt at improving knowledge of weak interactions in physical conditions similar to those of nucleosynthesis environments (stars, the Big Bang and cosmic rays), in fact the weak interaction represents the most important bottleneck in nucleosynthesis calculations. In the s-process (i.e., the slow neu-

tron capture process), as an example, the relative abundances of elements and isotopes produced depend on the interplay between neutron densities (neutron fluxes coming from reactions producing neutrons), neutron capture cross sections, and decay rates. The interplay between neutron capture phenomena and the charge-state-induced $\beta$ decays introduces enormous uncertainties in the knowledge of the lifetimes of isotopes close to the valley of $\beta$-stability.

Beyond the nuclear decays investigation, the PANDORA facility will make possible the measurement of plasma opacity in different thermodynamic conditions, being the mechanisms of light transport in plasma particularly relevant in the dynamics of many astrophysical phenomena.

This kind of measurements has a great impact on the comprehension of the radiative transport, thus on the evolution of electromagnetic transients like the kilonova (KN) phenomena, of great interest in the last years [22, 23].

**In-plasma $\beta$ decay investigation** Experiments performed at storage rings confirm that the lifetimes of these decays can change significantly as a function of the ionization state [24].

Variations even of several orders of magnitude are expected in the $\beta$ decay rate [25, 26]. The PANDORA project aims at measuring, for the first time, the correlation between the thermodynamic parameters of plasma and the nuclear lifetime, which depends on the plasma ions charge state distribution.

The main decay mechanisms investigated in this approach are the bound-state $\beta$ decay, where the electron emitted in the decay process remains bound in the atomic orbitals, and the electron capture (EC) decay, where an electron of the atomic shells is being captured from the nucleus.

The atomic shells population at different charge states can affect the phase-space volume involved in both the decays, determining relevant variations on the expected lifetime [27].

In the PANDORA plasma trap, the radionuclides will be trapped in a dynamic-equilibrium for several hours or days, depending on the experimental requirements for the measure significance [28], keeping the local

density and temperature constant.

The Charge State Distribution (CSD) can be modulated according to the pumping RF power, the magnetic field and the background pressure. The decay rates can be then characterized with respect to the CSD variation, and versus the plasma density and temperature, in a stellar-like condition (as concerns, mainly, the CSD conditions and electron temperature).

For the first phase of PANDORA, a subset of physical cases was chosen to start the study, relying to scientific relevance to nuclear astrophysics processes (Big Bang Nucleosynthesis, s-process nucleosynthesis, role of CosmoChronometers, etc.), on the expected effects on the lifetime, due to radionuclide in-plasma CSD and on the maximum ionization state that can be reached by the trap design. Moreover, being the identification of the decay products based on the $\gamma$-ray detection, only isotopes whose daughter nuclei emit $\gamma$-rays were chosen [29].

The selection procedure has given four isotopes as outputs: the $^{176}Lu$ (which might play a crucial role as cosmo-clock), the $^{134}Cs$ (involved in s-processes and relevant to produce the s-only isotopes $^{134}Ba$ and $^{136}Ba$), the $^{94}Nb$ (relevant for the abundance of $^{94}Mo$ in single or binary systems of stars), the $^{7}Be$ (still open question of the so-called Cosmological Lithium Problem).

| **Isotope** | $t_{1/2}$ | **Type of decay** | **Daughter nuclei** | $E_\gamma[keV]$ |
|---|---|---|---|---|
| $^{176}Lu$ | $3.78 \cdot 10^{10}[yr]$ | $\beta^-$ | $^{176}Hf$ | 202.88 & 306.78 |
| $^{134}Cs$ | $2.06[yr]$ | $\beta^-$ | $^{134}Ba$ | 795.86 |
| $^{94}Nb$ | $2.03 \cdot 10^{4}[yr]$ | $\beta^-$ | $^{94}Mo$ | 871.09 |
| $^{7}Be$ | $53.2[days]$ | EC | $^{7}Li$ | 477.60 |

Table 2.1: Physical cases of PANDORA reporting the isotope of nuclear astrophysics interest, the half-life in the neutral state, the type of decay, and the daughter nuclei including the energy of the emitted $\gamma$-rays after the decay.

The experimental method consists of magnetically confining a hot plasma, kept in dynamic equilibrium, containing a known concentration of the $\beta$-decaying atoms, and then measuring the decay rate as a function

of the average ionization state of radioactive ions confined in the trap [30].

The decaying nuclei will be identified by measuring the energy of the $\gamma$-rays emitted by the daughter nuclei.

Since the selected physics cases involve the emission of secondary $\gamma$-rays, the total amount of decays becomes detectable via $\gamma$-rays tagging by means of an array of 14 HyperPure Germanium (HPGe) detectors placed around the plasma trap, 12 radially and 2 axially. Figure 2.3 shows a schematic of the PANDORA setup and the positions of the HPGe detectors. Due to geometrical constraints set by the superconducting magnetic system, each $\gamma$-detector has a narrow field of view and the final detection efficiency ranges between $0.1 - 2\%$, depending on the energy of the photon. This implies that measurements must be made over an extended period of time in order to deduce decay rates with high level of certainty.

The line-of-sight of each HPGe intersects gradients in plasma density and temperature, which requires the use of geometrical models [29] to map the decay rate with plasma thermodynamic parameters.

Figure 2.3 shows a sketch of the PANDORA facility, focused on the magnetic confinement system, the cryostat, and the HPGe detector array.

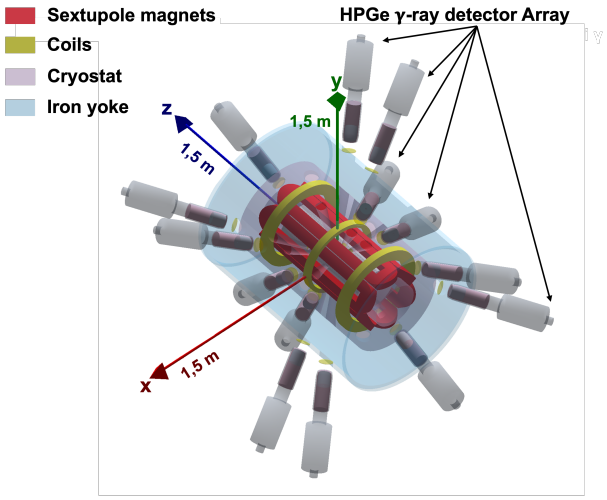


Figure 2.3: Simplified sketch of the PANDORA facility, focusing on the magnetic confinement system, the cryostat, and the HPGe detector array - adapted from [29].

**Opacity measurements of astrophysical interest** Plasma opacity has a great impact both on radiative transport and spectroscopic observation of many astrophysical phenomena. In particular, the physics case of the kilonova (KN) became of great relevance for nuclear astrophysics in the last years, since its first observation in 2017 [31].

The electromagnetic transient known as kilonovae, are among the photonic messengers released in the post-merger phase of compact binary objects, e.g., binary neutron stars, and they have been recently observed as the electromagnetic counterpart of related gravitational-wave (GW) events. The detection of KN signal plays a fundamental role in the multi-messenger astronomy entering in a sophisticated GW-detecting network. KN light-curve also delivers precious information on the composition and dynamics of the neutron-rich post-merger plasma ejecta (relying on r-process nucleosynthesis yields). In this sense, studying KN becomes of great relevance for nuclear astrophysics.

Theoretical models attempting in encoding the opacity of this system often fail, due to the complexity of blending plethora of both light- and heavy-r nuclei transition lines, requesting for more complete atomic database. Trapped magneto-plasmas conceived in PANDORA could answer to these requests, allowing experimental in-laboratory measurements of optical properties and opacities, at plasma electron densities and temperatures resembling early-stage plasma ejecta's conditions, contributing to shed light on r-process metallic species abundance at the blue-KN diffusion time.

A crucial point in making the ECR plasma an experimental environment is the determination of stable MHD and thermodynamical conditions. Such stability is required for long period of time in both the abovementioned cases, especially in the $\beta$ decay measurement, which are estimated to last weeks or months, depending on the expected activity of the radionuclides of interest.

For this aim, a remarkable effort is being spent to develop a diagnostic system able to monitor the plasma stability in terms of magnetic confinement and thermodynamic parameters.

**The multi-detectors system of the PANDORA facility** At INFN-LNS and in collaboration with the ATOMKI laboratories, several non-invasive

diagnostic techinques and tools were developed in the last years [32] with the final goal of developing the complete multi-diagnostic system required for the PANDORA research facility.

The basic idea is that the in-plasma experimental environment of the PANDORA measurements is fully under control, in terms of MHD stability, electron density $n_e$ and temperature $T_e$, and ion charge state distribution (CDS).

The advanced multi-diagnostic system includes dozens of non-invasive devices that will operate simultaneously for the non-intrusive on-line monitoring of all the relevant plasma properties.

In more detail, the multi-diagnostic setup will consist of the following:

1. Two spectrometers with different spectral resolutions for the plasma-emitted visible light characterization: the first is the SARG (Spettrografo Alta Risoluzione Galileo) spectrograph with a high spectral resolution of $R = (\lambda/\Delta\lambda) = 160000$ in the spectral range of $370 - 900nm$ [33].

   Such a value allows one to identify spectral lines separated up to 0.003 nm at $\lambda = 500nm$. By this resolution, SARG is in principle able to identify spectral line shifts (due, for example, to isotopic line shift or Doppler effects) in the order of $0.004nm$. This resolution makes possible to resolve the Doppler, collisional or Stark effects line broadening at ion temperatures of few eV and the Zeeman splitting in the order of Bmin = 0.2 T [34].

   The second consists of a Horiba iHR550 spectrometer, coupled to a Synapse Horiba CCD camera, with a nominal resolution around $0.035nm$ ($R = 13900$ $at$ $\lambda = 486nm$) in the spectral range of $300 - 750nm$ [35].

2. One Incoherent Thomson Scattering (ITS) system used for the direct and non-invasive measurement of electron properties [36].

   It is made of (i) a 532 nm Quantel with a 10 Hz Nd:YAG laser of 430 mJ nominal pulse energy, (ii) an Acton Standard Series SP- 2756 imaging spectrometer, equipped with three gratings in order to access different spectral ranges (and hence different ranges of electron

energies), (iii) a PI-MAX 4: 1024f iCCD camera for photon detection, and (iv) a fiber bundle for light collection from the plasma volume and transmission to the camera detector (Princeton Instruments, Acton, MA, USA).

3. Two Silicon Drift Detectors (SDDs) used to characterize the warm (0.5–30 keV) electrons in the plasma, measuring electron density and temperature [37].

   The SDDs have an energy resolution of 160 eV at 5.9 keV, a maximum quantum efficiency in the 2-30 keV energetic range, and can operate at a high counting rate ($\sim 10^5 cps$).

4. Twelve High-purity Germanium (HPGe) detectors [28, 38] with an average resolution (Full Width at Half Maximum, FWHM) lower than 2.5 keV at 1.3 MeV, placed radially around the PANDORA plasma chamber. The HPGe detectors have a length of 240 mm and a radius of 43.4 mm and are composed of a coaxial hyper-pure crystal with an $\sim 82mm$ length and $\sim 38mm$ radius.

   The array of HPGe detectors will be used for the $\gamma$ tagging of daughter nuclei. Moreover, they allow to characterize the hot electrons population (30–400 keV) in the plasma [37, 7].

5. Two X-ray pin-hole CCD systems for 2D/3D space-resolved spectroscopy. The X-ray CCD camera (SOPHIA-XO by Princeton Instruments) is made by a sensor of $27.6 \times 27.6mm$ and $2048 \times 2048$ pixels, with an optimal quantum efficiency in the range of 100 eV - 30 keV and coupled with a lead pin-hole focusing system and an external X-Ray shutter. A detailed description of the X-ray pin-hole camera system will be presented in Section 4

6. A two-pins RF probe connected to a Spectrum Analyzer (SA) in order to characterize the EM emission inside the plasma chamber performing frequency-resolved spectra.The Spectrum Analyzer operates in the range of 13–15 GHz with a resolution bandwidth of 3 MHz and a sweep time of 400 ms.

   This setup is able to detect both the main pumping RF frequency and the plasma self-emitted sub-harmonics, which can provide sig-

natures of plasma kinetic instabilities (characterized by fast RF and X-ray bursts [39, 40].

7. A W-band superheterodyne polarimeter for the measurement of the total line-integrated electron density based on the measurement of the Faraday rotation [41].

   The system consists of a signal generator for the probing wave and two high-directivity horn antennas, of which the rotatable receiving antenna is connected with an orthomode transducer (OMT) (a waveguide component to combine or separate two orthogonally polarized microwave signal paths).

Figure 2.4 shows the full multi-diagnostic system, sketched in the final configuration on the PANDORA plasma facility. Table [2.2] summarizes all the above-mentioned diagnostics, highlighting the main features explained in this section.

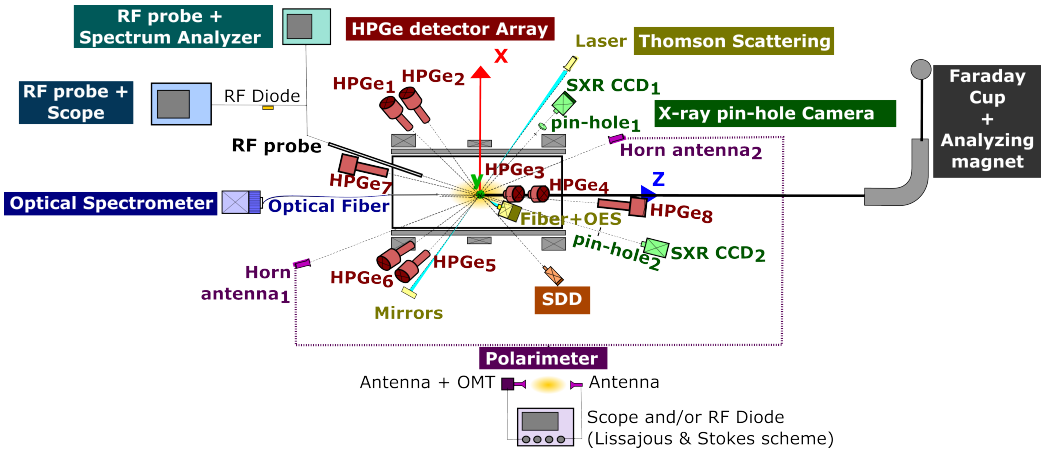


Figure 2.4: Sketch of the multi-detectors system of PANDORA. [42]

| Diagnostic Tool | Sensitive Range | Measurement | Resolution-Measure Error |
|---|---|---|---|
| 1 Visible light camera | 1 ÷ 12 eV | Optical Emission Spectroscopy: cold electrons' temperature and density | $\Delta\breve{} = 0.035$nm R=13900 |
| 1 Thomson Scattering | 0.5 ÷ 500 eV | EEDF, absolute electron density | Condition-dependent (a function of spectral width, dependent on temperature, and area, dependent on density |
| 2 SDD | 1 ÷ 30 keV | Volumetric soft X-ray Spectroscopy warm electrons' temperature and density | Resolution $\sim$ 120 eV $\text{ffl}_{\text{ne}} \sim 7\%, \text{ffl}_{\text{Te}} \sim 5\%$ |
| 14 HPGe detector | 30÷2000 keV | Volumetric hard X-ray Spectroscopy: hot electrons' temperature and density | *FWHM<2.4 keV $\text{ffl}_{\text{ne}} \sim 7\%, \text{ffl}_{\text{Te}} \sim 5\%$ |
| 2 X-ray pin-hole camera | 2 ÷ 15 keV | 2D Space-resolved spectroscopy: oft X-ray Imaging oft X-ray Imaging | Energy resolution $\sim$ 0.3 k Spatial resolution $\sim$ 0.5 mm |
| 2 Multi-pins RF probe | 10÷26.5 GHz | Local EM field intensity | ffl $\sim$ 0.073 ÷ 0.138dB |
| Multi-pins RF probe + Spectrum Analyzer (SA) | 10÷26.5 GHz (probe range) | Frequency-domain RF wave | SA Resolution bandwidth: RBW = 3 MHz |
| Multi-pins RF probe + Scope + HPGe detector | 10÷26.5 GHz (probe range) | Time-resolved RF burst and X-ray time-resolved Spectroscopy | 80 Gs/s (scope) Time scales below ns |
| Multi-pins RF probe + X-ray pin-hole camera | 10÷26.5 GHz (probe range) | Time-resolved RF burst and X-ray spatial and time-resolved Spectroscopy | 80 Gs/s (scope) Time scales below ns |
| Microwave Imaging Profilometry (MIP) | 60÷100 GHz | Electron density profile | $\text{ffl}_{\text{ne}} \sim 1\% \div 13\%$ |
| 1 W-band super-heterodyne polarimeter | W-band 90÷100 GHz | Plasma-induced Faraday rotation: line-integrated electron density | $\text{ffl}_{\text{ne}} \sim 25\%$ |

*@ 1332.5 keV

Table 2.2: Overview of the multi-detectors system of the PANDORA facility [42].

The present work is particularly focused on the innovative CCD pin-hole camera diagnostic system, which allows to investigate the plasma structure and confinement dynamics. The diagnostic is able to perform space resolved spectroscopy and imaging, thanks to an advanced analysis algorithm developed at INFN-LNS, in collaboration with Atomki - Debrecen laboratory [10].

## 2.4 Thermodynamic parameters of ECR plasmas

As previously mentioned, the application of non-invasive, energy-resolved X-ray diagnostics to the ECR plasma enables the measurement of thermodynamic parameters.

Most of the available X-ray spectroscopy studies on ECR plasmas rely on volumetric measurements, i.e., the total flux emitted from the plasma along a given cone-of-view, normally individuated by proper collima-

tion systems, which are widely performed to characterize the EEDF from mostly the bremsstrahlung emission [7, 8, 43].

However, being these plasmas in non-LTE (local thermodynamic equilibrium) conditions (see section 1.4), the method is strongly affected by EED anisotropy and deviation from a single Maxwellian slope: actual ECRIS EEDF are in fact characterized by the presence of different electron populations (cold, warm, and hot), each one contributing to the overall distribution function, which assumes the typical three-slope structure (figure 1.10), and whose experimental decoupling represents a criticality of any diagnostic setup.

An additional limitation in the use of simplified volumetric setups for the X-ray diagnostics comes from the difficult decoupling of the pure plasma-emitted radiation from the X-rays coming from the plasma chamber metal walls.

Fluxes of deconfined electrons also contribute to bremsstrahlung radiation, and even this emission is comparatively larger than the one coming from the plasma core directly, due to the higher density of solids composing the chamber walls. The mixing of both plasma and plasma chamber wall contributions seriously affects the reliability of volumetric measurements when collimators are not properly designed and shaped in order to totally suppress the unwanted contributions.

To deal with this important issue, several measurements have been performed by using on-purpose developed collimators, to have cones-of-view intercepting specific portions of the plasma (typically, the plasma core) [7, 44].

A significant step forward, improving by far the reliability of a real plasma x-ray flux measurement, without significant contribution from the plasma chamber walls, can be done by using position-sensitive detectors, such as charge coupled devices (CCD), coupled to pinholes [45]. This “camera-obscura”-like setup enables both energy and space-resolved measurements: in this way, having the opportunity to collect spatial images of the plasma under different excitation conditions, it is directly possible to individuate the signal coming from the confined plasma vs deconfined plasma fluxes.

In particular, the X-ray imaging focused on the characteristic line emission of plasma atomic species gives access to information about in-plasma

ion distribution; moreover the deconfined electron fluxes are made evident by the characteristic line emission of the metals in the chamber walls, induced by the electrons' impact. [46, 47].

As reported in *Mascali et al.* [48], X-ray-integrated imaging measurements have been performed using a CCD detector, obtaining a map of confined and deconfined plasma under different plasma tuning conditions [e.g., single vs double frequency heating, radio frequency (RF) power and frequency scaling, and background pressure].

Due to the lack of precise measurements on warm electron-driven plasma radiation (1 - 30 keV), only a few data about absolute values of plasma density and temperature in an ECR setup are nowadays available [49]. The typical CCD detector sensitivity range (2 - 20keV) suites very well for probing the warm electron plasma parameters, whose related spatial distribution affects the ion charge state distribution (CSD). The overall performances of an ECRIS can be strongly influenced by the latter quantity.

The coupling of the energy-resolved X-ray measurement with the X-ray CCD imaging was applied in *Naselli et al.* [46], by developing a specific post-processing algorithm described in detail in the publication. The energy and position of each single photon is collected in a full-field view of the plasma, thus producing a 2D x-ray plasma image, preserving the energy information and the absolute brightness in each pixel (i.e., number of photons per second, per $cm^2$). Consequently, this enables the local estimation of the plasma parameters (electron density and temperature) and spectral composition investigations in different regions inside the plasma chamber.

This thesis work will show the application of the space-energy resolved technique on the evaluation of local warm electron temperature and density, performed on an ECR argon plasma, heated by 200W microwave power in the 14 GHz ECR ion source (Atomki–Debrecen, Hungary).

## 2.5 Open issues on ECR plasma dynamics

The understanding of several aspects of plasma dynamics underlying the operation of ECR sources remains a current and debated topic in the scientific community. Many features of the plasma in these sources are still not fully understood, also because the observation of several phenomena is usually challenging in such facilities, due to the limited accessibility for diagnostics.

This section explores some of these aspects, in particular the phenomenon of gas mixing—whose effects on the performance of ECRISs are well established—and the pulsed-plasma transient dynamics, the latter being especially relevant for understanding the contribution of the electromagnetic waves in the plasma confinement dynamics.

A concise review of the recent literature is also presented, identifying some of the most relevant findings that provide motivation for a more in-depth experimental investigation.

### 2.5.1 Gas mixing dynamics

Mixing two gases in an electron cyclotron resonance ion source (ECRIS) is a common technique to increase the extracted current of the highest charge states of a heavier element. This effect was experimentally discovered by *A. G. Drentje* [50] in 1983, and it is widely exploited to enhance the performance of ECR ion sources.

The overall reasons of this phenomenon are still under discussion, although there are a few explanations for what happens when two gases with different masses are mixed in an ECRIS [51]. The most widely accepted explanation consists of a mass effect in the ion cooling of the heavier element due to the ion-ion collisions between lighter and heavier species. The low-mass ions that drag energy from the heavy ones would efficiently carry out the ion energy because of their lower confinement [52, 53]. There is much experimental evidence that a mass effect exists in the gas mixing technique [54, 55]. Moreover, experimental observations show that the high charge state performance of an ECRIS plasma is worse after ion heating by cyclotron waves [56]. The experimental evidence of the ion cooling phenomenon in a gas mixing measurement was provided

by *Melin et al.* [57].

Another possible explanation deals with the changes in the potential dip value as the dominant phenomenon in the gas mixing effect. Particle In Cell (PIC) simulations [58] show that the ion temperature can be even increased in the gas mixing mode in parallel to an increase of the potential dip value. Even with an increased ion temperature, the ratio between the confining potential and the ion temperature is higher in the gas mixing mode of operation, resulting in improved ion confinement and subsequent population of the higher charge states of the heavier species. Furthermore, the simulations show a plasma density gain in proximity of the potential dip at the ECR surface.

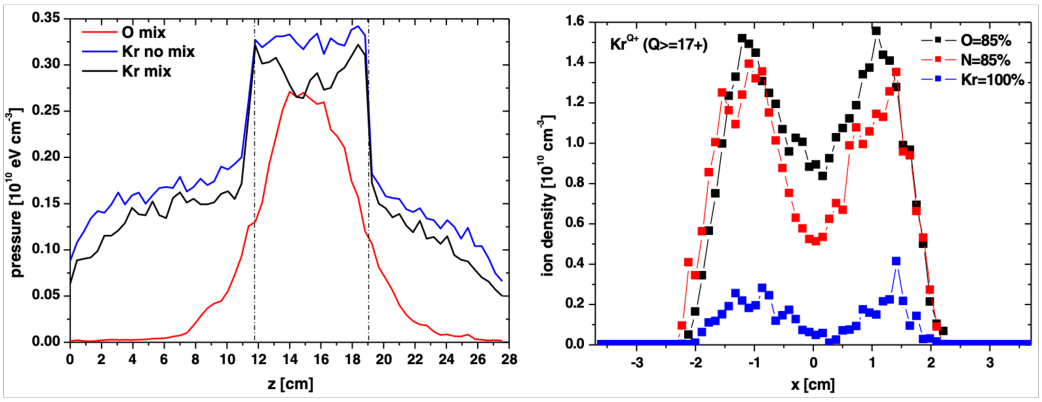


Figure 2.5: Ion pressure profiles along the source z axis: pressure of the oxygen ions (red line), pressure of the krypton ions at Kr ¼ 95%, O ¼ 5% (black line), and pressure of the krypton ions at Kr ¼ 100% (blue line) - Adapted from [58].

Figure 2.5 reports two plots extracted from *Mironov et al.* publication [58], showing the X and Z axis profiles of plasma density, obtained by O+Kr gas mixing simulations. On the left the z-axis profiles are compared between oxygen mixed (red line), krypton mixed (black line) and krypton not mixed (blue line), observing a hollow profile and a flat profile in the mixed and not mixed Kr cases respectively. The authors state that the oxygen ions push the krypton ions toward the ECR zone boundaries, thus degrading their confinement.

Similar profiles are shown in the x-projections of the highest charge

states of Kr ($Q \geq 17+$) (figure 2.5-right), in the not-mixed Kr and $O = 85\%$ and $N = 85\%$ mixed cases.

Being these simulation results particularly relevant in the comprehension of the gas-mixing phenomena, although no direct validation has been found in literature, the experimental investigation about the spatial features of plasma in gas-mixed plasmas could significantly support such results.

### 2.5.2 Plasma transient dynamics

The operation of an ECRIS with a pulsed RF ignition allows to observe phenomena of relevant interest in the plasma dynamics and about the electromagnetic properties of plasma.

The steady-state of the ECR plasma is characterized by a dynamical equilibrium between the neutral gas injection and the electrons and ions loss, the ECR heating and thermalization/cooling. Moreover, the interaction of the injected waves with the plasma determines the RF-scattering phenomenon and the existence of the so-called "potential dip", the electric potential generated by the ponderomotive forces due to the interaction of the EM pumping wave with the plasma electrons [59, 60, 61].

The latter is difficult to be directly measured, although the phenomenon has been widely studied by indirect measurements, waves-plasma interaction theory and PIC (Particle In Cell) and electrostatic simulations.

The ion dynamics is strongly affected by the spatial distribution of the electrostatic potential and collisionality of the highly charged particles. In particular, the presence of the potential dip gives a strong contribution in the electrostatic confinement of the high charge state ions near to the ECR isosurface, generating the so-called "double layer", namely the differential displacement of ion and electron density.

Figure 2.6 highlights the evidence of the double layer condition, simulated in *Mascali et al.* [59].

The RF-induced scattering contributes to $\sim 20\%$ of the electron deconfinement over the plasma chamber walls [58, 62].

When the pumping microwave is switched off, the potential dip decays in the time scale of $\sim \mu s$ [63], determining the deconfinement of highly charged ions. This phenomenon was first observed by Melin et

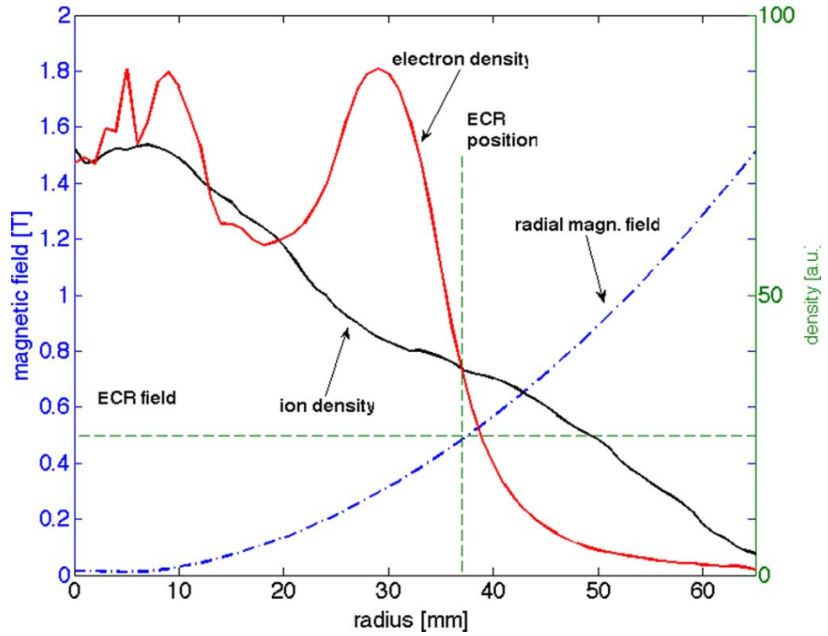


Figure 2.6: Simulated electron and ion radial density profiles compared to the magnetic field shape. The electron density is peaked slightly before the ECR due to weak off-resonance heating which, however, causes the particle being reflected before reaching the resonance - Adapted from *Mascali et al.* [59].

al [64], defining the so called "afterglow peak" on the extracted current, occurring in the time scale of $\sim 1ms$. The peak currents of the afterglow transient can exceed the steady-state ion currents by a factor of 2 - 6.

After this transient, the plasma decays in the time scale of $10 - 100ms$, depending on the magnetic configuration [65]. During this decay the plasma exists without the RF power source, and instability phenomena are observed, determining a peculiar time-evolution of the decay itself.

In particular, the ion beam currents exhibit some instability with time scales matching closely with the instabilities of the bremsstrahlung emission.

Figure 2.7 shows the extracted ion current decay of $Ar^{11+}$ measured in *Tarvainen et al.* [65] in two different operating conditions of power and magnetic field.

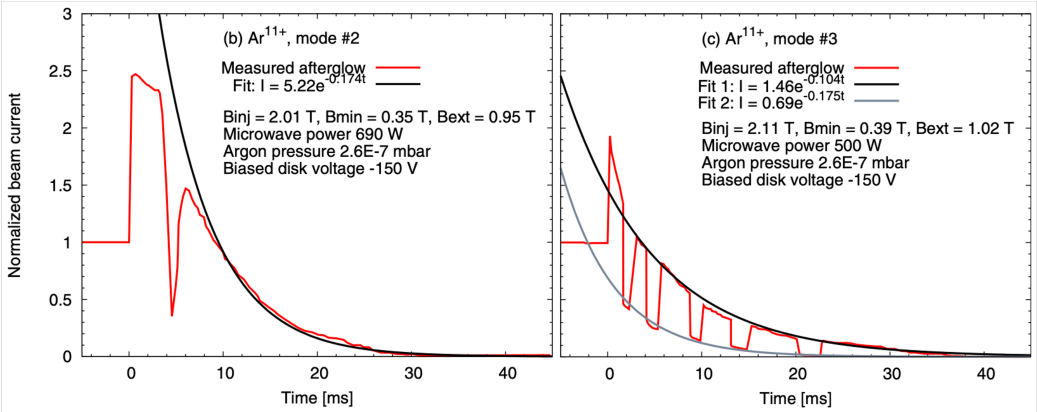


Figure 2.7: Two observed modes of afterglow: double peak structure followed by 'quiescent' decay and unstable but repeatable decay mode with two exponential envelopes - Adapted from [65].

The authors of these plots suggest that the onset of the afterglow instabilities could be driven by the electron instabilities due to relaxation of the electron energy distribution, concluding that the afterglow transient is probably triggered by electrons escaping via the loss cone due to interruption of the ECR-heating process.

The qualitative explanation of the afterglow is the following [63]: when the microwave radiation is switched off, the cold electron flux from the plasma increases abruptly (as observed in the experiments [65]), which causes the potential dip to disappear due to the removal of the ambipolar barrier. This leads to a rapid expulsion of the high charge state ions that were confined electrostatically in the steady-state. In other words, the afterglow peak implies a change of confinement scheme (and time) from electrostatic confinement to diffusive losses.

The physics of the afterglow transient is not completely understood, being dependent from the electrostatic ion confinement/deconfinement dynamics, difficult to be directly studied.

The observation of plasma during its decay transient allows to analyze the dynamics of processes happening in the absence of the pumping RF, investigating both on the afterglow phenomenon and the subsequent plasma instabilities. Moreover, the comparison between a steady-state

and a decaying plasma also allows to evaluate the contribution of the RF scattering in the electron deconfinement phenomena.

## 2.6 Experimental goals

The complete and reliable reconstruction of plasma thermodynamics requires space-resolved techniques, such as the X-ray pinhole camera; however, these techniques must be extended beyond their current limits, since monitoring of the PANDORA plasma in the gas-mixing regime will be required, which will in turn represent the standard operational mode for the experiments.

Fast temporal transients can also be of critical importance, requiring dedicated adaptations of the setup and diagnostic methods.

Beyond their relevance to the success of the PANDORA experiment, they hold intrinsic scientific significance in the context of ECR sources, where both gas mixing and temporal transients (instabilities, afterglow, etc.) remain insufficiently understood and thus not yet fully exploited to enhance device performance (currents, charge states, etc.).

The present thesis work is devoted at investigating on the abovementioned open issues on ECR plasma dynamics, building-up a robust diagnostic technique that will be mandatory for the PANDORA aim of measuring in fully-controlled plasma conditions.

Measurements from several experimental campaigns will be presented, performed on the 14 GHz ECR ion source facility (Atomki–Debrecen, Hungary) [66] during the period 2018 - 2024.

The gas mixing effect, afterglow transient and kinetic instability have been investigated, being these phenomena still not completely understood, by the application of a space-energy-resolved X-ray diagnostic. This technique is an insightful way to study the dynamics of such phenomena, making possible the probing of plasma confinement structures by observing its bremsstrahlung and X-ray fluorescence emission.

No direct experimental evidence exists about the spatial distribution of plasma in the gas mixing condition, therefore the fluorescence analysis on plasma imaging could give relevant answers about the ion confine-

ment when the gas mixing effect is occurring, distinguishing the emission of all the mixed gas species.

Moreover, the time-resolved application on the afterglow transient provides relevant elements about the time evolution of plasma structure's decay and also investigate on the contribution of the injected microwave in the confinement dynamics, being possible to observe for the first time the emission of a decaying plasma in the absence of a pumping microwave.

The space-energy resolved measurement technique has been applied for the first time on the evaluation of local warm electron temperature and density, as reported in the recent publication on Physics of Plasma journal [67].

Chapter 3

# Instruments and methods

The measurements described in this work have been obtained adopting a space-time-resolved spectrometry technique, performed by an X-ray pin-hole camera, consisting of a CCD detector coupled with a "camera obscura", containing all the pin-hole collimation and X-ray shuttering systems.

A characterization was performed on the pin-hole camera by an X-Ray Fluorescence (XRF) test-bench, in order to optimize the SPhC technique, from the acquisition setting to the analysis algorithm, with a particular focus on the energy calibration criteria.

The following sections will introduce the technique of the pin-hole camera applied to the CCD space-resolved spectrometry, then describing the experimental setup, consisting of the pinhole-camera diagnostic system and the XRF test-bench.

Subsequently, the characterization study will be explained in detail, whose results represent a significant advancement over the current state of the art [46].

## 3.1 Pin-hole camera imaging technique

This technique has been the most ancient way to focus light in an obscure camera (first uses have been documented in the XI century, well before the first optical lens).

The advantage, in respect of a lens, is that a pinhole is not affected by chromatic effects, and it can work also in the X-ray domain (X-ray light can't be focused with a common optical lens).

The system consists of a "camera obscura" closed by a lead disk (to block X-rays) with a tiny circular hole, through which it is possible to reproduce the image of the object of interest in a position-sensitive detector, as shown in the simplified scheme in figure 3.1.

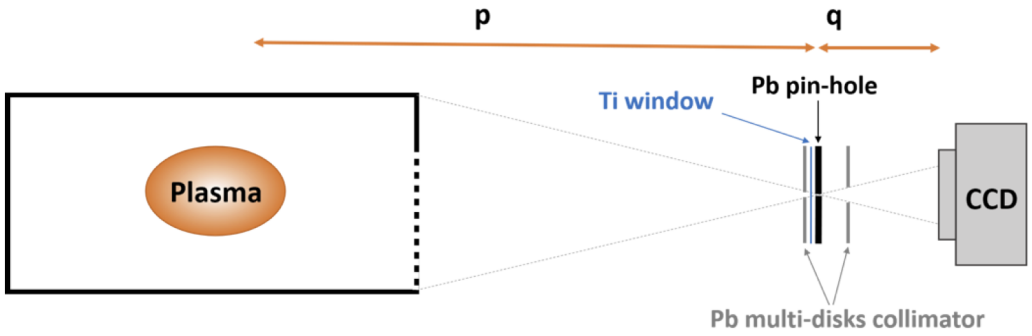


Figure 3.1: Sketch of a CCD pin-hole camera applied to a schematized plasma chamber.

The magnification M depends on the respective distances between the pin-hole, the observed object and the camera, following the law:

$$M = \frac{q}{p} \tag{3.1}$$

where $p$ and $q$ are, respectively, the distance between the CCD and the pin-hole and the distance between the observed object and the pin-hole. The diameter $\phi$ of the hole determines the focal resolution $r$, at the expense of the intensity.

$$r \simeq \frac{(p+q)\cdot\phi}{q} \tag{3.2}$$

A typical pin-hole system consists of:

- Lead disk with the pin-hole, thick enough to block X-rays over the whole measured energy range. A typical pin-hole size used in the present measurements is 400 $\mu m$ diameter, 2 $mm$ thick.

- Set of collimators to reduce the X-ray scattering on the chamber walls, inducing unwanted contributions in the acquisition;
- Thin window of different materials and thickness, to block visible and UV light, depending on the energy range of interest;
- CCD camera;
- Shutter, usually external, positioned in front of the pin-hole.

Quantitative details of each component of the systems used in the present measurements will be described in the following sections.

## 3.2 Energy-space resolved radiation detection

The typical operating principle of an energy-resolved photon/particle detector working in single-event counting mode is, in a few words, that of collecting and measuring all the charge generated by each single impinging event.

Each detection generates an electrical signal which is processed and registered by the chain of preamplifier, amplifier, signal shaper/integrator and then digitizer, whose output values are (usually) proportional to the energy released on the detector from the impinging particle, allowing the amplitude-to-energy calibration [68].

Such systems are required to be very fast to guarantee the single-event online processing, otherwise the phenomenon of pile-up would occur, namely when more events are registered in the same collection process, losing the distinction of each respective charge information.

To give an example, a typical Silicon Drift Detector (SDD) has a readout rate $R_{readout}$ of the order of few MHz (peaking time $\sim \mu s$) allowing, in principle, a maximum counting rate $R_{events}$ of the same order of magnitude $\sim Mcps$ [68].

In practice, being the impinging radiation randomly time-distributed, it is usually recommendable to operate far from the pile-up condition, which means $R_{events} \ll R_{readout}$.

### 3.2.1 Overview on Charge Coupled Device (CCD) detectors

The CCD is a silicon detector divided into a matrix of pixels, commonly used nowadays in digital photography.

It is based on the capability of temporary storage the charge, released by the impinging radiation into the silicon crystal, for all the exposure time of a picture.

This is possible thanks to a proper doping profile of the silicon crystal, creating an electric potential well for each pixel.

These wells are electrically coupled together, allowing the sequential readout by the coupled-charge transfer between adjacent pixels [69].

**Readout of the stored charge** At the end of the exposure time all the deposited charge is shifted row by row by a pulsed electric signal to the edge of the chip, where it is collected by a sequential readout system, consisting on a signal amplifier, integrator and digitizer.

Such process is not suitable for fast single-photon acquisitions, since the total readout time for each frame collection is proportional to the total number of pixels, usually of the order of $10^6$. Consequently, being the low-noise signal processing frequency of the order of $\sim 1MHz$, the typical single-frame readout time for a CCD is of the order of few seconds.

Moreover, being the detector sensitive during all the readout process, a mechanical shutter is required to avoid the photon collection over the shifting image.

**Pixel charge diffusion** An incident X-ray generates a certain amount of electric charge on the CCD, which can spread into a cluster of neighbor pixels. This effect must be taken into account to preserve the energy information (see chapter 3.5).

### 3.2.2 Single-photon-counting on CCD detectors

The idea of using the CCD as a space-resolved spectrometer is based on the principle of accumulating on each frame the information of many photons impinging on the device for a short exposure time ($\sim ms$), then

collected in a single readout process. By this way, the majority of single-photon events are spatially separate and can be analyzed individually. The overlapped events are identified as pile-up and then discarded.

The required amount of data for a single measure is then distributed on a series of several acquisitions, each of them containing a relatively small number of events.

The pile-up probability is then proportional to the source intensity, to the single exposure time and to the area occupied by each event, usually spread over a limited group of pixels. Therefore, the correct setting of the exposure time must be evaluated in relation to the source intensity, optimizing the number of discarded events (pile-up) versus the required amount of data to be collected in the overall measure time.

It is important to notice that such optimization is mandatory, otherwise this kind of measurement could become excessively time-consuming.

Figure 3.2 shows a typical acquisition in SPhC, where the single and multiple events are well distinguishable as groups of pixels (namely, clusters).

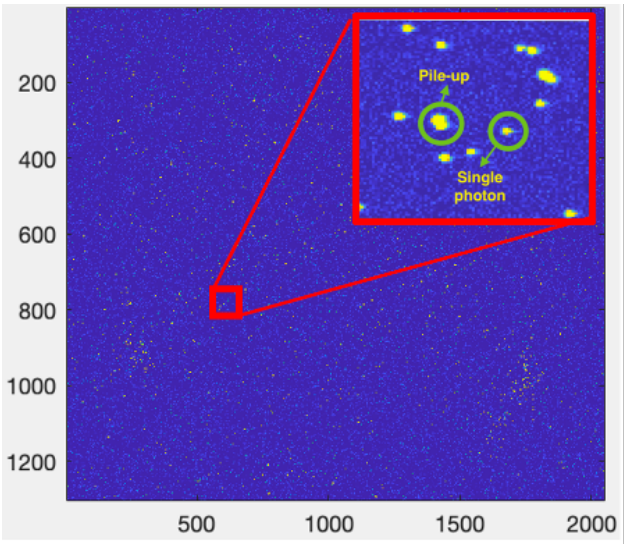


Figure 3.2: Single-frame acquisition in SPhC operating conditions. Zoom on a random portion to highlight the single vs multiple photon clusters of pixels.

The technique adopted to extract and calibrate the energy information from the images, required a specific analysis algorithm, on whose development a relevant effort has been spent during the last years [46, 48, 70].

The algorithm, written in MATLAB®, mainly performs the identification of each single photon event registered on a set of frames, using a package of imaging tools.

The output of such process is an array containing the impinging position of each photon event on the CCD matrix, the deposited energy information, and some geometrical features which can be helpful for the energy calibration and pile-up discrimination. The latter will be described in detail in section 3.5.

## 3.3 CCD pin-hole camera setup

The space-resolved X-ray diagnostic consists of a silicon CCD array detector coupled to a "camera obscura" which contains a set of lead collimators, including a $400\mu m$ pin-hole disk, and a Pt-Ir mechanical shutter. Such detector is specifically designed for professional and research low-noise applications, providing the X-ray sensitivity up to 30 keV, a cooling system working below $-90°C$ and the high-vacuum compatibility.

**Princeton SOPHIA-XO 2048B – 132 CCD camera** This camera is equipped with a $27.5 \times 27.5mm$ back-illuminated sensor, containing $2048 \times 2048$ squared pixels ($13.5\mu m \times 13.5\mu m$), with an intrinsic quantum efficiency in the $5eV - 30keV$ range. The sensor is equipped with a hybrid cooling system (air+liquid), reaching the lowest temperature of $-90°C$. The detector is controlled by its software (LightField®), which provides the tuning of the main operative settings (e.g. exposure time, gain, readout frequency, etc...) which will be described in the specific section (3.5). Figure 3.3 reports the camera device and the intrinsic quantum efficiency provided by the manufacturer (green line).

This kind of devices can be used in single photon counting acquisition mode as a space-resolved spectrometer, thanks to the very low-noise signal processing, thus determining a relatively slow readout ($T_{readout} \sim$

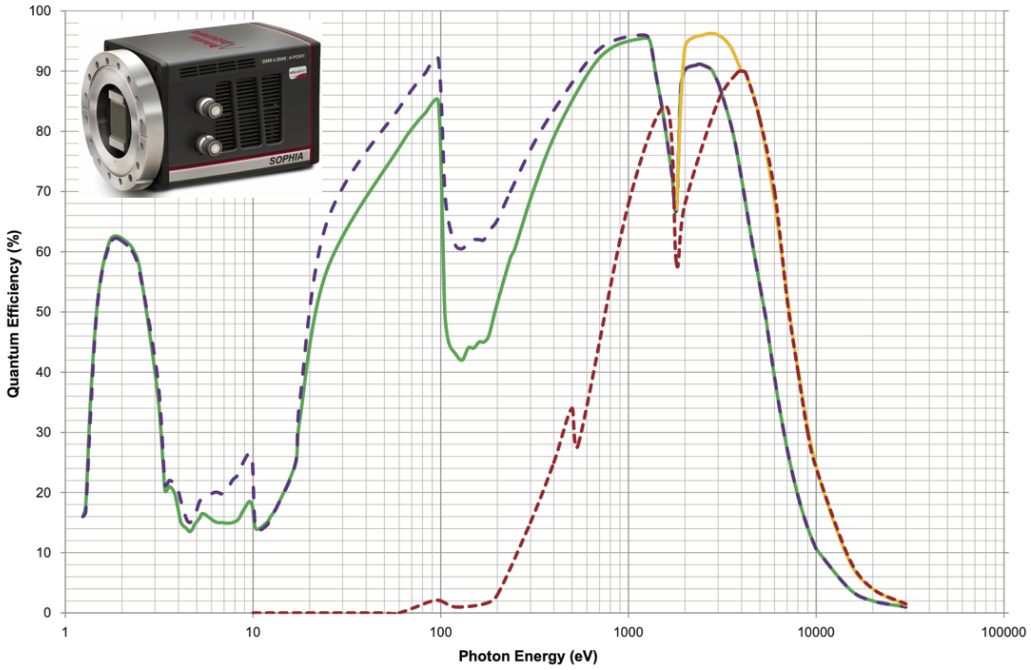


Figure 3.3: Princeton SOPHIA-XO 2048B - 132 CCD camera and respective quantum efficiency (green line)

$1 - 24s$). Such operating mode requires specific exposure conditions in relation with the observed source, which will be described in the respective section.

The energy-resolved information processing is not provided by the manufacturer, thus requiring the development of a specific analysis algorithm, to which a detailed section is dedicated (3.5).

**Pinhole camera and X-ray shutter** The CCD camera/SDD detector is coupled to a camera obscura, consisting of a specifically designed vacuum case, containing the X-ray shutter and multilayer lead collimator consisting of:

- Lead pinhole collimator: 2 mm of thickness, $400\mu m$ of hole diameter;

- Lead extra-shielding collimator: 1 mm of thickness, 2 mm of hole diameter;
- Al window $0.8\mu m$ thick, in order to block visible light and X-ray up to 450 eV.

A vacuum bypass preserves the thin window from pressure shock-waves.

The X-ray shutter is a platinum-iridium mechanical blade (Uniblitz XRS6 Pt-Ir), designed to stop X-rays up to 30 keV, with a minimum exposure time of 5 ms. The shutter can be triggered by the camera acquisition through a specific driver, compatible with logical TTL standard inputs. Figure 3.4 shows the vacuum case (left), the internal structure with the lead disks (middle), window and pinhole, and the x-ray shutter (right).

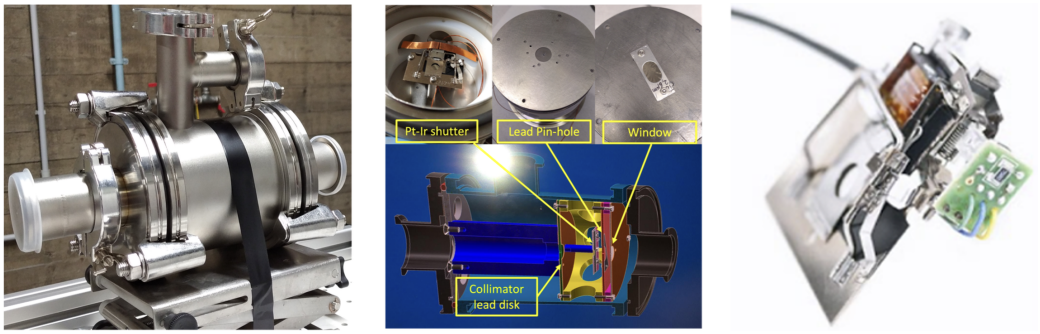


Figure 3.4: Vacuum case of the camera obscura (left), containing the multi-layer pin-hole + collimator and the X-ray transparent window (middle). View of the X-ray shutter device (right).

## 3.4 X-ray diagnostics test bench

A test bench for X-ray diagnostics development was set up at INFN-LNS to characterize the diagnostic instruments.

Particular attention was devoted at benchmarking the CCD device, whose suitability for spectrometric applications is not characterized by the manufacturer in terms of operating capabilities and inherent limitations. In fact, the CCD datasheets do not include any spectroscopic

features, that have to be determined in laboratory with ad-hoc measurements.

The test bench consists of a scattering vacuum chamber providing different lines of view for direct and scattered X-ray measurements, to be coupled with a portable X-ray tube source (Ametek Mini-X2, 70 kV, 10 W, Tungsten anode) shown in figure 3.5.

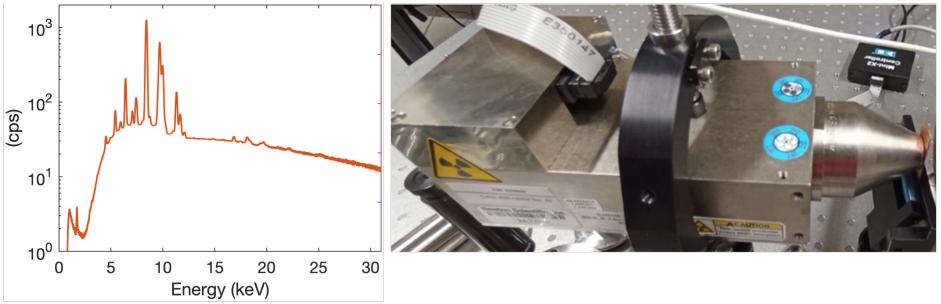


Figure 3.5: X-ray source Ametek Mini-X2, 70kV, 10W, Tungsten anode (right) - Emission spectrum (left) measured in vacuum with the SDD detector.

A fast Silicon Drift Detector (SDD) was provided as a spectrometric reference (Ketek VITUS H7LE), to be directly coupled to the vacuum system (figure 3.6).

**KETEK VITUS H7LE SDD detector** This detector is a silicon SDD with $7mm^2$ active area and $450\mu m$ thickness, providing a polymer AP3.3 window with a quantum efficiency range of $100eV - 30keV$. The detector has a maximum resolution of FWHM <129 eV @5.3 keV ($8\mu s$ peaking time). Figure 3.6 reports the detector quantum efficiency as provided by the manufacturer: on the left the full-range QE is reported with the $8\mu m$ Be window transparency, on the right the low-energy transmission of the polymer AP3.3 window is reported. The detector can operate in high-vacuum conditions.

Different targets (figure 3.7-left) were prepared to be irradiated and obtain different patterns of fluorescence lines, in order to investigate both spectroscopy and imaging performance of the CCD pinhole-camera.

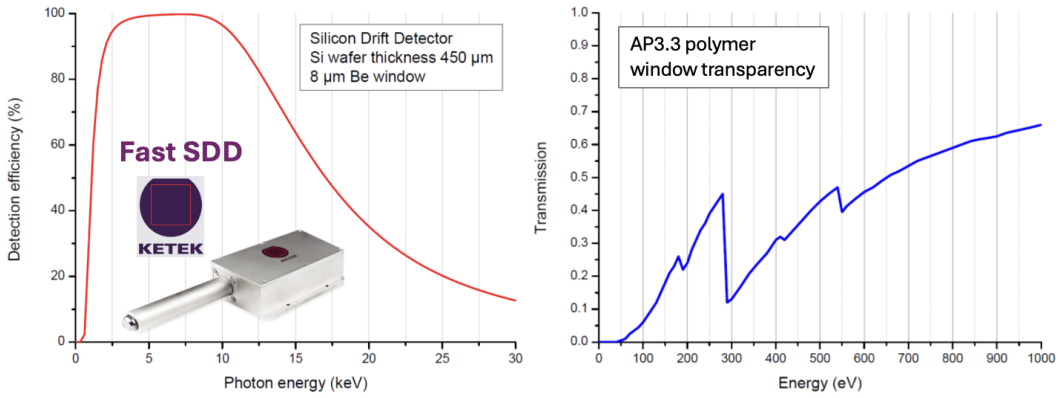


Figure 3.6: KETEK VITUS H7LE SDD detector quantum efficiency, provided with the reference $8\mu m$ Be window (left) - Transparency of the AP3.3 custom window at low energy (right).

Figure 3.7-right shows the scattering chamber with the X-ray tube and the CCD line mounted orthogonally for X-ray induced fluorescence (XRF) measurements. Inside the chamber the target was placed with a holder at 45° angle (middle).

Figure 3.7: Multi-elemental target, consisting of a Cu plate with Al, Ti, Fe, Ag, Sn, Ta, W, Au smaller targets (left) - detail of the target mounted inside the vacuum irradiation chamber (middle) - external view of the irradiation chamber with the X-ray source on the right and the CCD camera at the back (right).

Figure 3.8 shows the setups for direct detection of the X-ray source emission with the CCD and the SDD detector.

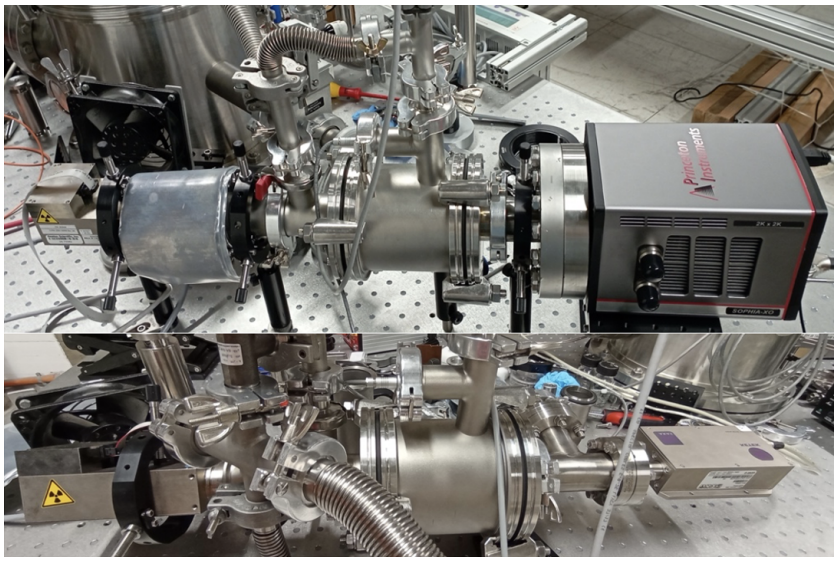

Figure 3.8: Setups for direct detection of the X-ray source emission through the pin-hole with the CCD (top) and the SDD detector (bottom).

## 3.5 CCD pin-hole camera characterization

A characterization study of an X-ray CCD detector was performed in laboratory by a specifically developed test-bench, mainly focused on the X-ray imaging and spectroscopy capabilities of the SPhC pin-hole camera technique.

The algorithm adopted for the SPhC analysis, working in Matlab®, is the result of a long development and optimization effort spent during the last years [46, 48, 70], in order to enhance the spectrometry and imaging performances of the CCD pin-hole camera.

Further improvements have been developed in the present work, concerning both the operative configuration of the instrument and several aspects of the analysis algorithm.

The study was focused on the following main aspects:

1. Operative configuration of the instrument;
2. Single-photon-counted data analysis;
3. Multiparametric energy calibration – energy resolution;
4. Spatial resolution characterization;
5. Time resolution: shutter characterization;
6. Pile-up analysis and statistical correction;
7. Efficiency calibration;
8. HDR imaging.

### 3.5.1 Operative configuration of the instrument

The main operative settings of the CCD were explored to find an optimal setup for long acquisitions in single photon counting mode.

The most relevant settings provided by the acquisition software are:

- Exposure time

- Charge collection mode [low noise/high capacity]
- Readout frequency [500$kHz$, 1$MHz$, 4$MHz$]
- Analog gain [Low, Medium, High]

A background acquisition was performed at different exposure times (10$ms$ and 60$s$) and low, medium, high gain values, characterizing the readout noise and dark current distribution.

The optimal gain setting was evaluated by irradiating a multi-element target, composed with pieces of Cu, Ta, Sn, Ag, Fe, Ti, Al.

The best configuration of "Charge collection mode" and "Analog gain" was determined as "Low noise – High gain", by the choice of the highest energy resolution and the widest dynamic range, being the charge collected at the maximum detectable energy quite far from the pixel well saturation. More quantitively, a rough energy calibration at the highest gain setting shows that a photon at the quantum efficiency tail of 30$keV$ generates a charge of 7000$ADU$, quite small compared to the maximum capacity of 65000$ADU$ (saturation value).

The acquisition software provides three settable values of the readout frequency parameter (500$kHz$, 1$MHz$, 4$MHz$), whose choice determines the total readout time for each frame. In principle, this parameter is proportional to the readout noise produced during the CCD readout, consequently it should be lowered for better spectroscopy performances. On the other hand, the readout time becomes longer for lower frequency values.

For this reason, the lowest settable value (500$kHz$) was excluded since the single frame readout requires 24 seconds, unsuitable for a typical experimental multi-frame acquisition.

A comparison of 1$MHz$ and 4$MHz$ acquisitions have been done, with a single frame readout time of 4.4$s$ and 1.2$s$ respectively. The resulting readout noise distribution width and energy resolution, expressed in Analog to Digital conversion Units (ADU), are shown in the table 3.1:

All the following study was then performed operating at 1 MHz readout frequency.

| **Readout frequency** | **Readout noise width (FWHM)** | **Energy resolution** @4.51$keV$ |
|---|---|---|
| $1MHz$ | $13.7ADU$ | $40ADU$ |
| $4MHz$ | $33.4ADU$ | $72.8ADU$ |

Table 3.1: Readout noise distribution width and energy resolution at two different settings of readout frequency.

### 3.5.2 Background analysis

Each dataset is usually acquired together with a background acquisition, consisting of a set of empty frames with the shutter closed and, possibly, with the X-ray source off. Such frames usually contain the readout noise generated by the coupled-charge collection, mainly depending on the readout frequency; the integrated dark current, depending on the exposure time and on the CCD set temperature; the impinging cosmic and ambient radiation. The adopted device also requires the subtraction of the readout bias pattern, namely a "zero" pattern necessary for the readout process, which can be measured from a background acquisition. The latter is shown in figure 3.9, reporting the bias value map expressed in ADU color bar.

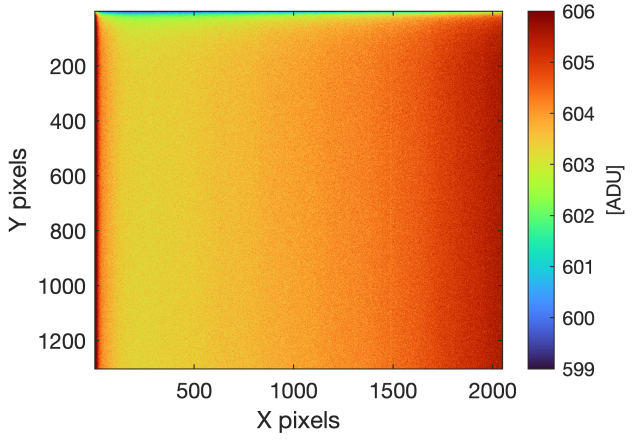


Figure 3.9: Readout bias pattern measured in a background acquisition without any sources.

The calculation of the bias pattern is obtained by averaging all the background frames of a short-exposed dataset, excluding the rare cosmic ray events by a rough application of the graphic cluster recognition function, described in the next subsections. The overall average frame is weighted with a 2D mask containing the information of the small regions eventually excluded by the presence of impinging radiation clusters (few events per frame).

The next step is the analysis of each data frame, starting with the subtraction of the bias pattern.

A histogram is generated from all the pixel data to determine the noise threshold for each frame.

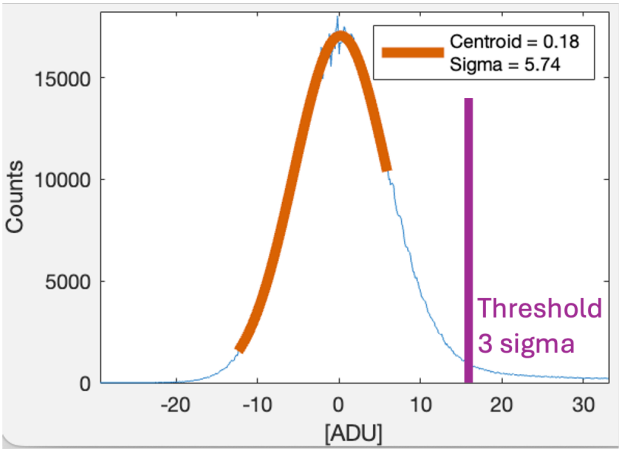


Figure 3.10: Noise distribution of a background acquisition (blue), fitted with a Gaussian curve (orange). Setting of the noise threshold at $3\sigma$ (purple).

A typical short-exposed frame for a single-photon measurement roughly contains a maximum of $\sim 10^4$ events, with an average surface of $\sim 10$ pixels each (assuming to frame a homogeneous source, properly magnified to optimize the sensitive area). Consequently, the number of pixels that contain data is about $\sim 10^5$, one order of magnitude less than the total number of $4.2 \cdot 10^6$ pixels. The majority of the pixels contain only the readout noise, so the maximum value of the histogram is centered on zero, with a predominant Gaussian distribution of the readout noise

values. The negative side of the distribution can only contain negative noise fluctuations, while all the significative information produces values higher than the positive half-width at half maximum (HWHM). For this reason, a Gaussian fit is generated in the asymmetric range of [-2·HWHM, HWHM] (roughly estimated), providing a precise evaluation of the width and mean value of such distribution.

Figure 3.10 shows the noise values distribution and the Gaussian fit (in orange) defined on the respective range.

Table 3.2 reports the number of noise events at different threshold values:

| **Threshold** | **Counts over threshold** |
|---|---|
| No threshold (all pixels) | $4.2 \cdot 10^6$ |
| 0 | $2.1 \cdot 10^6$ |
| $\sigma$ | $6.4 \cdot 10^5$ |
| $2\sigma$ | $9.2 \cdot 10^4$ |
| $3\sigma$ | $5.5 \cdot 10^3$ |

Table 3.2: Number of counts over different threshold values in a background acquisition.

### 3.5.3 Single-photon clusters identification

This part of the algorithm concerns the graphical identification of the single photon events on each frame, based on the connectivity of neighbor pixels. It requires the insulation of the regions (namely, clusters) involved on each single photon interaction, by the application of a threshold, whose value is not easy to be exactly estimated in advance and trades-off two different consequences: on the one hand, its value determines the probability of unwanted connections between clusters due to over-threshold noise spots; on the other hand, it affects the quantity of under-threshold missed information, to be integrated as the total signal produced on each event.

Figure 3.11 highlights the application of a threshold to discriminate a single-photon cluster from the background noise.

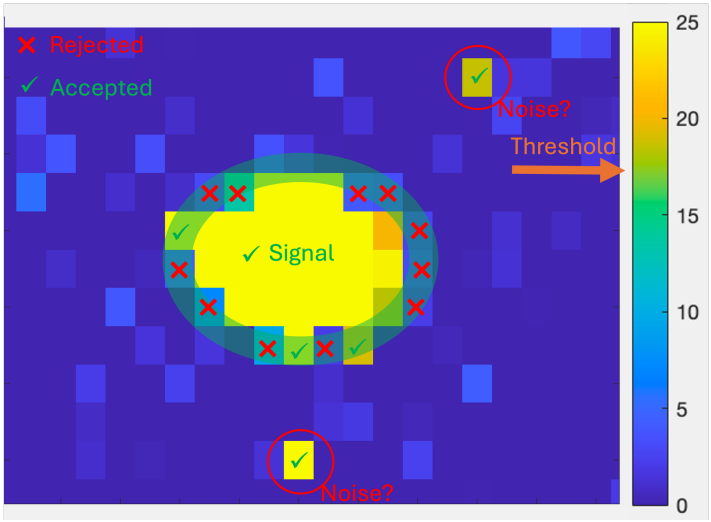


Figure 3.11: Image of a single-photon cluster surrounded by the noise over and under threshold. Color bar properly set to obtain a color discrimination at value 18, highlighting the issue of discriminating noise from the cluster tail.

An empirical evaluation has been done to fix this threshold at $3\sigma$, at whose value the number of noise spots over threshold is usually lower (in proper SPhC exposure conditions) than the number of significative photon events, giving a reasonably low probability of unwanted clusters connection due to the noise spots. The correction of the under-threshold missing information will be described in detail in the next paragraphs.

All the clusters are collected frame by frame and labelled with all the relevant information (features):

- Area (number of pixels)
- Sum (digitalized collected charge summed over area)
- X, Y centroid position
- Eccentricity, Major and minor axis of a fitting ellipse
- Number of local maxima

Moreover, a "shape parameter" is defined for each cluster by the ratio between the maximum pixel value and the integral over the whole surface, which is correlated to the collected charge spread.

It is now considered the data sample obtained by the X-ray Fluorescence (XRF) measurement on the multi-element target, to discuss the single photon analysis output.

The energy information can be resumed by the 2D histogram shown in figure 3.12-left, reporting the clusters integral (Sum), expressed in ADU, on the X-axis and the cluster area (number of pixels) on the Y-axis. The bin-size is defined as one unit on both axis.

The histogram is filled with all the data having one local maximum, since data with more local maxima are strongly correlated to the pile-up of multiple photons and have been therefore discarded.

No relevant energy information is contained in the clusters of one-pixel dimension, which instead constitute most of the residual noise. Therefore, these data have been also excluded from the analysis.

On the right a reference energy spectrum is shown, obtained by the silicon drift detector (SDD) coupled to the same field of view of the CCD, in the same experimental conditions.

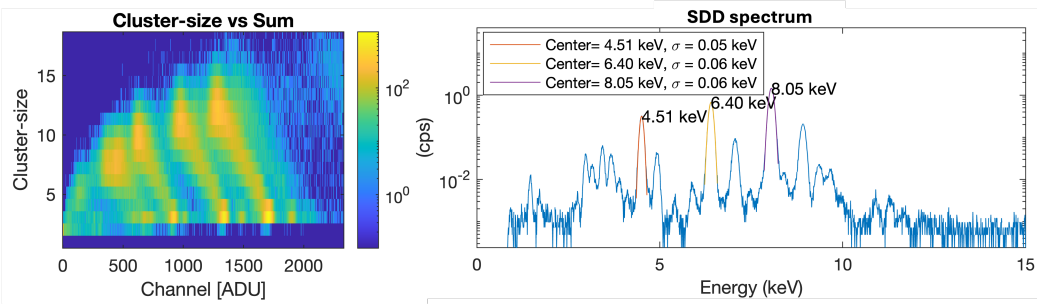


Figure 3.12: 2D histogram of the cluster integral on the X axis and the cluster area (number of pixels) on the Y axis, filled with data having one local maximum (left) - Energy spectrum measured with the SDD detector in the same field of view of the CCD.

The energy calibration of such information is not trivial and will be discussed later, although the statistical arrangement on the 2D histogram can be correlated to the main fluorescence lines emitted from the target.

The latter is then confirmed by considering the space-resolved imaging information.

Figure 3.13 shows the picture of the multi-element target (right) coupled to a pseudo-colors X-ray image (middle), obtained by a cut on each connected region of the 2D histogram (left), to which a respective color is assigned. A table with the main fluorescence lines is shown on the bottom, highlighting the respective lines in the same pseudo-colors.

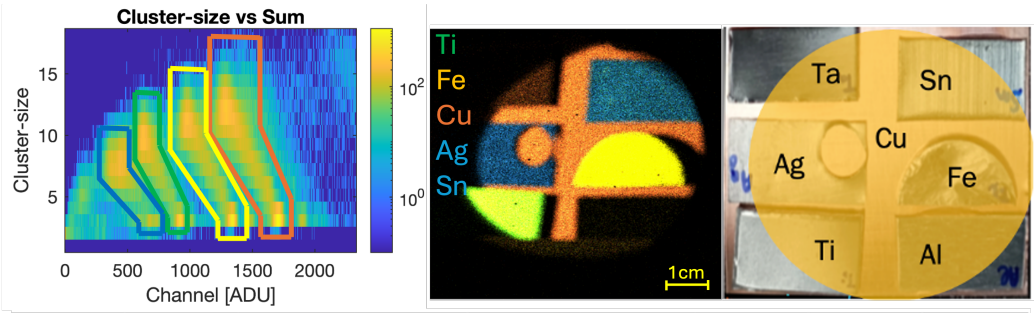


| Element | $K\alpha_1$ | $K\alpha_2$ | $K\beta_1$ | $L\alpha_1$ | $L\alpha_2$ | $L\beta_1$ | $L\beta_2$ | $L\gamma_1$ |
|---|---|---|---|---|---|---|---|---|
| 22 Ti | 4,510.84 | 4,504.86 | 4,931.81 | 452.2 | 452.2 | 458.4 | | |
| 26 Fe | 6,403.84 | 6,390.84 | 7,057.98 | 705.0 | 705.0 | 718.5 | | |
| 29 Cu | 8,047.78 | 8,027.83 | 8,905.29 | 929.7 | 929.7 | 949.8 | | |
| 47 Ag | 22,162.92 | 21,990.3 | 24,942.4 | 2,984.31 | 2,978.21 | 3,150.94 | 3,347.81 | 3,519.59 |
| 50 Sn | 25,271.3 | 25,044.0 | 28,486.0 | 3,443.98 | 3,435.42 | 3,662.80 | 3,904.86 | 4,131.12 |

Figure 3.13: Cuts on the 2D histogram over the main resolvable characteristic emission lines, highlighted in different respective colors (left) - pseudo colors image of the emission lines (middle) - picture of the target with the circular print of the cone of view - Table with the main emission lines of the selected elements (bottom).

The information about Ti, Fe, Cu K-fluorescence is well resolved both in energy (ADU channels) and in space, while the L-fluorescence lines of Ag and Sn are not well resolved and therefore represented in the same color (blue).

The structure of the Cluster-size vs Sum histogram highlights a peculiar behavior of the single-photon grouped charge, mainly populating two series of data: low-sized clusters with higher resolution and high-sized clusters with lower resolution, the latter presenting a non proportional shift towards lower values, as shown in figure 3.14. The two regions are

linked with a lower population presenting hybrid features. The two spectra on the right are the respective ADU-axis projections of the regions selected with respective colors (pink and orange).

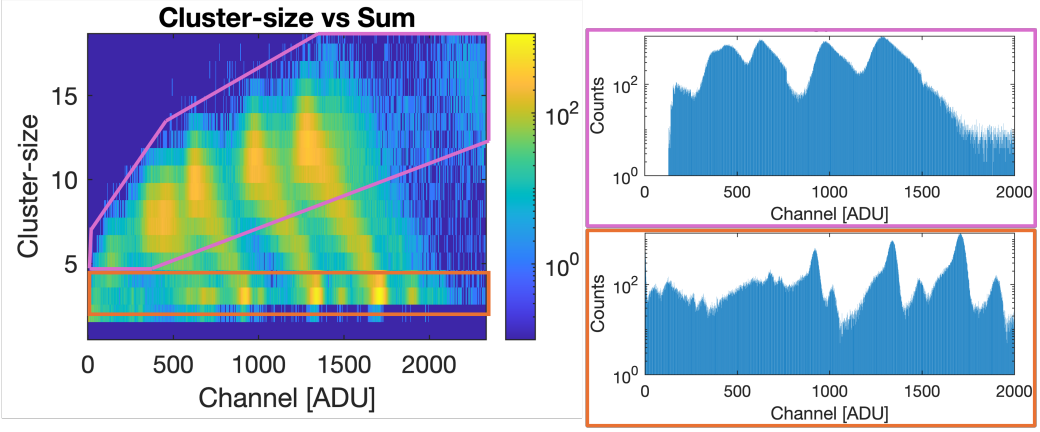


Figure 3.14: High and small-sized clusters on the Cluster-size vs Sum histogram, respectively generating low (pink) and high (orange) energy resolution spectra.

**Extension of clusters area** In order to correct the missing under-threshold information, an extended integral is further defined over the under-threshold pixels inside the ellipse, having a fixed eccentricity and an extension factor optimized ad-hoc.

This correction allows the inclusion of more information in the charge integral, reducing the shift towards lower values; on the other hand, it increases the statistical fluctuation of the integral over a higher number of pixels ($\sigma_{tot} = \sqrt{N \cdot \sigma_i}$). The extension factor has been optimized to the value 0.65, in a trade-off between the resolution loss ($\sigma$) and the shift reduction ($\Delta$), by a proportional reduction of the ellipse axes conserving the eccentricity. Figure 3.16 shows the effect of such correction in terms of resolution and shift of the Cu fluorescence line data.

As shown in the picture, the residual shift is still resolved ($\Delta$>FWHM) and will be corrected with a parametric energy calibration (see next subsection). A further extension seems to affect mostly the resolution than the shift compensation.

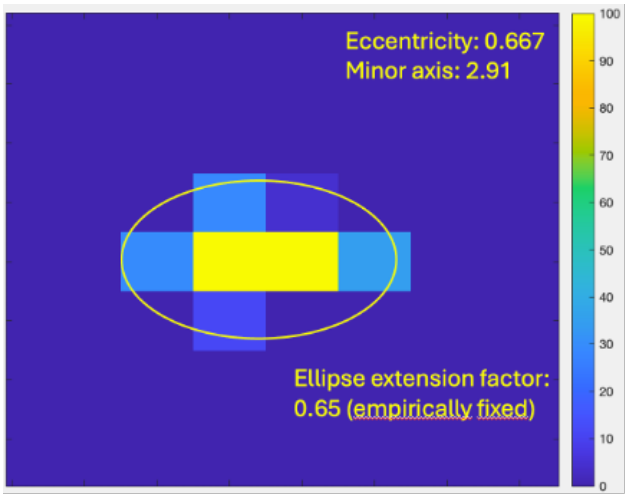


Figure 3.15: Example of cluster extension over a fitting ellipse surface.

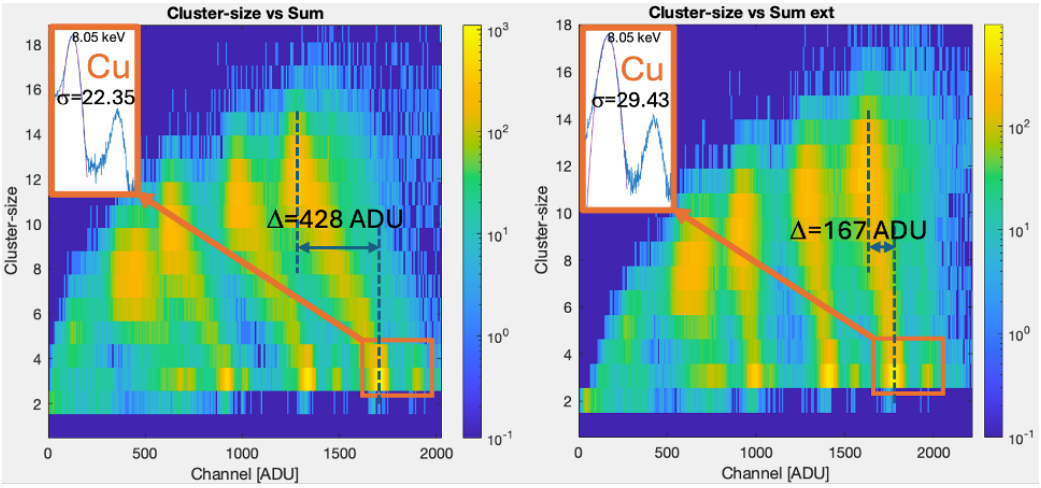


Figure 3.16: Effects of the cluster extension correction on the Cluster-size vs Sum histogram: original data (left) - after correction (right). The Cu line (8.05 keV) best resolution $\sigma$ of small-clusters data and shift $\Delta$ are reported on the image.

### 3.5.4 Monte Carlo simulation of a multi-frame dataset

A Monte Carlo simulation was developed to support the latter correction, confirming the assumptions about the effects observed in the previous paragraph. A simplified 1000 frames dataset was simulated by a model having the following features:

- Each frame is generated with a pre-existing random gaussian-distributed noise pattern, matching the experimental statistical spread ($\sigma_{noise} = 5.8AU$; FWHM = $13.7AU$).
- A fixed number of random impinging events (clusters) is generated assuming a 2D asymmetric gaussian shape, defining a homogeneous distribution of the gaussian widths $\sigma_x, \sigma_y$ that matches the resulting over-threshold surface with the experimental cluster-size range [2 - 30 pixels].
- The integral value of each 2D gaussian cluster, being the total charge of each event, is generated in a simplified bremsstrahlung + line emission distribution model, composed by the sum of a continuous exponential distribution with a series of gaussian peaks ($\sigma_{intrinsic} \simeq 2\%$) at several energy values.

The results of such simulation reproduce the same effects shown in the measures, confirming that the shift $\Delta$ explained in the previous paragraph origins from a partial collection of the total charge on each cluster, depending on the cluster's geometrical features combined with the background noise and threshold set. Figure 3.17-left shows the simulated ADU spectrum (orange) and the respective measure applied to the simulated data (blue), using the cluster-recognition algorithm. Figure 3.17-right shows the simulated 2D histograms ADU vs. Cluster size.

The variation of the $\sigma_x, \sigma_y$ parameters of the clusters shape and of the noise parameter $\sigma_{noise}$ determines respective variations of the energy resolution and shift $\Delta$, allowing to reproduce the experimental data features.

In perspective, this simulation tool could be optimized to investigate the multiple event pile-up, studying the complex distribution of geometrical combinations due to the overlap of several clusters. By this way, the correlation between the number of local maxima and the effective

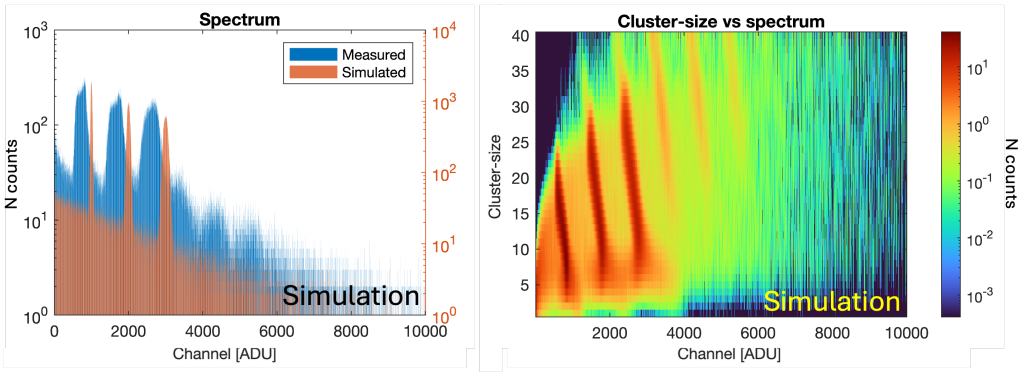


Figure 3.17: Simulated ADU spectrum in orange and respective output of the clustering algorithm in blue (left) - Cluster-size vs spectrum 2D histogram on simulated data (right)

number of overlapping events could be precisely estimated, to better apply statistical corrections to the SPhC data. Such study would require a very precise estimation of the clusters' geometrical extension, being such feature non-linearly propagating errors through the big pile-up clusters structures ($N_{local-maxima} \simeq 50$).

### 3.5.5 Multiparametric energy calibration

The residual correction of the charge information is obtained in the energy calibration process, taking into account both the integrated ADU value of the charge sum and some features about the charge spread over single-photon clusters. This correction is more efficient if combined with the one described in figure 3.16, being the residual value of $\Delta$ relatively small to be corrected.

As described in paragraph 3.5.3, a "shape parameter" was defined in the single-events labelling, as the ratio between the maximum pixel value and the integral over the whole cluster surface. This parameter results to be correlated to the cluster-size, as proved by the similarity of the 2D histograms of Cluster-size vs Sum and Shape parameter vs. Sum (figure 3.18).

The shape parameter, moreover, better resolves the information about low and high charge resolution data distinction. The energy calibration

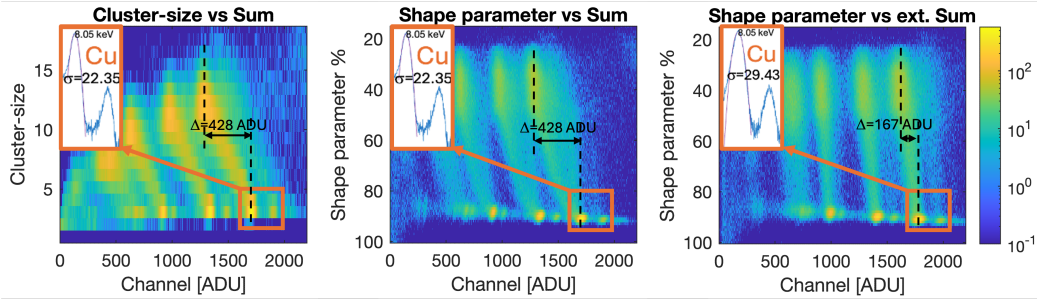


Figure 3.18: 2D histograms comparison of the cluster-size vs spectrum histogram (left) with the newly-defined "shape parameter" vs spectrum with and without the cluster-extension correction (middle and right).

is so defined specifically for different regions of the 2D histogram (figure 3.18-right, shape parameter vs extended sum). In particular, a low-sized clusters region is defined for Size < 6, mainly containing the statistics of the lower region of the histogram (Shape parameter $\gtrsim 70$).

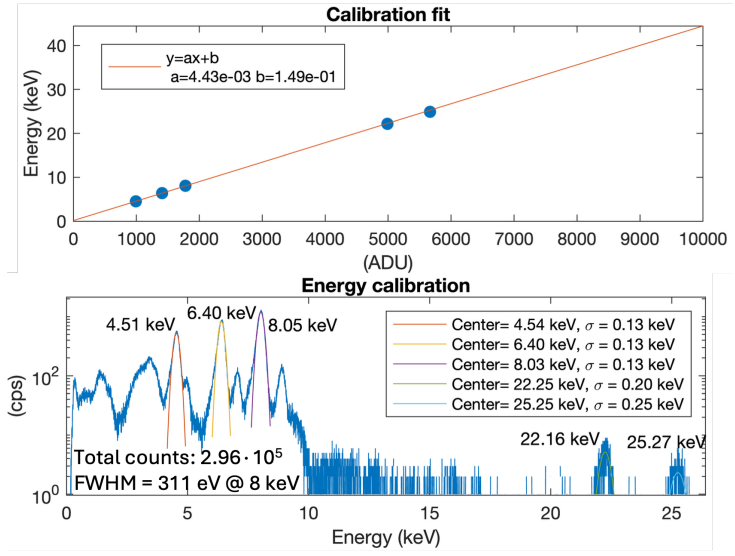


Figure 3.19: Linear energy calibration fit on the high-resolution spectrum. Data from extended clusters.

A linear calibration is defined on the main fluorescence peaks: $Ti - K\alpha$, $Fe - K\alpha$, $Cu - K\alpha$, $Ag - K\alpha$, $Sn - K\alpha$ obtaining the energy resolution

($\Gamma_{FWHM} = 2.355\sigma$) of $311eV$ at $8KeV$ and $470eV$ at $22keV$.

Figure 3.20 compares the Shape parameter histograms of the low-sized clusters (Size < 6) with and without applying the cluster-extension criterion.

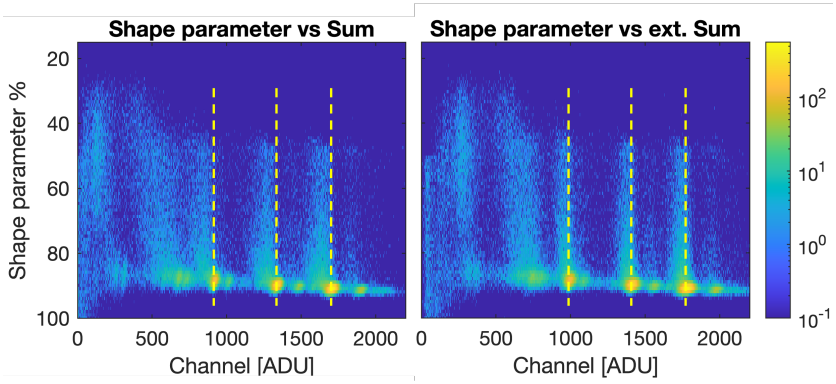


Figure 3.20: Effect of the small-clusters selection (Size < 6) in the "shape parameter vs spectrum" histogram with (right) and without (left) applying the cluster-extension criterion.

The calibration on the not-extended clusters sum gives higher resolution ($\Gamma = 240eV$ at 8 keV), although the spectral information is affected by the presence of non-gaussian broadening causing a “shoulder” artifacts, visible on the fluorescence peaks.

Therefore, the extended cluster calibration is more accurate although having a worse resolution.

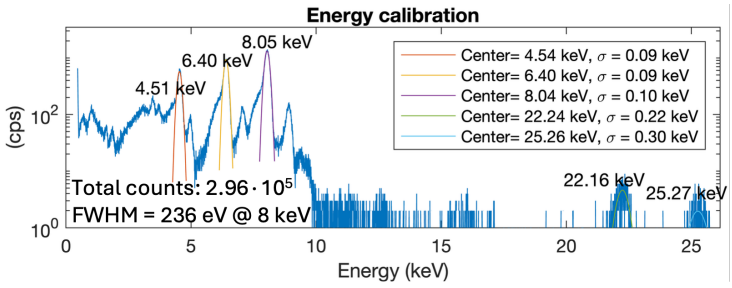


Figure 3.21: Energy calibration on small clusters without the extension correction: highest resolution.

Figure 3.21 shows the calibration on the latter information.

The calibration of the high-sized clusters (size > 5) requires the inclusion of the shape parameter information by a study of the fluorescence lines on the 2D histogram.

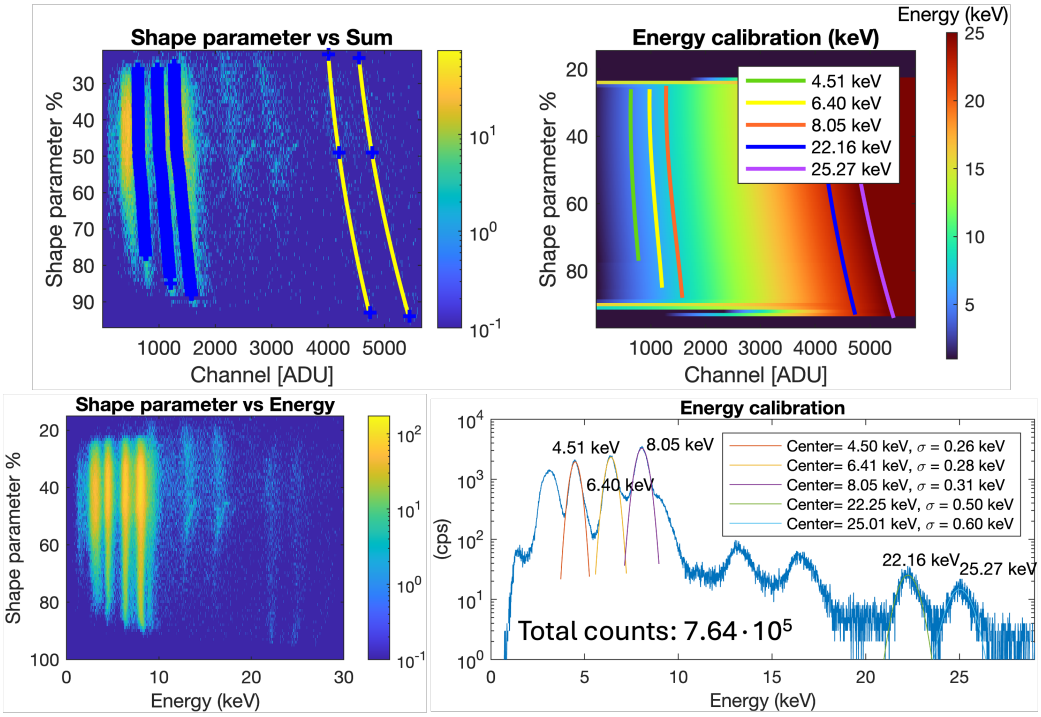


Figure 3.22: Multi-parametric energy calibration on bigger clusters (size > 5): shape-parameter vs spectrum histogram (extension correction applied), with centroid lines determined by polynomial fit (top-left) - 2D calibration fit (energy values on the color bar) (top-right) - calibration result on the 2D histogram (bottom-left) - resulting energy-calibrated spectrum (bottom-right)

Each calibration line is cropped on the histogram (figure 3.22-top-left), then a gaussian fit over the ADU-axis defines the center of the distribution at each shape-parameter value. A quadratic fit is obtained to interpolate the centroid line (no extrapolation is defined out of the fit range). The energy calibration is then obtained for each value of the shape-parameter, by a polynomial fit of degree $\leq 2$, according to the available number

of calibration points along the horizontal line (figure 3.22-middle). The resulting energy spectrum is shown in figure 3.22-bottom, with the energy resolution of 730 eV at 8 keV.

The total spectrum can be now defined by the sum of the two results including all the statistics, obtaining an intermediate value of energy resolution ($\sigma = 640eV$ at 8 keV) (figure 3.23).

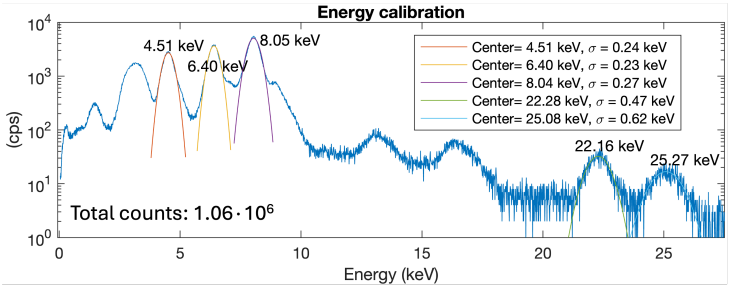


Figure 3.23: Overall energy spectrum including both high- and low-resolution data.

In summary, the collected data is distributed into low (730 eV @8keV) and high (311 eV @8keV) energy resolution populations, whose choice can be useful depending on the need of spectroscopy applications (resolution vs statistics).

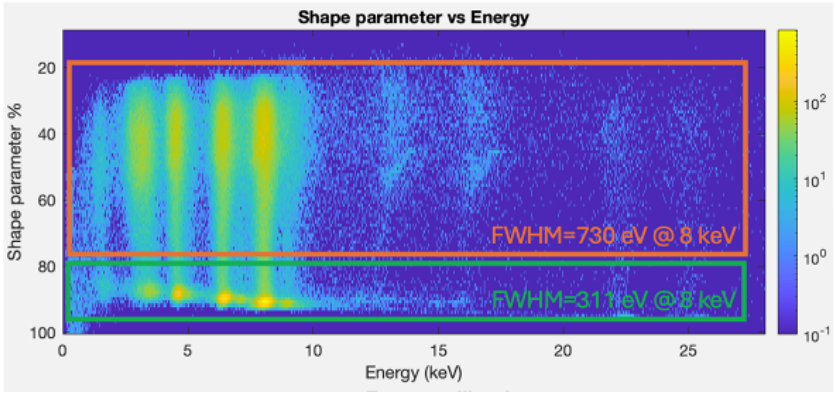


Figure 3.24: Summary of multi-parametric energy calibration: shape-parameter vs. energy histogram (left) - low and high-resolution energy spectra (right)

### 3.5.6 Time resolution: shutter characterization

The shutter response has been characterized by a dedicated measurement using a LED source and a diode detector sensitive in the visible light range, with a time response of $\sim 10\mu s$. The shutter was triggered with a pulse generator spanning from 4 to 180 ms of exposure time and the detector signal was acquired by a digital oscilloscope. Figure 3.25 reports a series of acquisitions at different pulse times showing the respective amplitude vs time track from the oscilloscope. The opening delay $t_0 = 3.51$ ms and the opening time $t_{open} = 1.16ms$ (respectively defined between 10% and 90% of the total amplitude) don't show any dependance on the pulse duration, while the closing delay and duration depend on it.

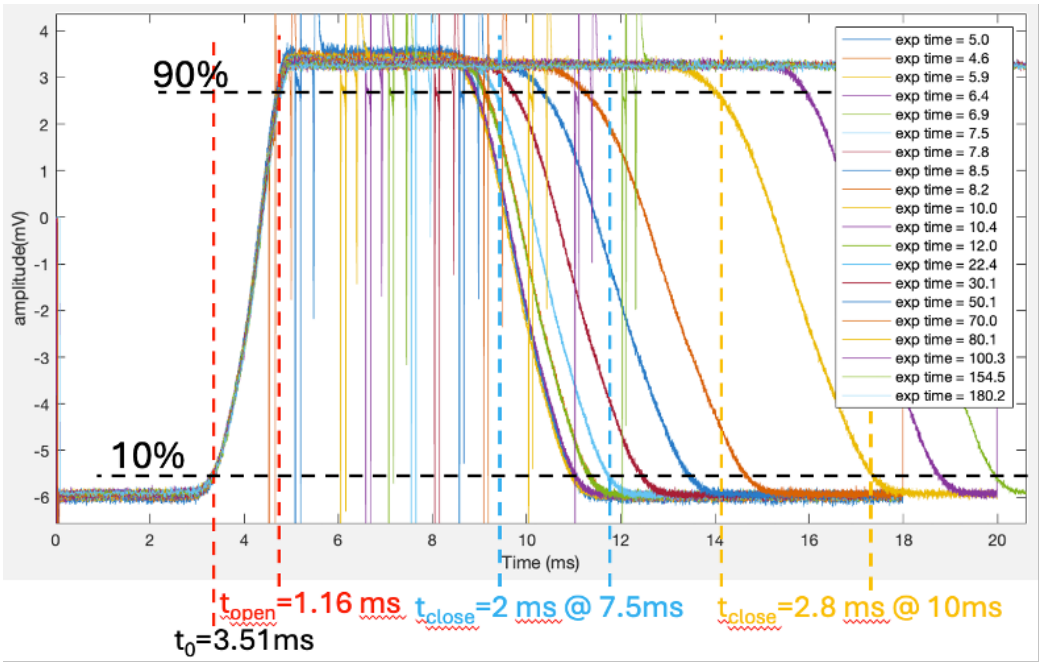


Figure 3.25: Shutter response at several logical exposure settings. The t=0 corresponds to the logical opening trigger. Transfer time on opening and closing are reported on the picture.

Figure 3.26-left, shows the effective exposure time at 50% ($t_{eff}$), 10% ($t_{10\%}$) and 90% ($t_{90\%}$) of the total amplitude versus the logical input pulse duration. It can be noticed that the shutter response is limited at 6 ms,

under which value the effective exposure time doesn't change. The shutter response at lower values was not reported, since irregular behaviors and partial openings were observed at pulses shorter than 3 ms.

Figure 3.26-right shows the shutter closing time vs pulse duration, defined similarly to the opening time.

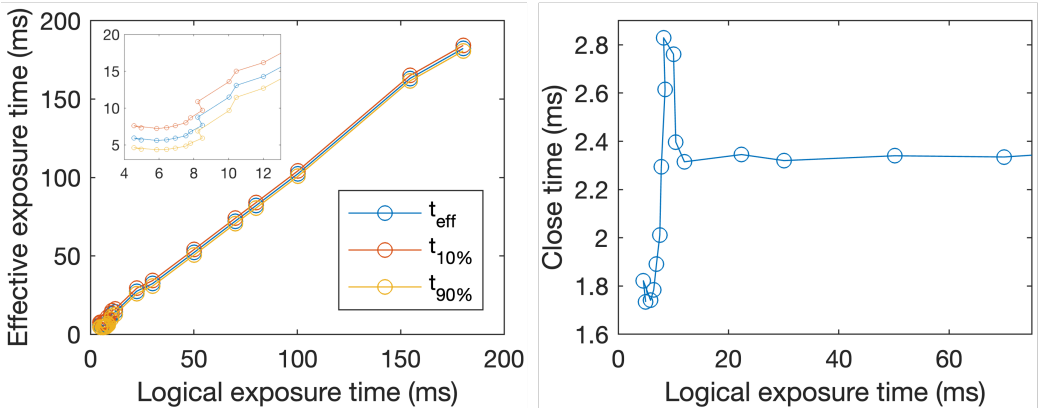


Figure 3.26: Effective exposure time (left) and transfer time on closing (right) reported at several logical exposure values.

For the sake of the present measurements, being the cone of view aperture very small ($\sim 3°$) and the distance between the pinhole and the shutter $d = 8.7mm$, the intersubsection with the shutter plane is a circle of $0.48mm$ diameter (7.5% of the shutter size), thus determining negligible transient times while opening and closing the field of view.

The exposure time can be easily defined as the effective opening time above 50% of shutter aperture. It is rather important to consider the response delays, which significantly affect the CCD exposure after the trigger and, particularly, during the first few milliseconds of the readout processes.

### 3.5.7 Efficiency calibration

The intrinsic quantum efficiency of the CCD detector is provided by the manufacturer, being the probability of an X-ray photon detection in relation of its energy.

The SPhC analysis algorithm applies strong selection criteria on detected data, which heavily affects the statistics. Such criteria are in part data-dependent and in part connected to the data processing constraints (i.e. the cluster-size selection which determines the choice of higher and lower energy resolution).

Statistical corrections can be defined to overcome the data-dependent contribution on the total detection efficiency and, on the other hand, an effective quantum efficiency could be defined to estimate the data-processing contribution, in principle data-independent.

This can be done by comparing the processed data with a reference instrument as a benchmark, providing an absolute efficiency calibration.

A Silicon Drift Detector (SDD) was so used to acquire reference data, reproducing a measurement in the same optical conditions.

A direct line of sight of the X-ray source coupled with the pinhole system was provided, optimizing the magnification to maximize the CCD imaging performance (the wider is the irradiated surface, the smaller is the photon flux density which causes pile-up). Then the SDD detector was coupled to the same cone of view, considering the different detector surface which constrains the distance from the pinhole. Being the line in vacuum ($P = 2.8 \cdot 10^{-2} mbar$), the air absorption along the line of sight is negligible.

An acquisition of 5500 frames has been done with the CCD detector at the exposure time of 30 ms, with the X-ray source set at 50 kV, $50\mu A$, measuring a total of $1.77 \cdot 10^7$ photon counts.

The SDD acquisition was performed in a shorter line of sight setting the X-ray source current at $5\mu A$, being the counting rate at $50\mu A$ at too high for the instrument.

The linearity of the source emission was verified, as shown by the plot of the total counts over the source current (figure 3.27-right).

The energy spectrum measured with the SDD is shown in figure 3.28, where the efficiency correction was obtained considering the Q.E. factor,

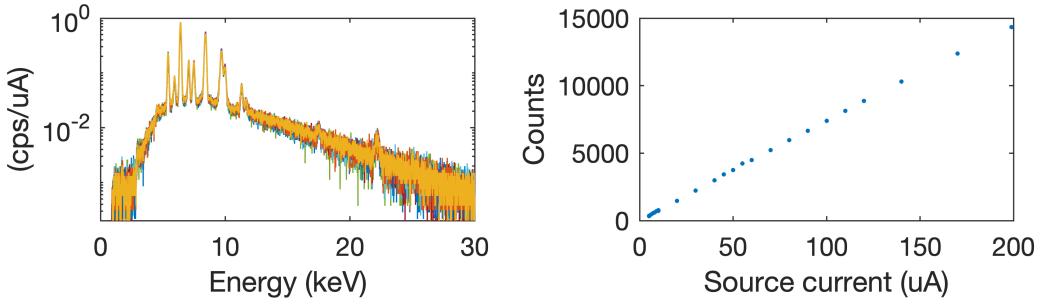


Figure 3.27: Linearity response check on the X-ray source: energy spectrum divided by the set current (left) - counting rate in function of the source current (right).

provided by the detector's manufacturer, and the transparency of the 800 nm thick Al window.

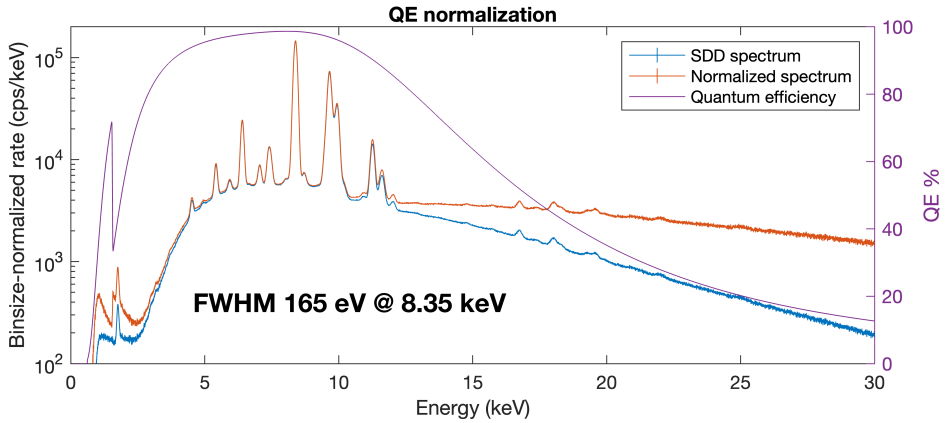


Figure 3.28: Energy spectrum measured by the direct exposure of the SDD through the pin-hole (blue) - detector quantum efficiency (violet) - Q.E. normalized spectrum (orange).

The spectrum is composed of a continuous bremsstrahlung and a line emission component, containing the L-M fluorescence lines of the W anode and the K lines of Cr and Fe of the steel body.

The CCD data consists of the energy and space-resolved information, distinguishing the energy spectrum of the whole dataset and of the small

cluster-size portion of data (higher resolution), obtained by the technique explained in the previous paragraphs. Being the latter quite interesting in order to enhance the high-resolution spectroscopic application, the efficiency calibration has been performed separately on both the data sets.

Figure 3.29 shows the full-energy image on the left and the energy spectra on the right, distinguishing the total one from the low-cluster-size one.

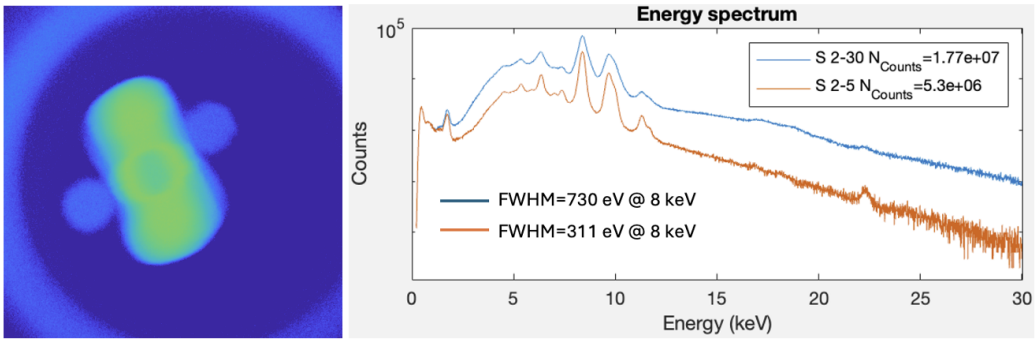


Figure 3.29: Image of the X-ray tube emission acquired with the pin-hole camera (left) - low and high resolution energy spectra (right).

**Pile-up analysis and statistical correction** The data-dependent contribution on the statistics should be firstly considered: indeed, the algorithm identifies events with only one local maximum ($N_{loc.-max.} = 1$) and discards all others ($N_{loc.-max.} > 1$), which have a high probability of containing more than one event.

Preliminary results from the aforementioned Monte Carlo simulations suggest, to a first approximation, a proportionality coefficient of about $c = 1.15$ between the number of local maxima and the effective number of events contained within a single cluster.

A typical distribution of the number of local maxima is shown in figure 3.30, corresponding to an acquisition of 1500 frames with an average event density per single frame of $4 \cdot 10^{-3}$ events per pixel.

The following study aims to map and quantify the discarded pile-up events, for which no energy calibration can be applied.

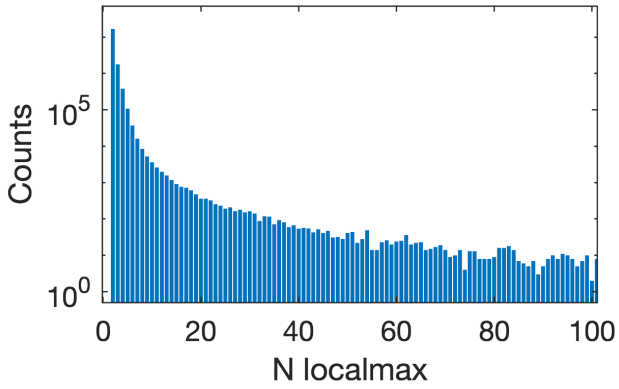


Figure 3.30: Typical distribution of the number of local maxima for a SPhC dataset of 1500 frames with an average event density per single frame of $4 \cdot 10^{-3}$ events per pixel.

All the pile-up clusters having $N_{loc.-max.} > 1$ are weighted with the effective number of impinging events and collected in a pile-up-weighted map, which represents the image of the not-photon-counted discarded events.

The ratio between this map and the one of all the events ($N_{loc.-max.} \geq 1$) represents the pile-up probability map ($P_{pile-up}$), as defined in the following equation:

$$P_{pile-up} = \frac{\sum_{i=2}^{N_{max}} Img(N_{loc.-max.} = i) \cdot c \cdot i}{\sum_{i=1}^{N_{max}} Img(N_{loc.-max.} = i) \cdot c \cdot i} \tag{3.3}$$

Figure 3.31 shows the image of the accepted events $N_{loc.-max.} = 1$ on the top-left, the pile-up ratio $P_{pile-up}$ in the middle and the corrected image multiplied by the correction factor on the top-right.

At the bottom, the full-frame energy spectra before and after the correction are reported in blue and orange, respectively.

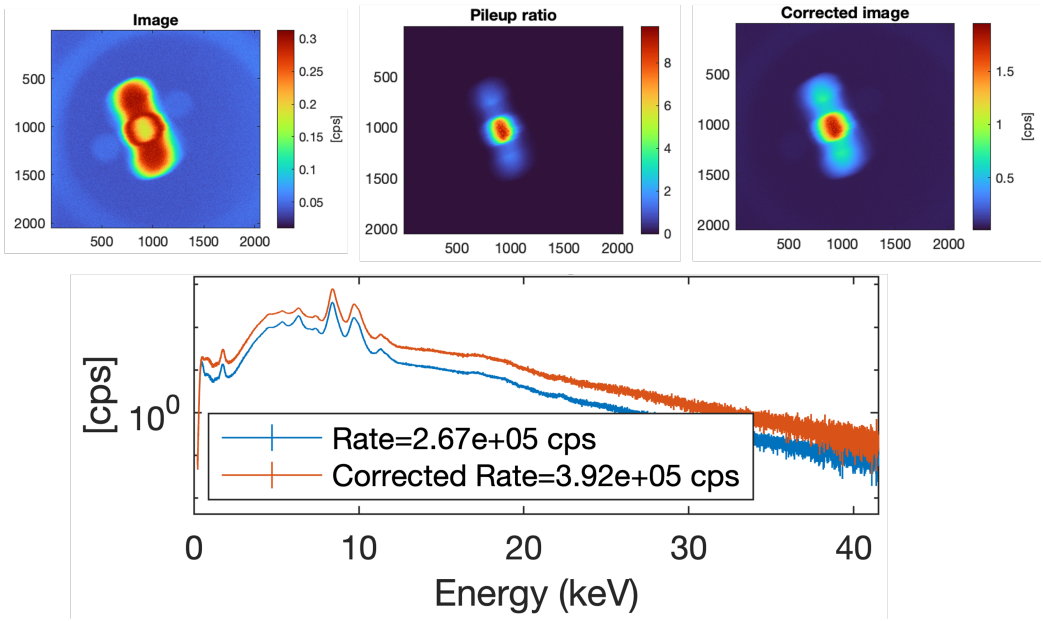


Figure 3.31: Image of the events having $N_{loc.max}$=1 (left) - calculated pile-up ratio map (middle) - pile-up corrected image (right) - energy spectra before and after the correction (bottom).

**Effective efficiency estimation** After this correction, a spectral normalization factor is defined on a set of energy values by the ratio between the CCD and the SDD spectra sum into the respective energy intervals (both the spectra are normalized with the intrinsic quantum efficiency of the respective instruments). Figure 3.32 summarizes the procedure.

The SDD and CCD spectra are shown respectively in orange and blue (the CCD intrinsic quantum efficiency is drawn in green and refers to the right y-axis). The normalization factor defined on a set of energy values is shown in red circles with respective error bars, referring to the right y-axis.

Due to a different energy resolution, the calculation has been done for few well-resolved fluorescence lines and in few regions of the continuous spectrum (the energy range of each point is highlighted in pink). The normalization factor is then interpolated along the overall energy range (green line with error bar – right y-axis).

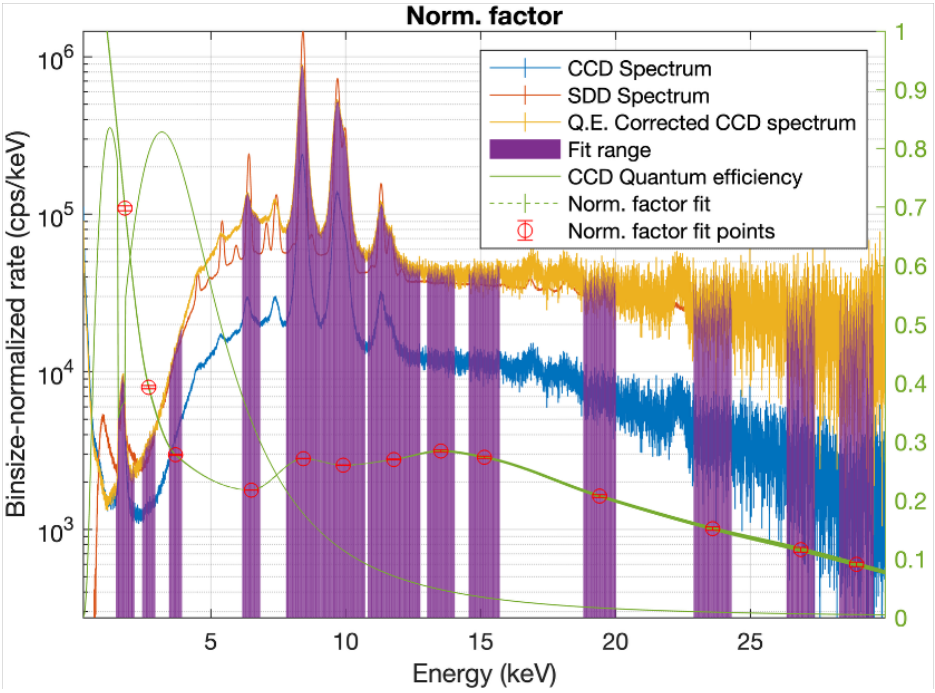


Figure 3.32: Summary of the effective efficiency calculation: SDD and CCD spectra in orange and blue, respectively; CCD intrinsic QE reported in green (referring to the right y-axis). Fit points reported as red circles, defined as the ratio of the two spectra into the respective energy ranges (in violet). Normalization factor fit reported in green with error bars. The effective quantum efficiency is then the product of the two efficiencies. The resulting CCD spectrum after correction is reported in yellow, overlapping the SDD reference.

The resulting CCD spectrum, corrected with the total effective efficiency, is shown in yellow.

The quality of this result can be evaluated by comparing the latter CCD spectrum with the SDD reference spectrum, according to the consequences of having two different energy resolutions (not-resolved fluorescence lines contribute to increase the continuous background, introducing an offset between certain regions of the two spectra).

The effective quantum efficiency is so defined as the product between the intrinsic one and the newly defined normalization factor, and can be

interpreted as the probability of a photon event to be detected, recognized by the algorithm and produce a high-resolution cluster with a size equal or smaller than 5.

This calibration method was then applied to the multielement target fluorescence dataset, comparing the CCD spectra obtained in the low (big clusters) and high (small clusters) resolution configurations, (figures 3.21, 3.22) with the reference one obtained with the SDD.

Figure 3.33 shows the SDD spectrum on the top and the couple of CCD spectra on the middle, together with the respective intrinsic QE. On the bottom, the couple of low- and high- resolution CCD spectra are shown together with the respective effective efficiency (Norm. factor).

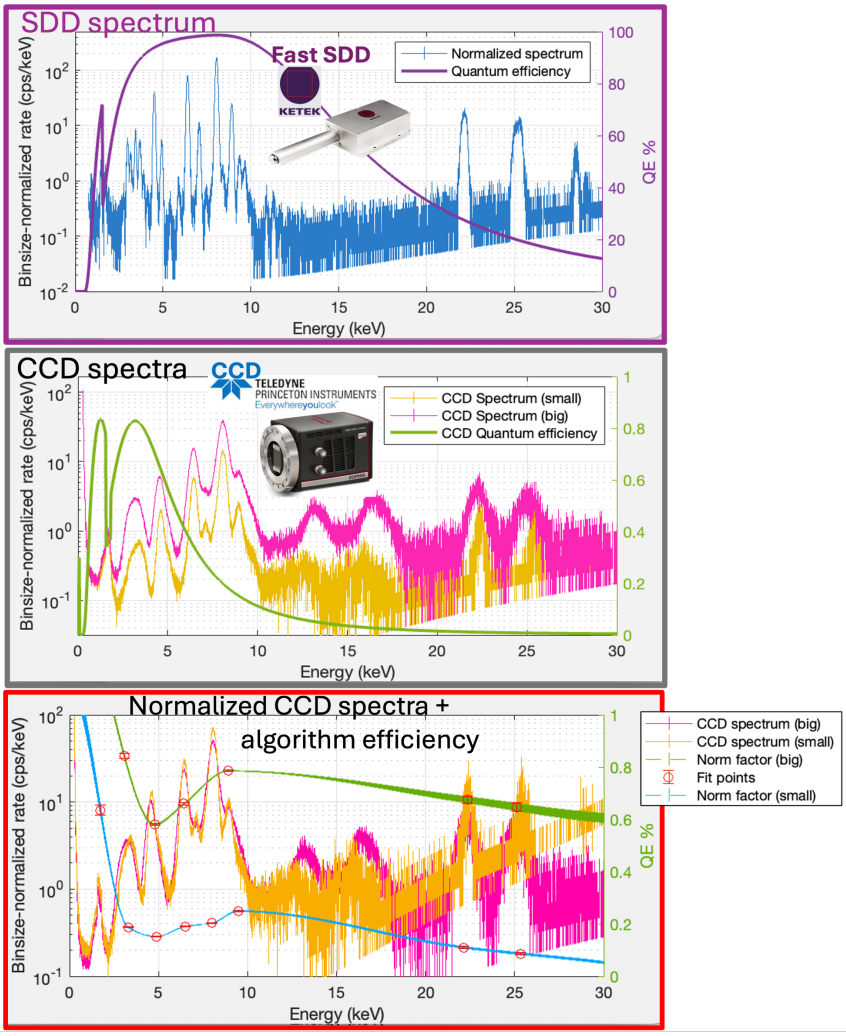


Figure 3.33: Efficiency correction applied to the multi-element target imaging measurement: SDD spectrum and QE (top) - CCD spectra in low (pink) and high (yellow) resolution modes and intrinsic QE (middle) - Efficiency-normalized CCD spectra with respective normalization factors (bottom).

### 3.5.8 HDR imaging

There is a statistical limit on the application of the aforementioned corrections: when the X-ray flux is too high, the amount of not-photon-counted data is too high respect to the single-photon one, determining a lack of information which cannot be corrected. Moreover, the correction method well works as a small approximation, since big clusters of multiple events ($N_{loc.-max.} \gtrsim 200$) deviate from the Monte Carlo simulation results.

When the dynamical range of the observed source is too high, it is not always possible to obtain good data by simply lowering the exposure time, since the collection of an acceptable amount of statistics on the lowest-intensity component of the image would require the acquisition of an excessively large number of frames, sometimes not compatible with a typical experimental time schedule.

The HDR (High Dynamical Range) acquisition method is a good option to overcome this limit, consisting of performing two or more sets of acquisitions at different exposure times.

Subsequently, a criterion of selection can be defined to unify the two acquisitions over a single HDR image.

The application of the HDR method to the energy-space-resolved data has been already developed in [46], where a criterion of image weighting was applied to combine together the low and high exposure datasets.

In light of the latests developments presented in this work, a more quantitative criterion has been defined for combining two acquisitions into a single HDR dataset, based on the cluster feature of the number of local maxima.

An image is iteratively defined during the data reduction (namely, the identification of all the cluster-events on the frames), containing all the respective regions involved in each cluster having $N_{loc.-max} > 1$, than divided by the total number of analyzed frames.

The resulting matrix is then normalized between 0 and 1, and represents the probability map of observing pile-up phenomena.

An example is shown in figure 3.34, where the pile-up weight maps are shown concerning the high-exposed (on the left) and low-exposed (on the right) acquisitions of plasma imaging, well described in the next

subsections.

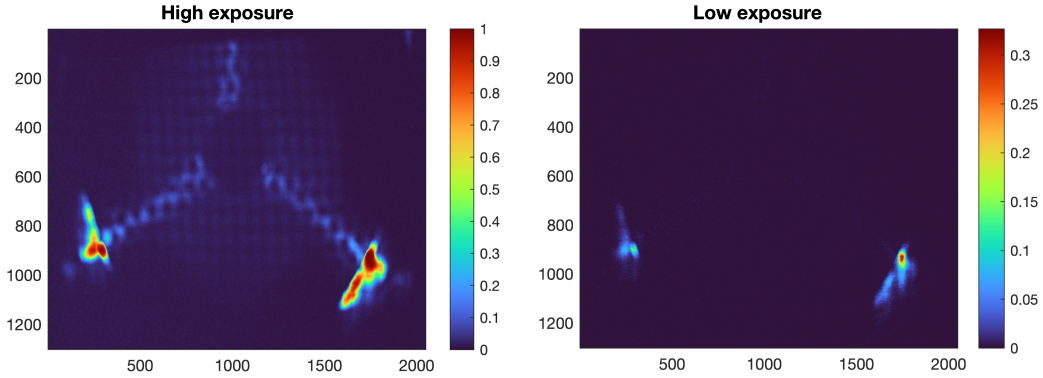


Figure 3.34: Pile-up probability maps in a plasma imaging measurement at high exposure ($t_{exp}^{high} = 162.2ms$, left) and low exposure ($t_{exp}^{low} = 18.2ms$, right)

It can be observed that the brightest regions of the left image (which will be later defined as "magnetic poles": the emission spots involved into the maximum plasma flux over the metal walls of the plasma chamber), exhibit values of pile-up probability around 100%, thus determining almost a total loss of energy-resolved information.

The corresponding high-intensity regions on the low-exposed pile-up map (figure 3.34-right) is than maximized around 34%. This means that almost the 66% of the information in these regions is energy-resolved and it can be used by applying the appropriate aforementioned corrections.

An HDR-weight map is then defined on the map of the highest exposure (figure 3.34-left), establishing empirically a threshold value equal to 0.2. Moreover, such map is normalized to the value of 0.5.

This map weights the amount of data to be combined from the low- and the high- exposed acquisitions, providing overlapping regions which contain data from both of them. In this way, the cut between the different dynamical range regions is automatically smoothed, compensating any effects produced by the low-statistics regions.

Figure 3.35 shows the respective images of photon-counted events into the high- and low- exposure acquisitions (top-left and top-right), represented in a log color scale.

It can be observed the lack of information into the magnetic poles on the high-exposure, which can be filled with the low-exposed one. On the other hand, most of the low-exposed picture lacks of information, exhibiting a low signal-to-noise ratio.

The HDR-weight map, defined as "HDR mask" in figure 3.35-bottom-right therefore weights the amount of data to be taken from the low-exposure into the final image (conversely, the complement "$1 - HDRmask$" weights the amount of data to be taken from the high-exposed image).

Figure 3.35-bottom-left shows the final HDR result.

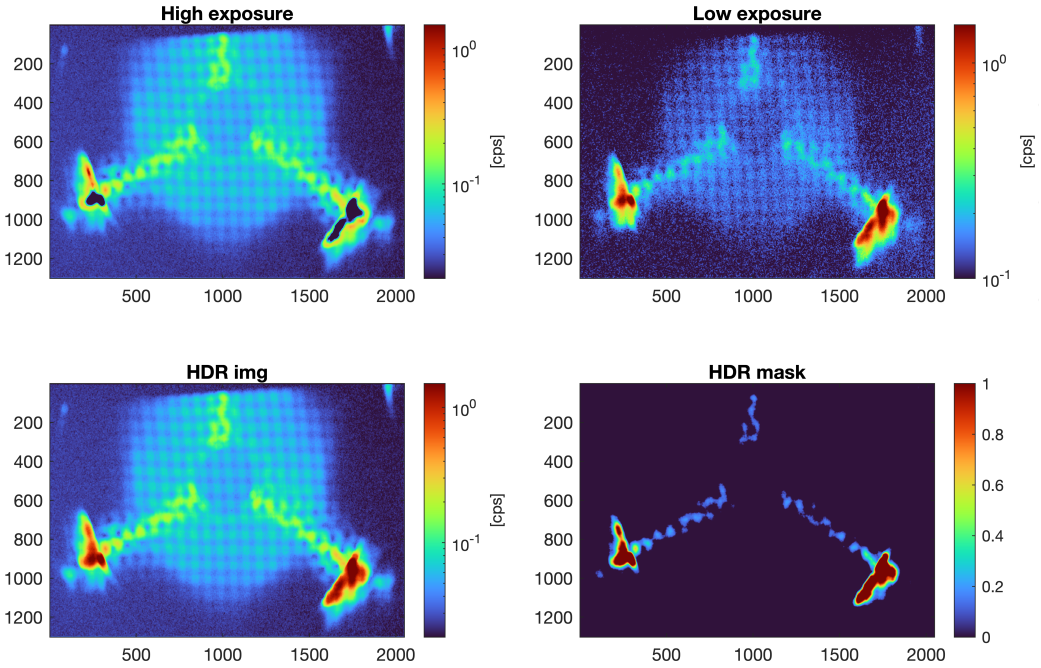


Figure 3.35: Application of the HDR-weighted imaging technique: Plasma images of SPhC events at high exposure ($t_{exp}^{high} = 162.2ms$, top-left) and low exposure ($t_{exp}^{high} = 162.2ms$, top-right) expressed in counts-per-second - HDR combination of the two dataset (bottom-left) - HDR-weight mask weighting the amount of data to be taken from the low-exposure into the final image. Its complement (1 - HDRmask) although weights the amount of data from the high-exposure to the final image (bottom-right).

The HDR combination of data is also defined preserving the energy in-

formation, by applying the HDR-weight map to all the registered events, according to each impinging position.

Therefore, the result on the full-frame spectrum is shown in figure 3.36, comparing the low- and high- exposed spectra and the HDR-combined one.

As will be explained in the respective plasma-measurements subsection (5), the balance between the two main spectral lines on the spectra (corresponding to the Ne-$K\alpha$ and Al-$K\alpha$ emission at $E_{Ne-K\alpha} = 849eV$, $E_{Al-K\alpha} = 1.49keV$), differs between these spectra.

This is due to the main presence of aluminum fluorescence emission into the high intensity regions, which are almost totally missing in the high-exposed acquisition. Conversely, being the neon fluorescence emitted from the weaker parts of the images, both the acquisitions contain the same amount of Ne fluorescence data.

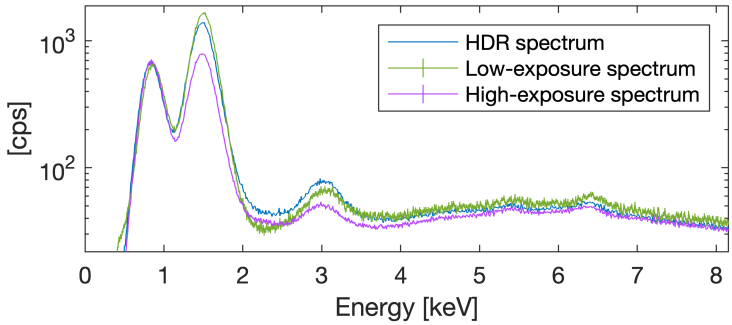


Figure 3.36: HDR result on the full-frame spectrum: low-exposure and high-exposure (green and pink), resulting HDR spectrum (blue).

The application of this method will be shown in the experimental results subsections of the next chapter (5).

Chapter 4

# Experimental setups

This chapter shows the experimental setup adopted for the application of the above-mentioned pin-hole camera technique to the ECR plasma phenomena investigation.

The pin-hole camera setup was then mounted on the Atomki ECRIS in Debrecen, Hungary, a facility specifically developed for fundamental research aims.

Several experimental configurations have been set to perform space- and time- resolved spectroscopy measurements.

## 4.1 Atomki B-minimum ECR facility

The Atomki-ECRIS is a 2nd generation ion source and the basic operation frequency is typically 14.25 GHz, produced by a Klystron.

The magnetic system is composed of two axial coils, providing the axial magnetic gradient, and a hexapolar permanent magnet providing the radial gradient, the latter being a key factor of a B-minimum plasma trap (see section 1.2.1 and figure 1.7 explaining the relevance of the hexapolar field in plasma confinement).

The axial magnetic field is 1.26 T at injection side, 0.39 T ($B_{min}$) and 0.95 T at the extraction, whilst the radial magnetic field produced by the hexapole at the plasma chamber wall (R = 29 mm) is about 1.2 T.

Figure 4.1 shows an overview of the source on the left and the typical axial magnetic configuration on the right.

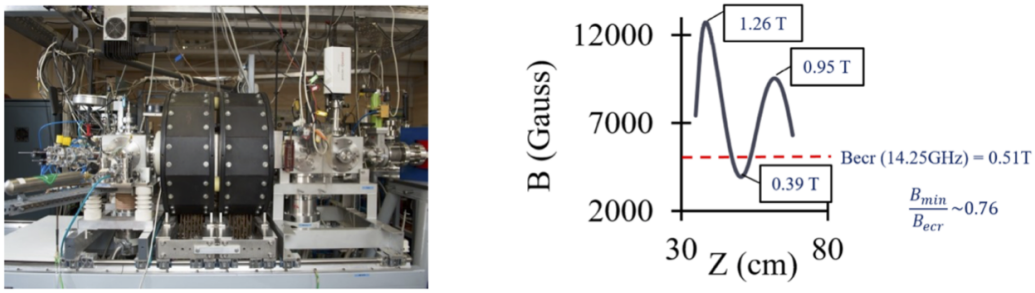


Figure 4.1: Picture of the ATOMKI ECRIS (left), typical axial magnetic field configuration with the resonant ECR value in red for a pumping frequency of 14.25 $GHz$. (right)

The ion source provides an extraction system at 10 kV and a mass spectrometer to measure the extracted charge state distribution. It is not connected to any accelerator, thus it is suitable and available for plasma physics investigations.

Figure 4.2 shows a sketch of the plasma chamber, where the confined Ar plasma is represented as an ellipsoid; the deconfinement fluxes along the magnetic branches are represented with the yellow stream lines.

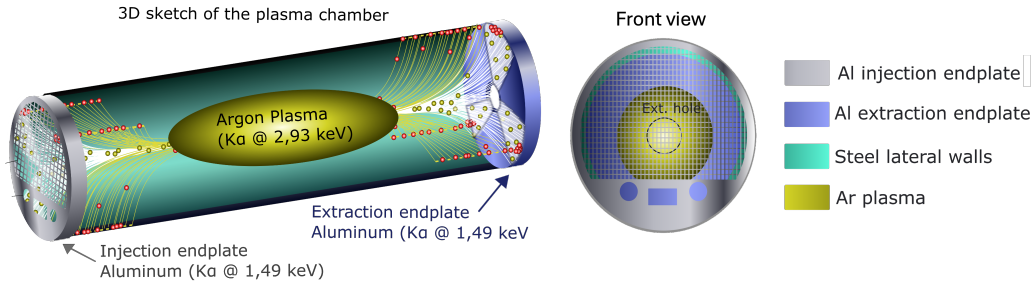


Figure 4.2: Sketch of the plasma chamber with the Al flanges at the extraction and injection sides. The Ar plasma is schematized as a yellow ellipsoid and the deconfinement fluxes with yellow stream lines. The front view is reported on the right, highlighting the view of the plasma through the injection-side mesh.

The plasma chamber is closed with an Al injection flange, providing the housing for the RF and two gas injection lines, and a $400\mu m$ mesh allowing both the electromagnetic enclosure and the X-ray line of view. The extraction plate at the opposite side, is an Al flange with an extraction hole and a thicker mesh to enhance the vacuum pumping.

The B-minimum magnetic configuration determines a plasma confinement morphology, typical of this kind of ion sources, composed by a closed egg-shaped ECR resonant surface and a hexapolar streamline, which determines the shape of the so-called "magnetic branches".

The plasma is then confined into the volume enclosed by the ECR surface and deconfined along the streamlines, impinging on the circular endplates of the plasma chamber and generating two complementary tricuspidal prints on them.

Figure 4.3 shows the scheme of the magnetic field lines, drawn in red at the extraction side ($z > 0$) and in blue injection side ($z < 0$).

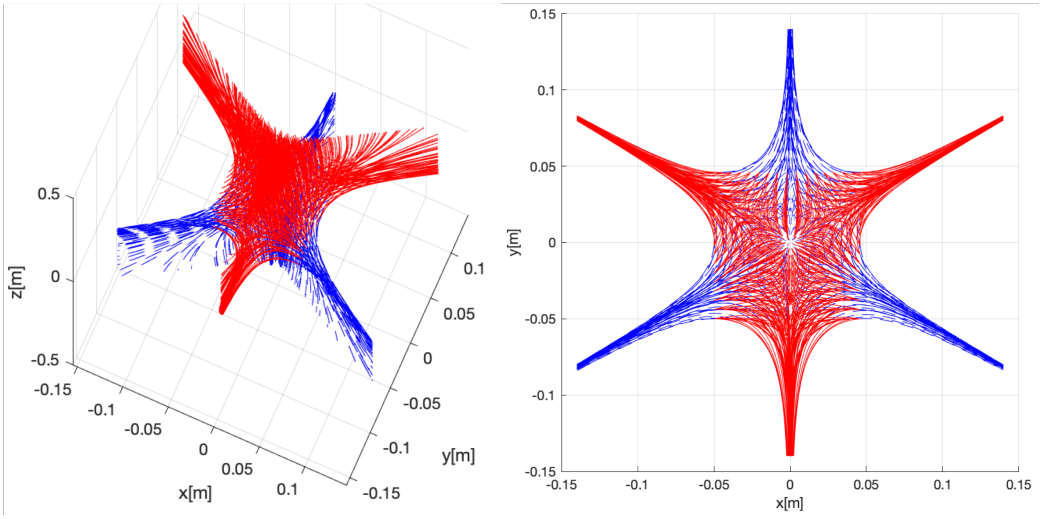


Figure 4.3: Scheme of the magnetic field lines into the Atomki ECRIS, reporting in red the lines towards the extraction side (z>0) and in blue the lines towards the injection side (z<0) into two different view projections. The image on the right (XY projection) reflects the confinement structure of the plasma observed in the imaging measurements.

The axial component of the magnetic field is typically asymmetric be-

tween injection and extraction side, in order to enhance the process of ion-current extraction.

### 4.1.1 Pin-hole camera setup for time-space-energy-resolved measurements

The pin-hole camera diagnostic (section 3.3) was coupled to the plasma chamber at the ignition side through a vacuum line, containing an electric insulator element and a gate-valve, with a magnification M=0.55 at the ignition side and M=0.44 at the extraction side (M=0.495 at the mid-plane).

The sketch of the overall setup with the pin-hole camera is reported in figure 4.4.

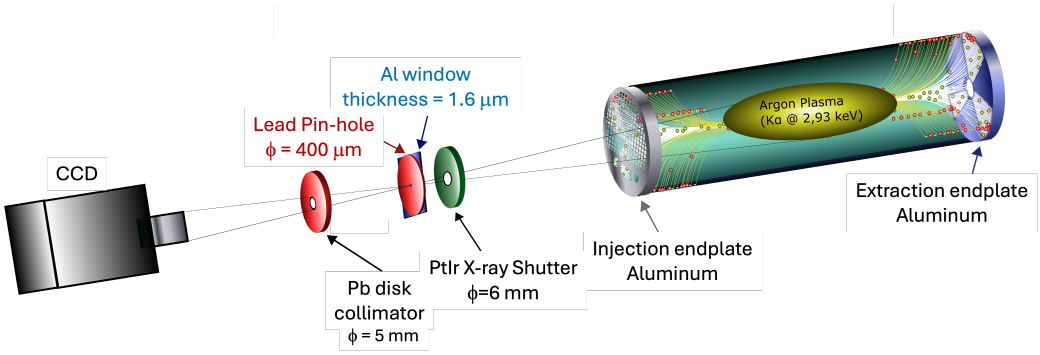


Figure 4.4: Sketch of the experimental setup. From the left: CCD camera, pinhole multi-collimator system, shutter, plasma chamber.

Figure 4.5 shows a fluorescence-filtered view of the plasma in Ar, Ti and Ta fluorescence lines, obtained on a previous measurement on the same facility [66], overlapped with the scheme of the magnetic branches.

This image is useful to explain the structure of the plasma, composed of the following parts:

- **Plasmoid**: the confined component enclosed into the ellipsoidal ECR heating surface;
- **Magnetic branches**: the deconfined component (namely plasma loss) generating the well-observable tri-cuspidal shape, correspond-

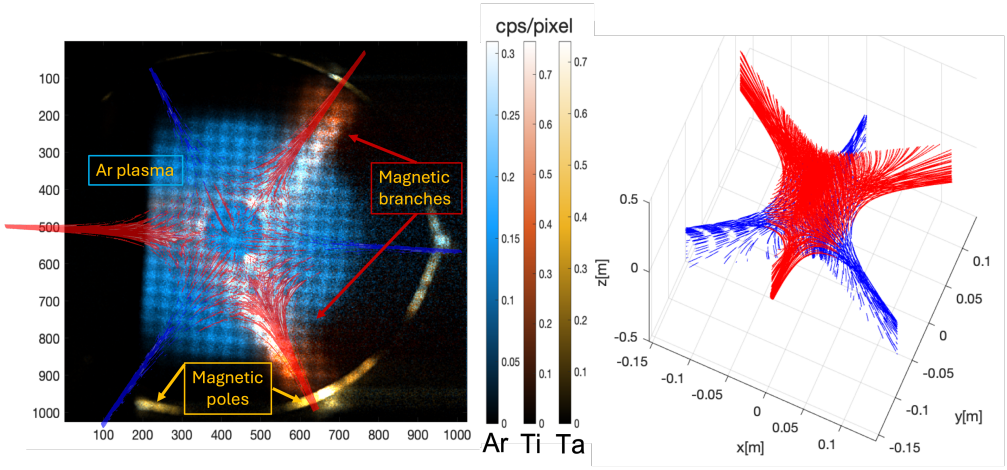


Figure 4.5: Fluorescence-filtered view of the plasma in Ar,Ti and Ta fluorescence lines [67], overlapped with the scheme of the magnetic branches. This figure is useful to explain the structure of the images acquired in the present experimental conditions.

ing to the intersection of the loss streamlines with the metallic walls of the chamber;

- **Magnetic poles**: the most external deconfinement spots against the cylindrical walls of the chamber.

For an easier reading of the image, the three-dimensional simulation projection has been repeated from figure 4.3.

It can be noticed that only the three magnetic branches at the extraction side (in red) can be observed, since the other three (in blue) are due to the streamlines directed through the injection endplate, indeed all the six poles are visible in the image, being the solid external walls involved.

The slight mismatch between the injection magnetic poles and the simulated streamlines (in blue) are due to a not perfect alignment between the two parts of the permanent hexapolar magnet of the ECRIS, which is not considered in the magnetic simulation.

Figure 4.6 shows the pin-hole camera setup (a) on the plasma chamber, highlighting the main components. At the bottom, the injection (c) and extraction (d) flanges are shown.

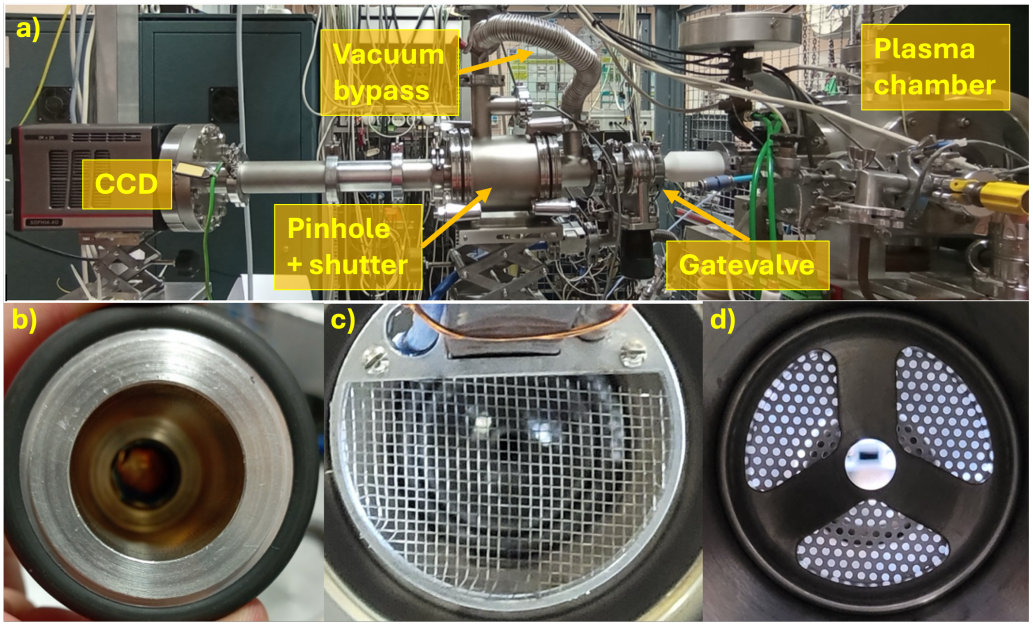


Figure 4.6: Pin-hole camera setup mounted on the Atomki ECRIS in the final experimental configuration. The overall view is shown on the top (a) and the details of the Al thin window (b), the injection mesh (c) and the extraction plate (d) are shown at the bottom.

A thin aluminum window (800$nm$ thick) was placed in a KF O-ring holder (figure 4.6-b) to obtain a differential vacuum pumping through a bypass, being the diagnostic line not equipped with flanges for high vacuum. In fact, the highest vacuum reachable by the pin-hole camera line ($\sim 10^{-5} mbar$) was not suitable with the base vacuum required for the plasma ignition ($\sim 7 \cdot 10^{-7} mbar$).

The pin-hole vacuum line was equipped with a system of valves and bypass lines (figure 4.6-a) to protect the window during the separate pumping of all the volumes from ambient pressure to middle-high vacuum ($\sim 10^{-3} mbar$). Below this pressure the gate-valve was opened, and the differential vacuum was kept beside the Al window with a rotative

pump on the CCD side ($p_{CCD} = 3 \cdot 10^{-3} mbar$) and a turbomolecular pump on the plasma side ($p_{plasma} = 7.4 \cdot 10^{-7} mbar$).

The Al window was strong enough to keep the differential vacuum and thin enough to be transparent in the low energy X-ray domain (0.5-30 keV). Two further layers of $800nm$ were also placed into the pinhole holder (figure 4.6-b) to attenuate the high intensity of plasma emission at very low energy, reaching the overall Al screening thickness of $2.4\mu m$.

Figure 4.7 shows the X-ray transparency of the set of windows at very low energy.

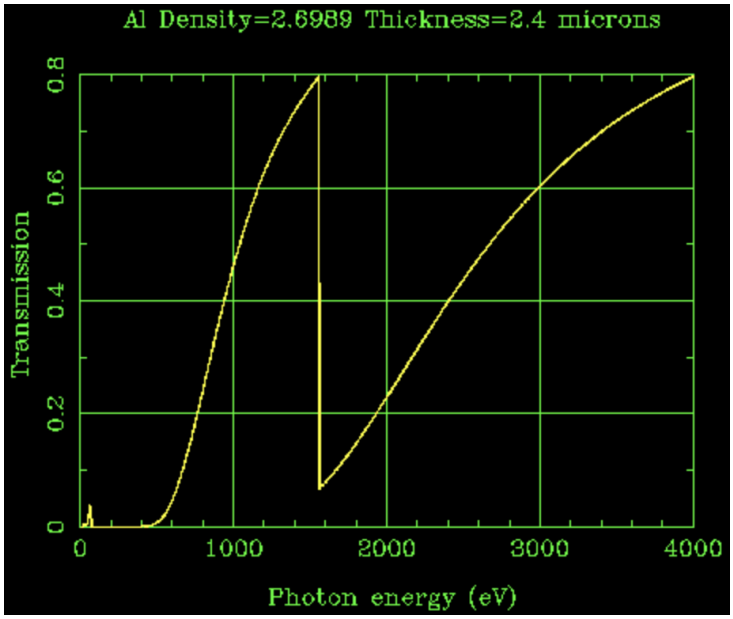


Figure 4.7: Overall transparency vs X-ray energy of the set of Al windows, with a total thickness of $2.4\mu m$ [https://henke.lbl.gov/].

**Gas injection system** The plasma chamber provides the simultaneous injection of two different gases, by two high-pecision valves remotely controlled. Ne, Kr, Ar, Xe gases were provided for the present measurements, in order to investigate on the gas mixing physics.

**CCD acquisition trigger** Two different trigger systems have been used during the present measurements, depending on the required type of acquisition.

Time-integrated measurements have been performed by self-triggering the X-ray shutter with the CCD camera output signal, sending the open-pulse from the CCD to the shutter driver with a fixed exposure time.

Time-resolved measurements have been performed by using a signal generator as a master trigger and a multiple TTL signal generator to provide two delayed triggers respectively to the CCD and shutter. In this way, the shutter-open was triggered few ms before the CCD, compensating the mechanical opening transient of the shutter and enhancing the time resolution.

Figure 4.8 summarizes the two trigger configurations, showing the time-integrated gas-mixing configuration on the left and the master-triggered configuration on the right, for the time-resolved acquisitions.

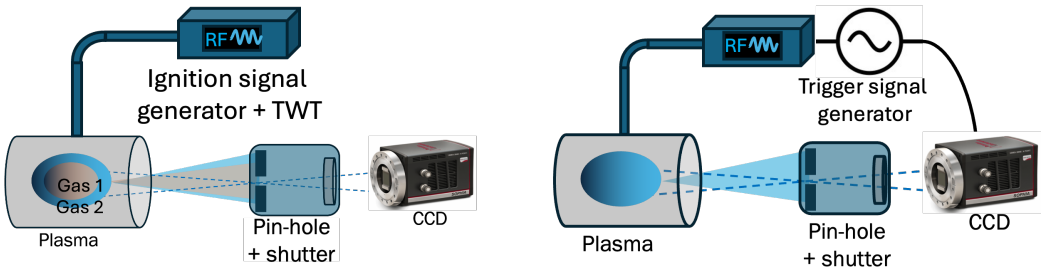


Figure 4.8: Trigger configuration of the two experimental conditions: self-triggered CCD acquisition scheme for time-integrated measurements (left) - mater-triggered CCD acquisition scheme for time-resolved measurements on pulsed plasma (right).

In the time-resolved configuration, the periodic master trigger was directly sent to the klystron, to obtain a pulsed plasma ignition, while the CCD and shutter were controlled by two respective TTL pulses, synchronized case by case with the time window of interest, taking into account the needed exposure time and the opening transient of the shutter.

The overall period of the master trigger period was always set longer than the total CCD readout time, to ensure that the CCD was in a ready state before each subsequent exposure.

Figure 4.9 shows a scheme of the trigger logic in one of the experimental configurations: the red line exemplifies the expected dynamics of the observed phenomenon (namely, the afterglow peak of plasma); the master trigger generates the RF pulse with 1$s$ period and 0.5$s$ width; the 5$ms$ exposure time window is delayed subsequently in the range $500 - 525ms$ from the master trigger, in this case, to focus on several temporal phases of the plasma decay transient.

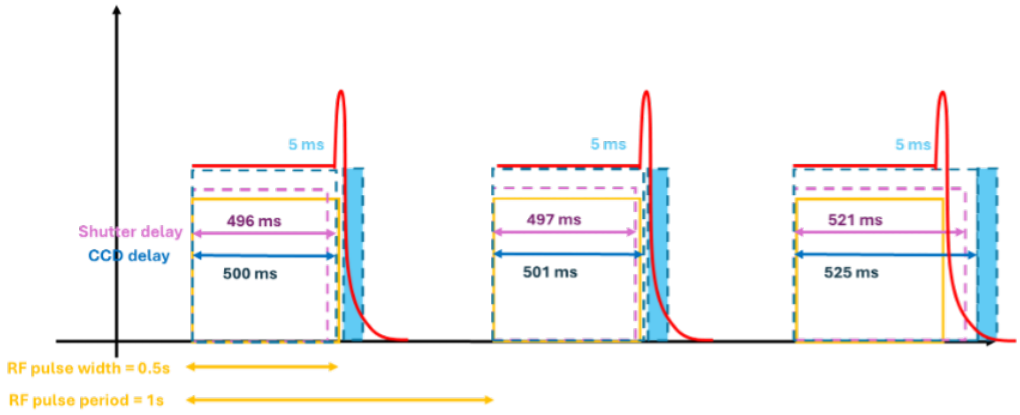


Figure 4.9: Scheme of the trigger logic in a time-resolved configuration: the red line represents the expected observable dynamics; the master trigger generates the RF pulse with 1s period and 0.5s width (yellow); the 5ms exposure time window (blue) is delayed subsequently in the range 500 - 525ms from the master trigger, in this case, to focus on several temporal phases of the plasma decay transient.

The exposure window is opened by triggering the CCD acquisition in the "Clean Until Trigger" state, which provides a continuous exposure and cleaning of collected charge until receiving a trigger pulse. This determines a response latency of the order of one vertical shift time, from $1 - 30\mu s$.

The shutter pulse (in pink) is delayed 496$ms$, 4$ms$ less than the CCD trigger on, to exclude the mechanical opening transient.

The exposure finishes with the close pulse to the shutter, at which time the CCD is triggered to the readout process.

The application of this setup will be shown in the next chapter.

Chapter 5

# Space and time resolved characterization of ECR plasma dynamics

The experimental campaign at the ECR Atomki lab in Debrecen was devoted at investigating the ECR plasma dynamics under conditions of a wide and interdisciplinary interest, spanning from operations of ECR plasma systems such as ion sources, to plasmas for thermonuclear fusion and fundamental research. About this latter topic, most of the expected outcomes are relevant for the PANDORA project [20, 21].

The X-ray pin-hole camera diagnostics is an insightful technique to characterize the plasma morphology and to perform space resolved spectroscopy (thus evidencing the local displacement of electrons at different energies, as well as of plasma ions highlighted by fluorescence lines emission) versus the main tuning parameters such as the pumping wave frequency and the strength of the confining magnetic field. It is very useful to investigate the dynamics of plasma versus plasma losses and, consequently, to study how the operative parameters (RF pumping frequency and power, magnetic field and the presence of plasma turbulence) affect the plasma confinement, stability and turbulence onset.

In addition, the timing capability of the X-ray shutter allows to investigate the time evolution of plasma transients such as switch on/off and

plasma behavior under turbulent regimes.

Several kinds of measurement have been proposed, mostly motivated by the capabilities of the newly developed energy-space-time resolved diagnostic tool, with respect of the literature's state of the art about relevant research fields on ECR plasma physics:

- Time-integrated measurements have been performed to investigate the plasma structure under different conditions of gas mixing by the technique of the x-ray fluorescence filtered imaging.
- Time-resolved measurements have been performed to investigate the plasma switch-off transient by observing the time evolution of such phenomena on different time windows.

The present chapter is divided into four sections, presenting each kind of measurement with a brief introduction and three respective subsections with the experimental configuration, results and discussion.

The first three sections concern the space and time-resolved measurements performed during an experimental campaign in November 2024. The last section is devoted to the study of the thermodynamic parameters of plasma by the application of the emissivity model on the space-resolved spectroscopic information. This work, applied to a dataset of a previous experimental campaign on the same ECR facility (March-June 2018), has been published on Physics of Plasma journal [67] as the first-time application of the technique in a space-resolved investigation.

## 5.1 Gas mixing dynamics investigation

These measurements are devoted at investigating the dynamics of gas mixing confinement, observed in several configurations. The lack of experimental observation in literature on the related phenomena (see section 2.5.1) makes this kind of measurement particularly relevant.

The application of the fluorescence-filtering technique and the respective imaging analysis make possible to reveal relevant features about plasma structure, giving access to a selective information about the emissivity map of each single gas species in gas-mixed plasmas.

Being the observation of the gas mixing effect more significative when mixing gases with a considerable mass ratio ($\sim 3-4$), couples of gases have been chosen according both to their masses and their respective fluorescence lines emission, which have to fit into the detection efficiency of the CCD diagnostic.

### 5.1.1 Experimental configuration

Two gas mixing configurations have been studied: Ne+Kr and Ar+Xe, with the aim of probing the gas mixing effects in different conditions.

The choice of Kr gas is motivated by the similarity to other available measurements in literature [58, 71]. Moreover, the use of noble gases (He, Ne, Ar, Kr, Xe, Rn) is preferable due to their neutrality in terms of chemical interactions between the mixed species and with the plasma chamber metals, as well as not having molecular states.

Although oxygen and nitrogen gases are commonly used to observe gas mixing effects, their K fluorescence lines (524.9 - 392.4 eV) are out of the sensitivity range of the detector, therefore the Ne+Kr mixing was chosen as the optimal trade-off to satisfy all the chemical, spectroscopic and mass requirements.

Furthermore, the choice of Ar+Xe mixing is then motivated by the optimal fit of fluorescence lines (K and L respectively) into the CCD efficiency range, as well as investigating a less common physics case with a mass ratio ($M_{Xe}/M_{Ar} = 3.3$) similar to the Ne+Kr case ($M_{Kr}/M_{Ne} = 4.1$). Moreover, the application of fluorescence-filtered imaging to heavy elements could have a significant scientific impact (higher charge states can be explored, allowing the investigation of line emission broadening effects).

Table 5.1 summarizes the features of all the above-mentioned elements, in terms of mass, main detectable fluorescence lines and respective detection efficiency.

| Element | Atomic mass | Fluorescence line | Energy [keV] | Intrinsic CCD efficiency |
|---|---|---|---|---|
| 10 Ne | 20.2 | $K\alpha$ | 848.6 | 30.0% |
| 18 Ar | 39.9 | $K\alpha$ | 2.96 | 58.3% |
| 36 Kr | 83.8 | $K\alpha$ | 12.65 | 5.75% |
| 54 Xe | 131.3 | $L\alpha$ | 4.11 | 63.6% |

Table 5.1: Relevant properties of the mixed gas species.

The Ne+Kr measurement was structured in two steps: a first characterization of the space-integrated X-ray emission was performed by the SDD X-ray detector at different mixing balances of the two gases (reported in table 5.2), varying the Ne valve opening with a fixed set of the Kr valve.

| Config. ID | Pressure [mbar] | RF net power [W] | $B_{max}/B_{min}$ | Ne/Kr mixing % | Number of frames | Exposure time [ms] |
|---|---|---|---|---|---|---|
| 1 | $1.4 \cdot 10^{-6}$ | 201.2 | 2.29 | 0 | 2000 | 162.2 |
| " | " | " | " | " | 1000 | 18.2 |
| 2 | $1.8 \cdot 10^{-6}$ | 204.7 | " | 100.0 | - | |
| 3 | $0.3 \cdot 10^{-6}$ | 205.1 | " | 106.7 | - | |
| 4 | $0.2 \cdot 10^{-6}$ | 201.3 | " | 105.0 | - | |
| 5 | $1.7 \cdot 10^{-6}$ | 205.3 | " | 102.2 | - | |
| 6 | $2.3 \cdot 10^{-6}$ | 207.4 | " | 110.1 | - | |
| 7 | $2.6 \cdot 10^{-6}$ | 206.4 | " | 112.3 | - | |
| 8 | $2.1 \cdot 10^{-6}$ | 205.0 | " | 105.8 | 2000 | 162.2 |
| " | " | " | " | " | 1000 | 18.2 |

Table 5.2: Set of measurements in different gas mixing configurations.

The charge state distribution (CSD) of the extracted Kr ion current was monitored on each configuration, making possible an optimization tuning, whose result is shown in figure 5.1.

On the second step, the optimal mixing configuration maximizing the $Kr^{11+}$ ion current extraction was chosen for the CCD imaging measurements. Two sets of 2000 high-exposed frames ($t_{exp}^{high} = 162.2ms$) plus 1000 low-exposed frames ($t_{exp}^{low} = 18.2ms$) have been acquired both on the optimized Ne+Kr mixing (config. 8) and on the pure Kr plasma (config. 1).

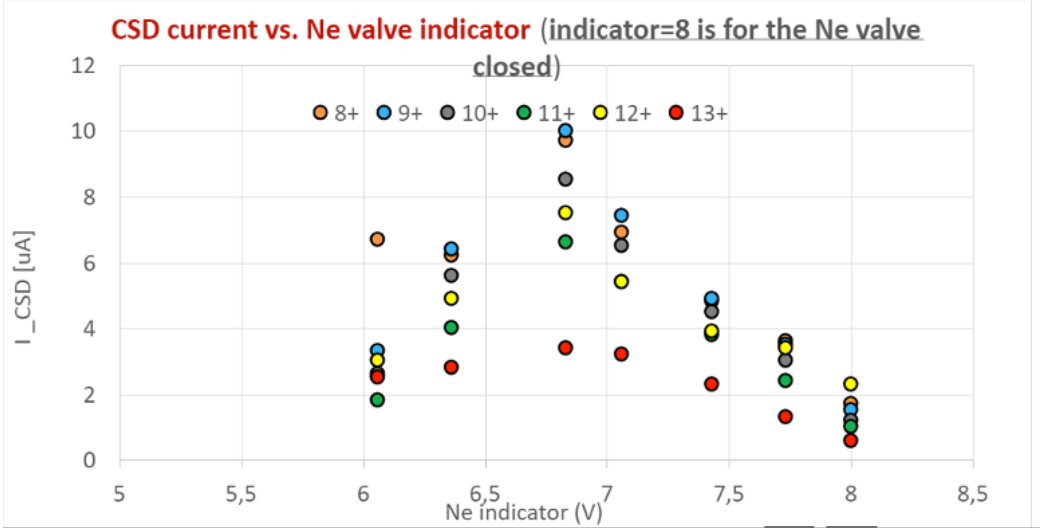


Figure 5.1: Charge state distribution of Ar 8+ to 11+ in all the explored mixing configurations, to optimize the gas-mixing for high charge state extraction.

The Ar+Xe CCD measurement was similarly done by exploring the configurations of table 5.3, having optimized the gas mixing on the Xe ion current extraction. No SDD spectra were acquired for these configurations.

| Config. ID | Pressure [mbar] | RF net power [W] | $B_{min}/B_{ECR}$ | Ar/Xe mixing % | Number of frames | Exposure time [ms] |
|---|---|---|---|---|---|---|
| 1 | $2.4 \cdot 10^{-6}$ | 201.2 | 0.77 | 0 | 1500 | 102.3 |
| 2 | $2.4 \cdot 10^{-6}$ | 240 | 0.77 | 94.61 | 1500 | 52.1 |

Table 5.3: Gas mixing configurations of Ar + Xe imaging measurements.

All the reported exposure times are corrected by the effective opening time of the shutter (see section 3.5.6).

A fluorescence-resolved image, referring to the Ne+Kr configuration, is shown in figure 5.2 to give a brief description of the observable plasma structure.

The pseudo-colors figure is the overlap between two images, respectively obtained by filtering the $K\alpha$ fluorescence of Ne ($0.85keV$) in green

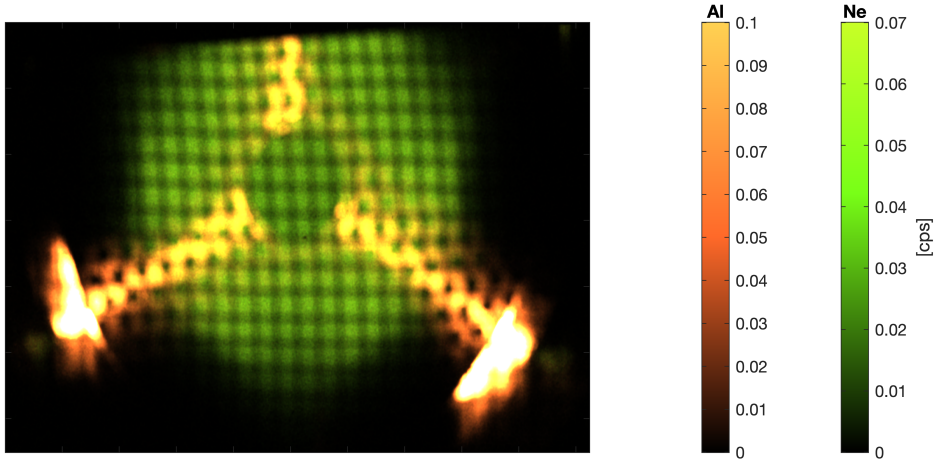


Figure 5.2: Fluorescence-resolved image of Al and Ne obtained in the Ne+Kr configuration. The color bars of the two respective elements are reported on the right

and the $K\alpha$ fluorescence of Al ($1.49keV$) in yellow/orange. The green image is a projection of the plasmoid shape, defined by the ellipsoidal ECR heating surface (see section 4.2). The squared shadow pattern of the injection mesh is clearly visible, being the latter interposed through the line of sight. The yellow/orange image origins from the deconfined electron fluxes over the Al endplate, showing the latter's structure with the circular mesh pattern and the extraction hole in the center (see figures 4.4,4.5). The shape of such deconfinement print is mainly determined by the external hexapolar magnetic field at the endplate intersection, which generates the so-defined "magnetic branches", namely the three radial bands on each endplate, and "magnetic poles", namely the brightest structure at the end of each branch. Only the extraction-side branches and poles are visible in the images, since the complementary tri-cuspidal structure could be in principle observed over the injection endplate by placing an X-ray diagnostic on the opposite side.

The color scale saturates at the pole emission, since the dynamics of the deconfinement image is too wide to be represented in a unique linear color scale.

Such description of the plasma structure will be usefully recalled on

the next paragraphs.

### 5.1.2 Results

**CCD data analysis** All the acquired CCD data have been analyzed by the algorithm described in section (3.5), to obtain the energy-space resolved information from SPhC acquisitions. The following information have been extracted from each dataset:

- Full image, integrated above time and energy
- Energy spectra integrated above time and space
- Fluorescence-filtered images, energy-integrated above the main fluorescence peaks of interest for plasma structure identification.

Four sets of acquisitions have been performed in this measurement (as shown in table 5.2 and 5.3), investigating the single-gas (the heaviest species) vs mixed-gas of the two couples: Ne+Kr, Ar+Xe.

The energy-space resolved information extracted from each dataset allows the imaging reconstruction of each chemical species, making the distinction possible between the confined gas distributions and the electrons deconfinement over the Al endplate.

Figure 5.3 shows the full-frame energy spectra, reporting the Kr-only and Ne+Kr emission (on the top) and the respective Xe-only and Ar+Xe emission (on the bottom). The main fluorescence lines are reported on the spectra.

For an easier reading, figure 5.4 reports all the fluorescence lines (expressed in keV) of interest for the present study.

The spectra contain all the X-ray fluorescence line emission pattern from both the plasma chamber (Al, Fe, Cr K-lines) and the gas species (Ne, Kr K-lines on the top, Ar K-line, Xe L-line on the bottom), well distinguishing the absence of the lighter gas component (Ne, Ar respectively) in the single-gas configurations (blue lines).

The L-lines of krypton are not resolved from the K-line of aluminum, therefore it is not possible to obtain fluorescence-filtered imaging from these lines.

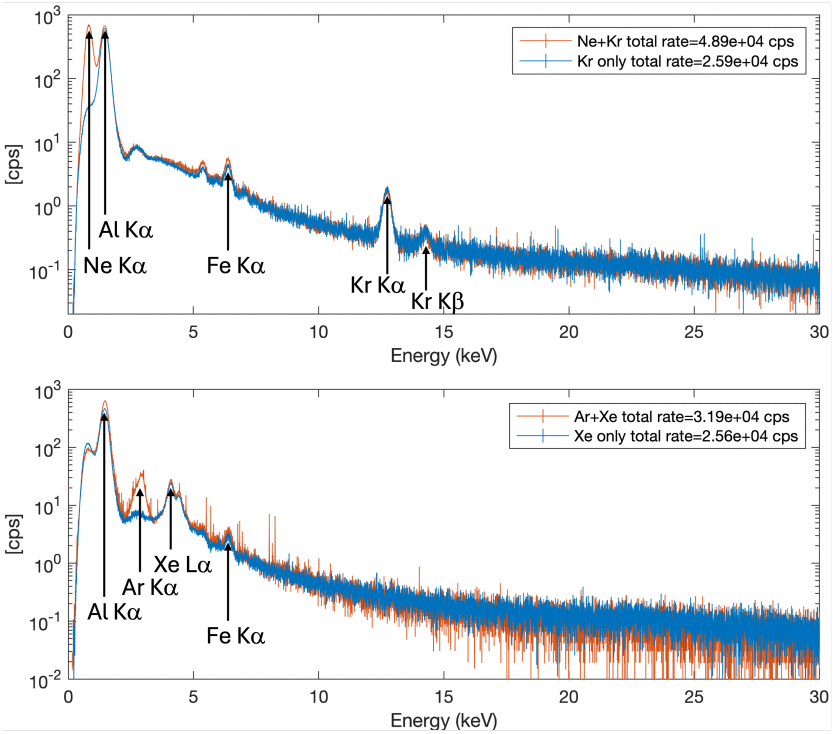


Figure 5.3: Full-frame energy spectra in the high-resolution analysis mode: Kr-only and Ne+Kr emission (top) - Xe-only and Ar+Xe emission (bottom)

| No. | Element | Ka1 | Ka2 | Kb1 | La1 | La2 | Lb1 |
|---|---|---|---|---|---|---|---|
| 10 | Ne | 0.8486 | 0.8486 | | | | |
| 13 | Al | 1.48670 | 1.48627 | 1.55745 | | | |
| 18 | Ar | 2.95770 | 2.95563 | 3.1905 | | | |
| 24 | Cr | 5.41472 | 5.405509 | 5.94671 | 0.5728 | 0.5728 | 0.5828 |
| 26 | Fe | 6.40384 | 6.39084 | 7.05798 | 0.7050 | 0.7050 | 0.7185 |
| 36 | Kr | 12.649 | 12.598 | 14.112 | 1.5860 | 1.5860 | 1.6366 |
| 54 | Xe | 29.779 | 29.458 | 33.624 | 4.1099 | - | - |

Figure 5.4: Table of the emission lines of the elements involved in this study [72]. The detectable lines are highlighted in yellow. The L-lines of Kr have been excluded because they are not resolvable neither in energy nor spatially.

The imaging analysis is performed by selecting the main fluorescence

emission from each significative element, obtaining a selective map of the electron deconfinement over the endplate (Al K-line) and of each gas species confinement.

**Ne+Kr imaging analysis** Figure 5.5 shows the pseudo colors convoluted HDR image of the Ne+Kr gas-mixed configuration on the top (filtered in the Ne, Kr and Al line emission and properly balanced to fit the dynamics into each color scale), and each single element component on the bottom. The image of Kr has been re-binned of $10 \times 10$ pixels due to low statistics.

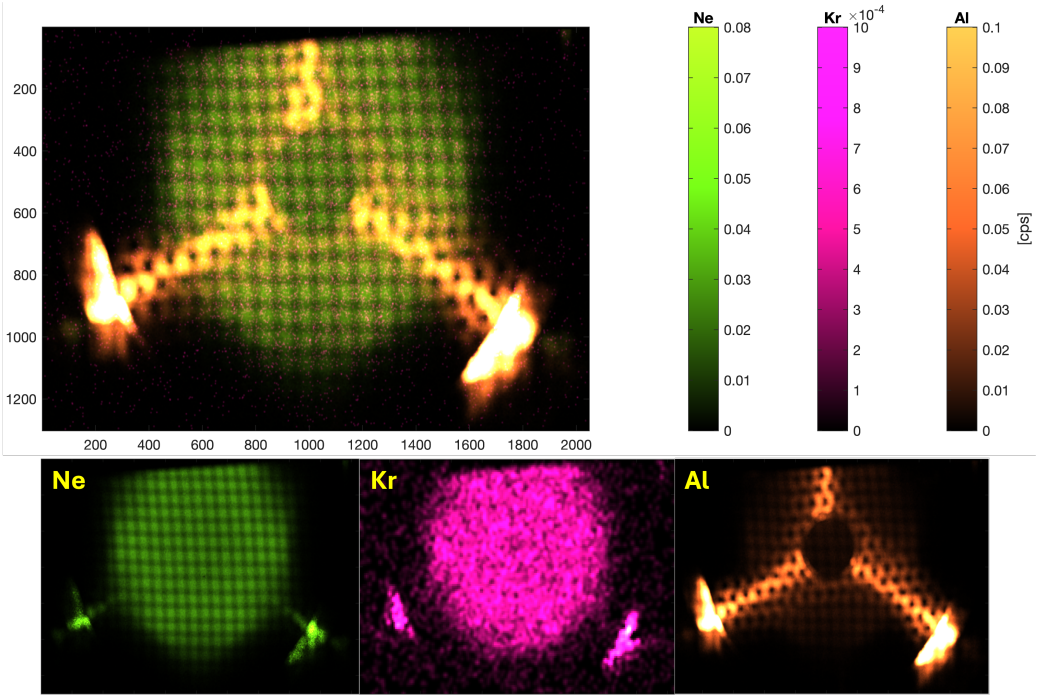


Figure 5.5: Pseudo-colors convoluted HDR image of the Ne+Kr gas-mixed configuration filtered in the Ne, Kr and Al fluorescence lines with respective color bars (top) - The single components are reported at the bottom. The Kr image has been re-binned due to the few statistics.

A quantitative analysis is proposed on these pictures to bring out significative information about the morphology of plasma.

Two rectangular ROIs are defined on the image to compare the Ne and Kr emission profiles over the x-axis. ROI 1 includes almost all the plasmoid image, avoiding the pole emission regions; ROI 2 includes the central region of the plasmoid, out of the magnetic branches regions. Figure 5.6 shows the definition of ROI 1 and ROI 2 on the left and the respective profiles of Ne and Kr on the right, respectively in green and pink lines. A smooth function has been applied on both profiles to interpolate the intensity modulation given by the shadow of the squared mesh pattern on the images.

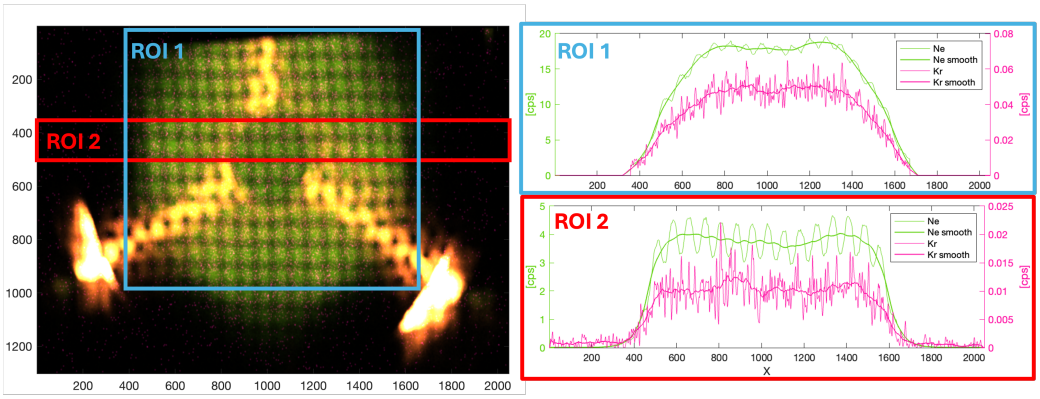


Figure 5.6: Definition of ROI 1 and ROI 2 on the image (left) and respective x-axis projection profiles of Ne and Kr in green and pink respectively (right).

The projection of Ne emission on these ROIs shows an inhomogeneous morphology, being the plasmoid characterized by a "hollow" structure, slightly depleted in the central region.

An azimuthal ROI is defined on a circular crown around the symmetry axis of the plasma chamber, projected over the theta angle (figure 5.7). The Ne K-line emission profile is shown in green on the right.

The analysis of such projections gives an idea of the plasma morphology, being the latter uniformly distributed around the symmetry axis, except for the magnetic branches where plasma is deconfined. The magnetic branches regions, respectively peaked at 90°, 205° and 330°, also contain the bremsstrahlung contribution of deconfined electrons into the same energy range of the Ne fluorescence, thus the two contributions can

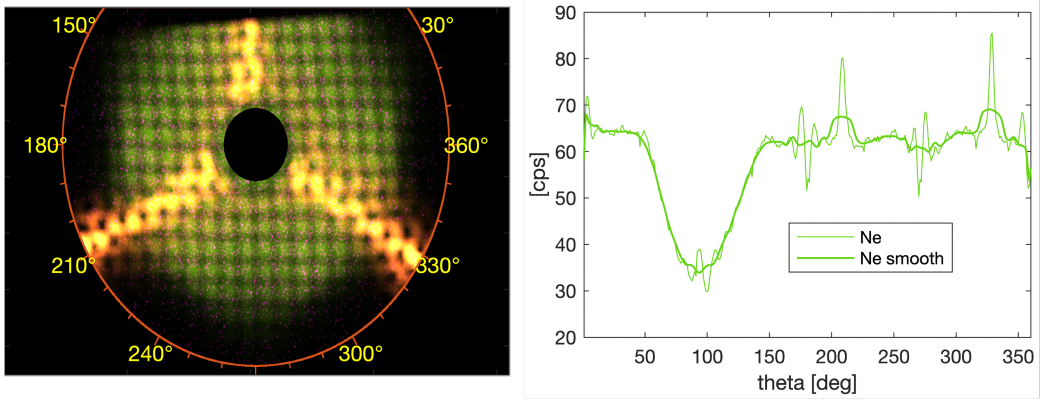


Figure 5.7: Azimuthal projection of the Ne emission (right) above the circular-crown ROI (left). The definition of the theta angle is reported as a goniometer on the image.

be hardly deconvolved. The gap between 50° and 150° is trivially due to the shadow of the solid part of the injection flange on the top of the image (see figure 4.6).

The same analysis is proposed comparing the Kr gas emission (figure 5.8), in the single gas vs. Ne-mixed configurations.

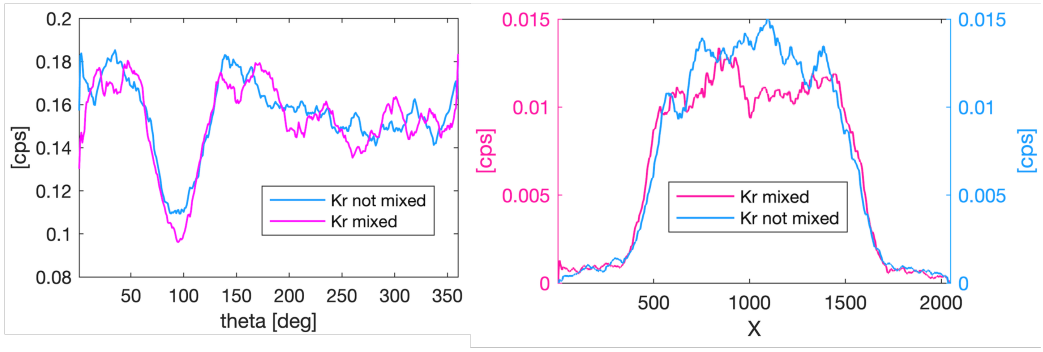


Figure 5.8: Kr emission in mixed (pink) and not-mixed (blue) cases in azimuthal projection on the circular crown (figure 5.7-left) and in x-projection on ROI 2 (figure 5.6-right).

Slight differences in the plasma morphology are shown in this comparison, concerning both the radial and azimuthal projections. The plasma

"hollowness" slightly increases in the mixed case respect to the single gas configuration. On the other hand, the azimuthal projection shows local maxima at 170°, 235°, 300°, 335° in the gas-mixed case, corresponding with the regions out from both the tri-cuspidal plasma loss streamlines (see figure 4.5).

**Ar+Xe imaging analysis** Figure 5.9 shows the pseudo colors convoluted image of the Ar+Xe gas-mixed (filtered in Ar, Xe and Al line emission) and each single element component on the bottom. Analogous results are shown in these configurations, where the signal-to-noise ratio is much better than the Kr case.

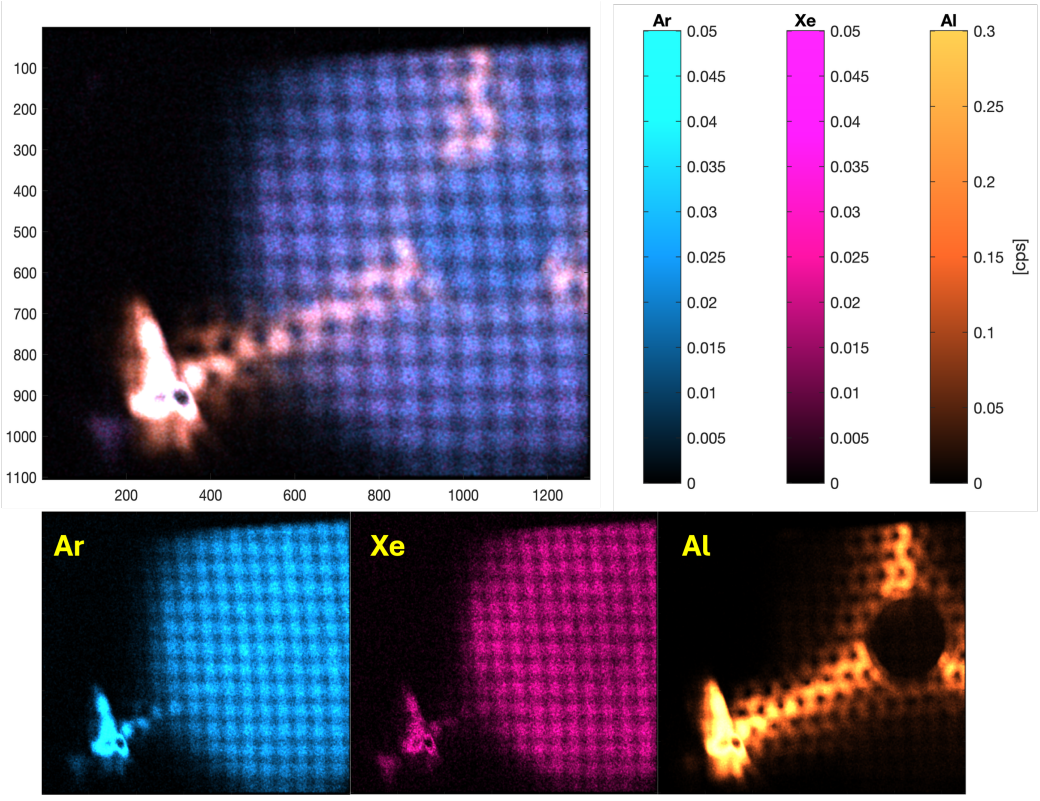


Figure 5.9: Pseudo-colors convoluted image of the Ar+Xe gas-mixed configuration filtered in the Ar, Xe and Al fluorescence lines with respective color bars (top) - The single components are reported at the bottom.

The single images of Xe and Al are compared in figure 5.10, where a gaussian filter of $\sigma = 25 pixels$ has been applied to smooth and lower the spatial resolution to reduce the squared mesh modulation effects and emphasize the features of plasma morphology.

All the images color scales have been normalized to the maximum value of the relevant portion of the image, in other words excluding the pole region, which is not fully single-photon-counted and no HDR have been acquired in this case.

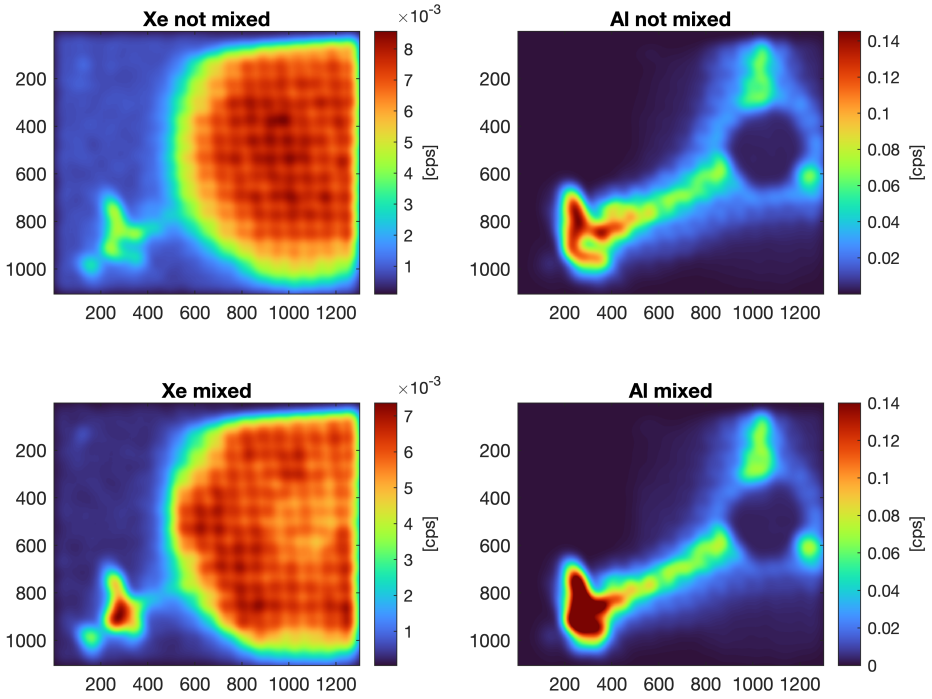


Figure 5.10: Single images of Xe and Al in the mixes (bottom) and not-mixed (top) cases. A gaussian filter of $\sigma = 25 pixels$ has been applied to smooth and lower the spatial resolution to reduce the squared mesh modulation effects and emphasize the features of plasma morphology. The multi-color scale bar helps to highlight the image differences.

The structure of the magnetic branches appears slightly different in

the two cases, indeed the structure of the plasmoid shows relevant morphological differences.

A clearer evidence of plasma hollowness is observed in the mixed case. In addition, the emission intensity reaches its maximum on the so-defined "magnetic gaps", namely, the regions in between the two tricuspidal series of magnetic branches (extraction and injection), as illustrated in figure 4.3.

A quantitative comparison is then proposed in the following figures, showing axial and azimuthal projections of the emission intensity. The evidence of plasma hollowness is observed in the x-projection profile of the central ROI (figure 5.11-bottom-right), reporting the profile of both mixed and not mixed cases (respectively in pink and blue), normalized on the region corresponding to the extraction hole ($X = 900 - 1100$).

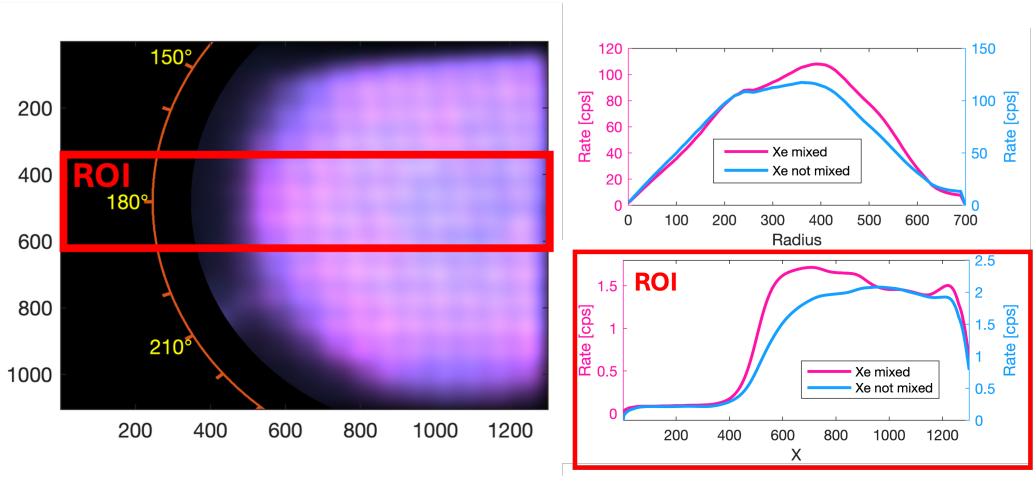


Figure 5.11: Pseudo-colors image of Xe plasma in the mixed (pink) and not-mixed (blue) cases. A rectangular ROI is defined in the middle region (red square) (left) - Radial projection of the two components of the image, integrated over all the theta angles (top-right) - x projection into the rectangular ROI (bottom-right).

The emission projection in this middle region of the image shows a flat profile of Xe emission in the not-mixed case with a maximum around the center of the plasmoid ($X \simeq 1000$), whilst the profile in the mixed

case is clearly peaked around $X \simeq 650$, much closer to the plasma-halo separatrix region corresponding to the ECR isosurface [59].

The emission profile in the outer region is also steeper towards the ECR layer in the mixed case, as confirmed by observing both the X projection in the range $X \simeq 400 - 600$. Figure 5.11-top-right plots the radial projection of both the images, convoluted above all the azimuthal angle. The scale is similarly normalized on $R = 0 - 250$, corresponding to the extraction hole region. This projection provides a clearer view of the plasma hollowness, being the gas-mixed emission higher in the range $R \simeq 400 - 600$.

Figure 5.12 shows the azimuthal projection of Xe emission in the two mixing cases, in the radial range of $R = 400 - 700$ to highlight the non-axis-symmetrical differences between the confinement structures. The result confirms the same behavior of the Ne+Kr case, observing the depletion at $\theta \simeq [150, 210, 270]$ and the enrichment at $\theta \simeq [180, 230, 300]$, which suggest the displacement of the Xe species into the magnetic gaps in the gas-mixed case.

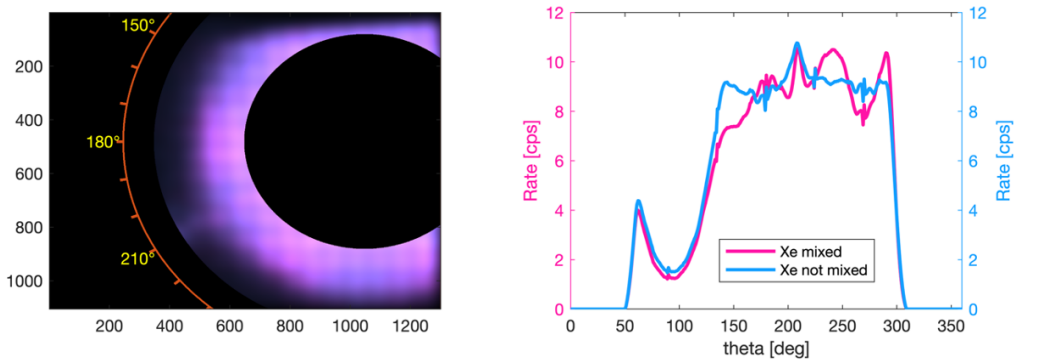


Figure 5.12: Azimuthal projection of Xe emission in the two mixing cases (mixed - pink and not-mixed -blue), into the circular crown shown on the left ($R = 400 - 700$). Non axis-symmetrical differences are observed.

**Splitting of the Xe $L\alpha$ fluorescence line** An interesting evidence has been observed in the Ar+Xe set of measurements: the L fluorescence line of Xe ($E_{L\alpha} = 4.110keV$) results to be splitted into a set of lines.

Figure 5.13 shows the spectra measured in the Ar+Xe configurations, respectively obtained in the high-resolution (left) and low-resolution (right) modes of CCD data analysis (explained in section 3.5.5).

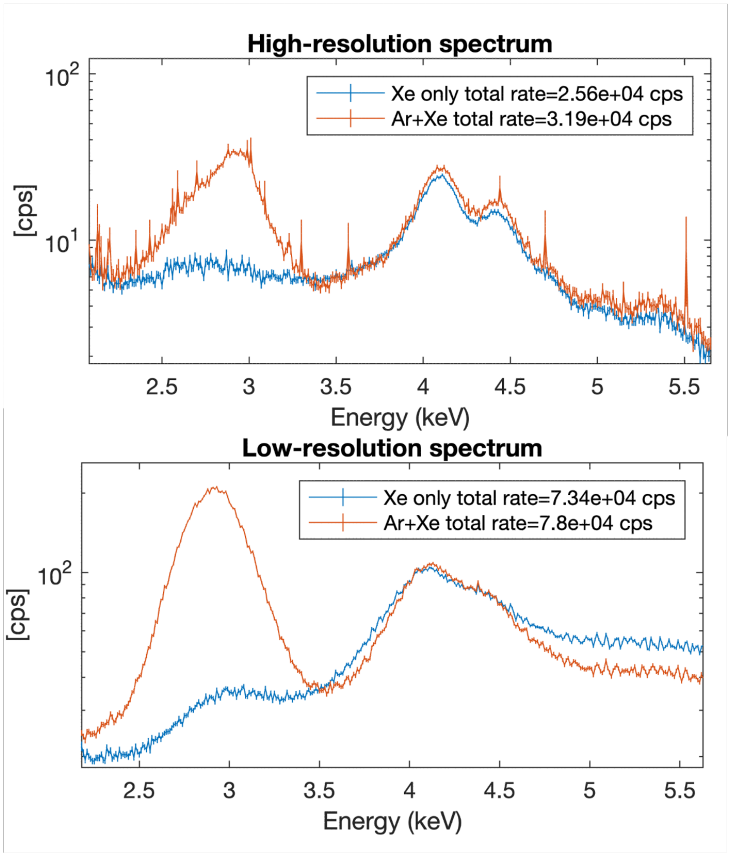


Figure 5.13: Energy spectra measured in the Ar+Xe mixed (orange) and Xe-only (blue) cases, obtained in the high (left) and low (right) energy resolution modes.

A set of lines is observed in the energy range of $4 - 5keV$ (high-resolution spectrum), respectively peaked at 4.11; 4.42; 4.73; 5.01 $keV$, with decreasing intensity. None of these lines are observed in the acquisitions without Xe gas, therefore excluding the contamination of the

spectrum with the fluorescence of other elements.

Furthermore, the possible contribution of the escape and pile-up phenomena on this series of peaks is excluded too, since the expected artifact lines would be unsuitable with the observed splitting.

Only two of these lines (4.11; 4.42 $keV$) are slightly resolvable in the full-efficiency analysis mode (figure 5.13-right), making the comparative imaging analysis possible.

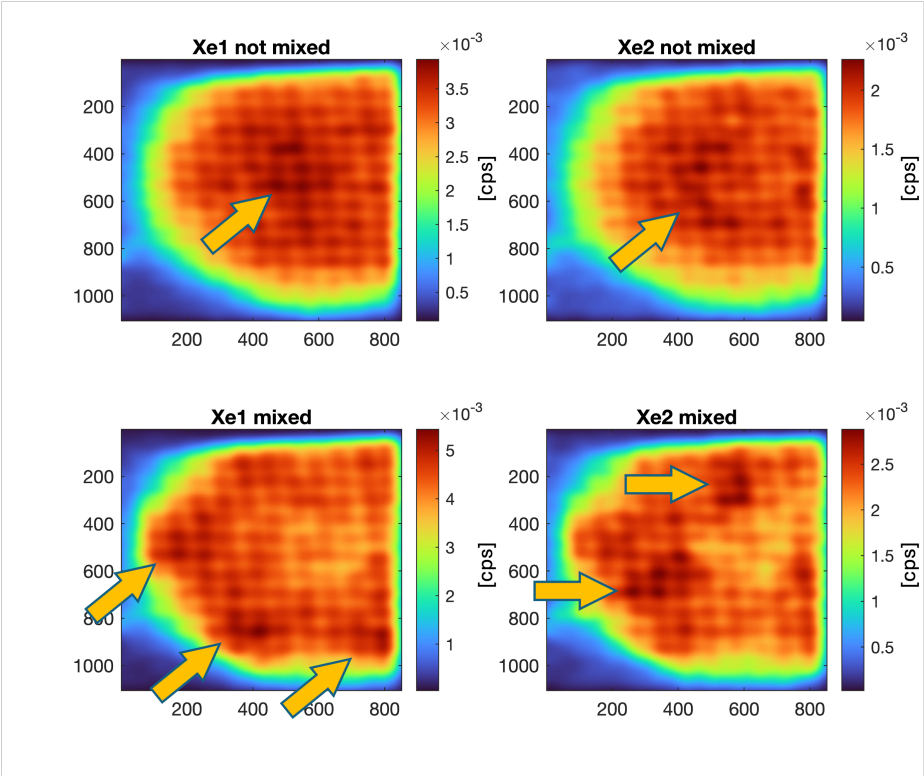


Figure 5.14: Images of the splitted lines of Xe, respectively defined as "Xe1" and "Xe2" in the mixed (right) and not-mixed (left) cases. The evidence of morphological differences is highlighted with the arrows. A gaussian filter of $\sigma = 25 pixels$ has been applied to smooth and lower the spatial resolution to reduce the squared mesh modulation effects and emphasize the features of plasma morphology. The multi-color scale bar helps to highlight the image differences.

Figure 5.14 shows the images of the first two lines, defined as Xe1 (energy range: $3.7 - 4.3keV$, left column) and Xe2 (energy range: $4.3 - 4.7keV$, right column), distinguishing the not-mixed case (top row) and the mixed case (bottom row).

A gaussian filter of $\sigma = 25pixels$ has been applied to smooth the images, lowering the spatial resolution to reduce the squared mesh modulation effects and emphasize the features of plasma morphology.

Morphological differences are slightly visible comparing each couple of images (left and right images on the same row), evidencing a different displacement of plasma into the plasmoid projection.

In particular, the Xe1 line emission in the not-mixed case is maximized around the center of the plasmoid (figure 5.14-top left), and the Xe2 line is maximized in a circular crown region around the extraction hole projection (figure 5.14-top left). The maxima regions are highlighted with yellow arrows.

In the gas-mixed case, the maxima of Xe1 are located in the vertexes of the hexagonal plasma shape (figure 5.14-bottom left), and the maxima of Xe2 are located into a region corresponding to the extraction-side magnetic branch.

This result will be commented in the discussion section.

### 5.1.3 Discussion

The results shown in this section provide a relevant contribution in the comprehension of the gas-mixed plasma dynamics: several phenomena predicted by theory and simulations have been successfully observed and benchmarked.

Although a different physics case has been studied, the outcome of the present study is consistent with the simulations performed in *Mironov et al.* publication [58], where an indication of plasma hollowness was observed in the Kr density when mixed with a lighter gas species (oxygen, in the specific case).

The analysis presented in figure 5.11 shows a steeper emission profile besides the ECR layer projection, in the gas-mixed case. This is consistent with the hypothesis of the increase of potential dip in gas-mixed mode [58], and in general with the predictions of the plasma structure in the

plasmoid-halo and double-layer-based models [59].

Being the X-ray fluorescence emission intensity approximately proportional to the product of electron and ion densities $n_e n_i$, the observed emission profile in both the gas-mixing configurations is consistent with the $n_e$ and $n_i$ profiles shown in *Mascali et al.* [59] (figure 2.6). The hypothesis of the potential dip value increase in gas-mixing mode is then consistent with the observed steepness variation in both the Xe and Kr radial profiles at the ECR layer (figures 5.8-right, 5.11-right).

Moreover, the evidence of the inhomogeneous plasma displacement in the "magnetic gaps", namely, the regions in between the two tri-cuspidal series of magnetic branches, is a relevant indication about the confinement morphology in gas-mixing mode (figures 5.8-left, 5.12-right), providing an interesting benchmark to support further Particle-In-Cell and electrostatic simulations about the double-layer models.

An interesting result has been obtained in the Xe L-line splitting investigation: morphological differences have been observed comparing the images of the two main Xe emission lines observed in the Ar+Xe configurations (figure 5.14).

This evidence leads to the hypothesis of being barely sensitive to the charge state spatial distribution, which is absolutely a new result in the field of X-ray plasma diagnostics.

The line emission of the single ionized state of Xe is in fact limited to the $K\alpha$, $\beta$ and $L\alpha$ lines, although a series of further lines has been observed in plasma (figure 5.13).

In the singly ionized state of Xenon ($Xe^{+}$), the observable X-ray fluorescence lines are the K$\alpha$ (29.779 keV) and K$\beta$ (33.624 keV) transitions, as well as the L$\alpha$ (4.109 keV) line, although a series of further lines has been observed in plasma (figure 5.13).

A calculation on the emission lines has been performed using FLY-CHK [73], a collisional-radiative code that computes radiative properties of plasmas, to well understand the energy shift in presence of high charge states, obtaining that the $L_\alpha$ emission energy varies as a function of the charge state.

Figure 5.15 presents the calculated energies of the L$\alpha$ emission line for xenon ions up to $Xe^{43+}$. It is evident that, at low charge states (less

than 25), the expected energy of the L$\alpha$ line remains below 4.2 keV. For higher charge states, the line energy exhibits a more pronounced increase, reaching approximately 4.6 keV for $Xe^{43+}$. From $Xe^{44+}$ onward, any L-alpha transitions are expected because there are no electrons in the M-shell.

This trend reflects the progressive influence of the increasing ionic charge on the binding energies of the L-shell electrons and the resulting shift in the X-ray fluorescence emission.

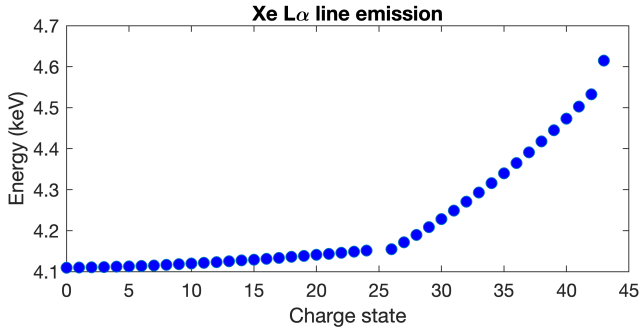


Figure 5.15: FLYCHK calculation of $Xe - L_\alpha$ energy shift as a function of the charge state, from $Xe^{1+}$ to $Xe^{44+}$.

In conclusion, the line previously labeled as "Xe1" corresponds to the well-known L$\alpha$ emission from neutral and low-charge-state xenon, while the line designated as "Xe2" is consistent with L-shell emission from higher charge states and can be attributed to the highly ionized component of the plasma.

Therefore, the observed morphology of Xe2 (figure 5.14-bottom right) is ascribable to a confinement map of the highly ionized states of Xe in plasma, which suggests a remarkable explanation to the gas-mixing effect: the concentration of the higher charge states of the heavier element into the magnetic branches is consistent with the high-charge-state current enhancement, mainly observed in the gas-mixing effect.

Deeper investigations should be done on this, to validate the effective possibility of performing charge-state-resolved imaging by fluorescence line splitting, to better understand the main mechanisms of the gas-mixing effect.

In perspective, the potentiality of such imaging technique could be applied to fundamental plasma physics, as well as to the further optimization of the highly charged ion current extraction from the ECR ion sources, the latter being one of the most relevant criticalities of such facilities.

## 5.2 Time-resolved measurements of plasma transients

This measurement was devoted to study the time evolution of plasma transients after the RF the switch-off.

The space-time-resolved diagnostic application to the study of plasma transients can provide relevant elements about the time evolution of such phenomena, making also possible the investigation of the RF involvement on the plasma confinement structures.

Two different kinds of measurements will be presented in this section, in order to investigate on several aspects of the time-resolved phenomena observable in a pulsed ECR plasma.

The first set of acquisitions was performed to obtain a fluorescence-filtered imaging comparison between the steady-state emission of plasma (RF-ON) and the respective emission time-integrated during the whole decay transient (RF-OFF) in a time window of $100ms$.

The second measurement consists of a series of short acquisitions in order to obtain a time-lapse of plasma decay with the maximum time resolution allowed by the X-ray shutter ($\sim 8.6ms$).

Several configurations have been explored, varying the magnetic confinement parameters, the RF power and the gas pressure.

### 5.2.1 Experimental configuration

A pulsed RF signal was generated, producing a periodic plasma ignition and switch-off. Different configurations of RF power, gas pressure and magnetic field have been explored, as shown in table 5.4, setting a fixed series of time windows for each acquisition.

| Config. ID | Pressure [mbar] | RF net power [W] | $B_{max}/B_{min}$ |
|---|---|---|---|
| 0 | $1.30 \cdot 10^{-6}$ | 280 | 2.29 |
| 1 | $1.35 \cdot 10^{-6}$ | 240 | 1.75 |
| 2 | $1.35 \cdot 10^{-6}$ | 340 | 1.75 |
| 3 | $1.00 \cdot 10^{-6}$ | 340 | 1.75 |
| 4 | $1.00 \cdot 10^{-6}$ | 240 | 1.75 |
| 5 | $1.35 \cdot 10^{-6}$ | 340 | 2.29 |
| 6 | $1.35 \cdot 10^{-6}$ | 240 | 2.05 |
| 7 | $1.00 \cdot 10^{-6}$ | 240 | 2.29 |
| 8 | $1.00 \cdot 10^{-6}$ | 340 | 2.29 |

Table 5.4: Explored configurations for time-resolved measurements.

The extracted current of $Ar^{8+}$ was continuously monitored during all the measurements, ensuring the repeatability of the observed physics.

As shown in the preliminary real-time data observed in the $Ar^{8+}$ current extraction (figure 5.16), the afterglow phase dynamics is prone to a time evolution study in the scale of few milliseconds (suitable with the lowest exposure time of 8.6$ms$ allowed by the X-ray diagnostics).

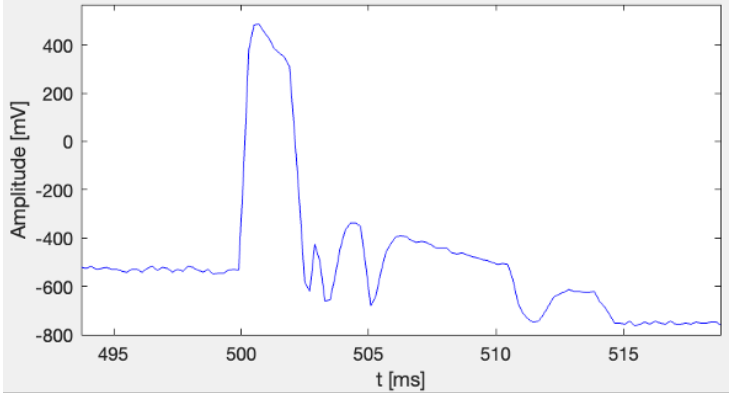


Figure 5.16: Example of $Ar^{8+}$ current extraction dynamics in the configuration n.7.

The time-resolved measurement in single-photon counting mode requires a set of repeated exposures at each fixed delay respect to the RF

switch-on master trigger, subsequently exploring a set of different delay values.

A first acquisition was performed (table 5.4 – configuration 0) with a 2 s RF pulse period and a 1 s width, defining two time windows 100 ms wide (106.3 ms effective), before and after the RF switch-off, as shown in table 5.5, exploring the plasma emission time-integrated during all the afterglow decay transient. An additional acquisition of the RF-ON configuration was made at 10 ms (16.0 ms effective) exposure time, in order to obtain the HDR imaging, due to the very high dynamic range of plasma emissivity observed in the steady-state.

| **Measure** | **Number of frames** | **Exposure time [ms]** | **Delay [ms]** |
|---|---|---|---|
| RF ON | 2180 | 106.3 | 800 |
| RF ON | 1000 | 16.0 | 800 |
| RF OFF | 3000 | 106.3 | 1000 |

Table 5.5: Acquisition setting for the time-resolved HDR plasma measurement into two time windows.

The readout time required for each frame was optimized by defining a ROI on the acquisition system (figure 5.17-left), allowing to balance the experimental schedule with the required amount of data collection. Such a ROI was defined to frame the most relevant portion of the field of view, including the extraction hole, the total structure of a magnetic branch +pole and a wide portion of the plasmoid. By this way, the total readout time was lowered from 4.4 s to 1.7 s, making possible the acquisition of 6180 frames in a couple of hours.

The acquisition of plasma configurations from 1 to 8 (table 5.4) was performed by defining a fixed set of delay values to explore all the transient dynamics. In this case, being the whole measure more time-consuming, a set of smaller rectangular ROIs (figure 5.17-right) was defined to focus well defined features of plasma structure: the radial profile of the plasmoid, from the extraction hole to the ECR separatrix; the left magnetic branch; the radial pole. The readout time of the latter configuration was 827 ms, allowing a frame acquisition with a shorter RF trigger (1 s pulse

period, 500 ms width).

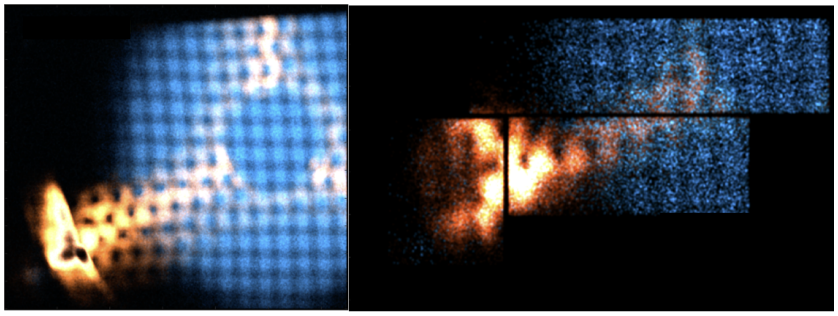

Figure 5.17: Steady-state plasma acquisition (RF-ON) in the two configurations: bigger ROI for measure n.0 (left) - smaller ROI for measures n.$1-8$ (right).

Table 5.6 shows the configuration of a plasma switch-off time lapse measurement, reporting the number of frames and the delay of each acquisition.

The first measure (ID=1) is related to the plasma steady state (Delay < 500ms), before the RF switch-off.

The single frame exposure time was set with a logical pulse of 5 ms, generating an effective exposure of 8.6 ms including the closing transient of the shutter (shown in detail in section 3.5). The trigger logic is represented in figure 4.9, showing the pulsed RF signal (in yellow), whose positive edge is the master trigger; the CCD acquisition is triggered at the preset delay time, in blue, once the "clean until trigger" function is activated, continuously exposing and cleaning the sensor every $30\mu s$ while waiting for trigger; the shutter pulse (in pink) is delayed 4 ms less than the CCD trigger on, to exclude the opening transient. The red line schematizes the expected X-ray emission intensity with the afterglow peak and the subsequent decay.

| Measure ID | Number of frames | Exposure time [ms] | Delay [ms] |
|---|---|---|---|
| 1 | 500 | 8.6 | 400.0 |
| 2 | 500 | 8.6 | 500.0 |
| 3 | 200 | 8.6 | 500.1 |
| 4 | 200 | 8.6 | 500.2 |
| 5 | 200 | 8.6 | 500.3 |
| 6 | 500 | 8.6 | 500.4 |
| 7 | 200 | 8.6 | 500.5 |
| 8 | 200 | 8.6 | 501.0 |
| 9 | 200 | 8.6 | 502.0 |
| 10 | 200 | 8.6 | 504.0 |
| 11 | 500 | 8.6 | 507.0 |
| 12 | 200 | 8.6 | 510.0 |
| 13 | 200 | 8.6 | 513.0 |
| 14 | 200 | 8.6 | 515.0 |
| 15 | 200 | 8.6 | 517.0 |
| 16 | 200 | 8.6 | 519.0 |
| 17 | 200 | 8.6 | 520.0 |
| 18 | 200 | 8.6 | 525.0 |

Table 5.6: Time-windows configuration for time-lapse measurements, reporting the number of frames and the delay for each acquisition.

### 5.2.2 Results

**Time-resolved measurement: RF-ON versus RF-OFF** The measure number 0 (see table 5.4) consists of the investigation of two time windows of 106.3 ms, obtaining two images which compare the plasma emission before and after the RF switch-off, integrated over 2180 and 3000 frames respectively. In addition, the "RF-ON" image contains the HDR contribution of 1000 short-exposed frames into the brightest region, corresponding to the pole emission and a portion of the left branch.

Figure 5.18 reports the two images obtained by a filter on Al and Ar K-fluorescence lines, represented in respective pseudo-color scales (orange-yellow and blue).

The lower part of the picture shows the x-projections of the Ar image

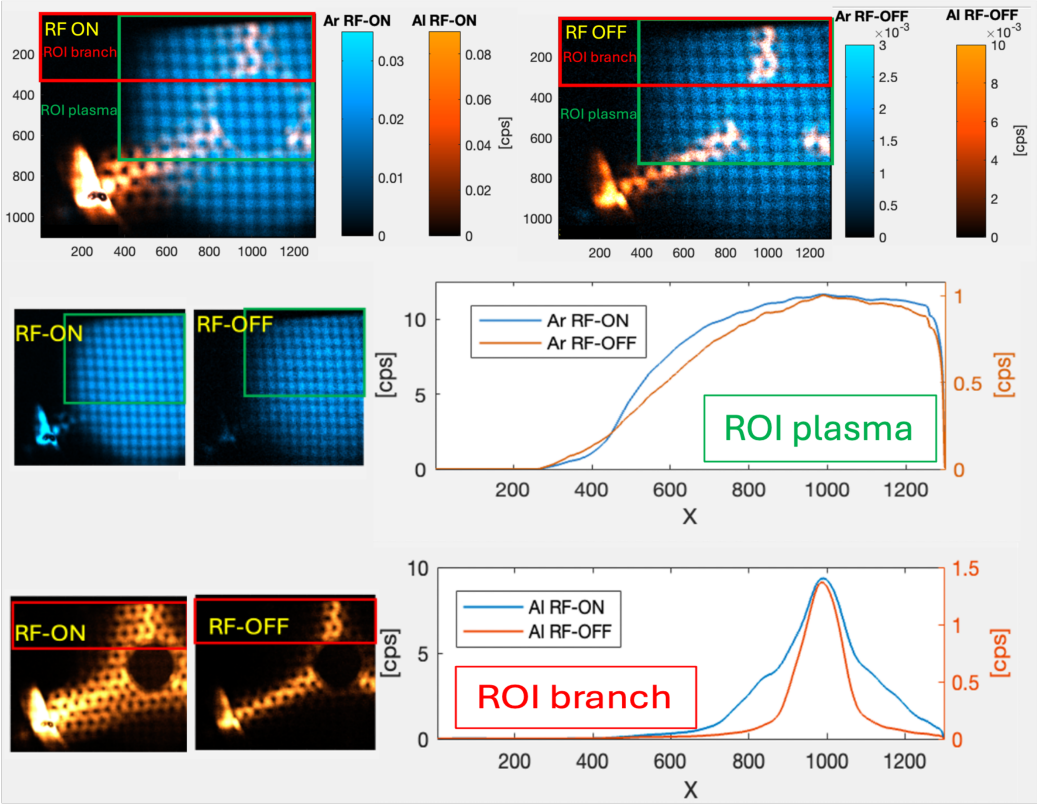


Figure 5.18: Set of images obtained by filtering the Al and Ar K-fluorescence lines, represented in pseudo-color scales (orange and blue). Steady-state plasma emission (RF-ON, left) and decay transient (RF-OFF, right). Two ROIs have been defined respectively for the plasma analysis (green square) and for the upper branch analysis (red square). The comparison between RF-ON and RF-OFF on the x-projections over the two ROIs is shown at the bottom.

over the full frame (left) and of the Al image over the red-squared ROI (right), comparing the pre and post RF-switch-off profiles (RF-ON and RF-OFF). The comparison suggests a shrunk morphology on both the plasmoid and the magnetic branches shapes.

Figure 5.19 shows the same pictures separately plotted in a more quantitative color-scale, highlighting the morphological differences between the two plasma configurations.

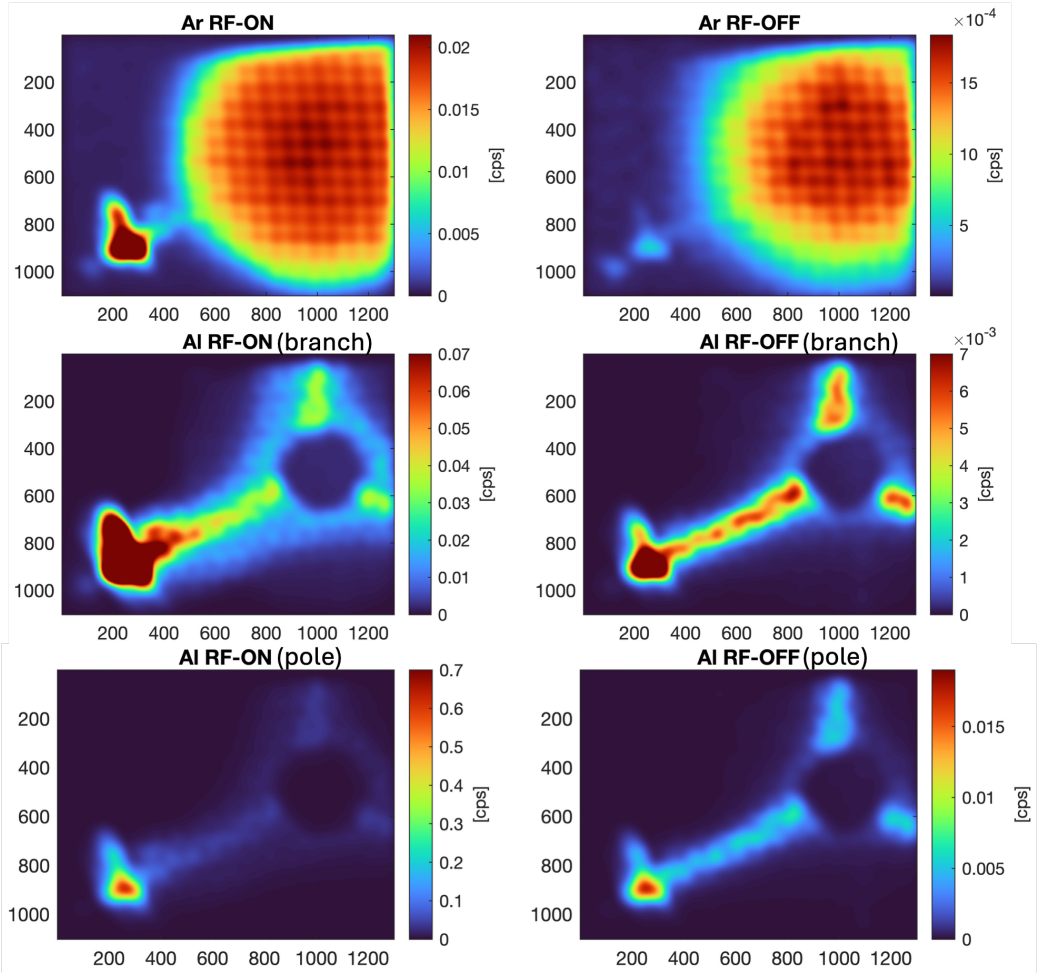


Figure 5.19: Steady-state and decay transient images reported separately for Ar and Al lines. A gaussian filter of $\sigma = 25 pixels$ has been applied to smooth and lower the spatial resolution to reduce the squared mesh modulation effects and emphasize the features of plasma morphology. The multi-color scale bar helps to highlight the image differences. The color scales are normalized to the brightest values of the relevant regions of interest, which are respectively the central region of the plasmoid (Ar images), the the brightest part of the magnetic branch (Al images - branch) and of the magnetic pole (Al images - pole).

A gaussian filter of $\sigma = 25 pixels$ has been applied to smooth the images, lowering the spatial resolution to reduce the squared mesh modulation effects and emphasize the features of plasma morphology.

The color scales have been normalized to the brightest values of the relevant regions of interest, which are respectively the central region of the plasmoid (Ar images) and the the brightest part of the magnetic branch (Al images - branch) and of the magnetic pole (Al images - pole). In this way, although the absolute emissivity is significantly lower, the plasmoid shrinking in the RF-OFF case (Ar images, on the top), as well as the shrinked shape of the deconfinement branches (Al images - branch) are better observable.

Being the dynamic range of the image too wide to fit into a linear color scale, the images at the bottom have been rescaled to the maximum intensity at the poles in to highlight the balance between the pole region and the magnetic branch.

The different balance between these two regions on the two images shows a relevant variation, suggesting that a relevant component of plasma loss in the radial direction (magnetic pole region) is reduced of a factor $\sim$ 2.5 respect to the axial loss intensity (magnetic branch) during the plasma decay in the absence of the pumping wave.

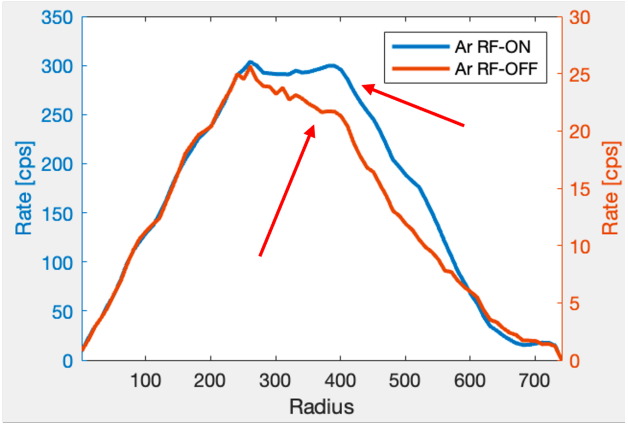


Figure 5.20: Radial projections comparison of the Ar emission in the RF-ON vs. RF-OFF cases. The y-scale is normalized to equalize the range $R = 0 - 250$.

The evidence of the plasmoid shape shrinking is highlighted in figure 5.20, showing the radial profile of the Ar emission map, centered on the simmetry axis of the plasma chamber.

**Time-lapse analysis of plasma switch-off** The measurements 1-8 (table 5.4) explore all the decay transient with 17 time steps between 0 and 25 ms after the RF switch off (see table 5.6). The evolution of the extracted $Ar^{8+}$ current has been registered for each measurement by the oscilloscope.

Figure 5.21 shows the normalized Ar8+ extracted current profile during the plasma switch-off transient for all the explored configurations.

Each plot reports the RF-ON (high) and RF-OFF (low) baselines, the rise time of the afterglow peak (when present) and two fall time components, namely fast and slow, respectively defined as the decay time over the two baselines.

The current extraction dynamics (reported in figure 5.21) shows a common behavior above all the configurations: the afterglow peak occurs at the RF-OFF trigger, whose amplitude depends on the operative conditions (pressure, power, magnetic field). Subsequently, a modulation pattern is observed in a variable time scale of $\sim 3 - 13ms$, suggesting a periodic plasma ignition post-afterglow, in accordance with the measurements reported by *Tarvainen et al.* in [65] (figure 2.7).

Such phenomenon is particularly visible in configurations n. 3, 4, 7, 8, where a short pulse followed by a quasi-plateau is repeated few times.

Such behavior is more pronounced at a lower pressure value ($1.00 \cdot 10^{-6} mbar$).

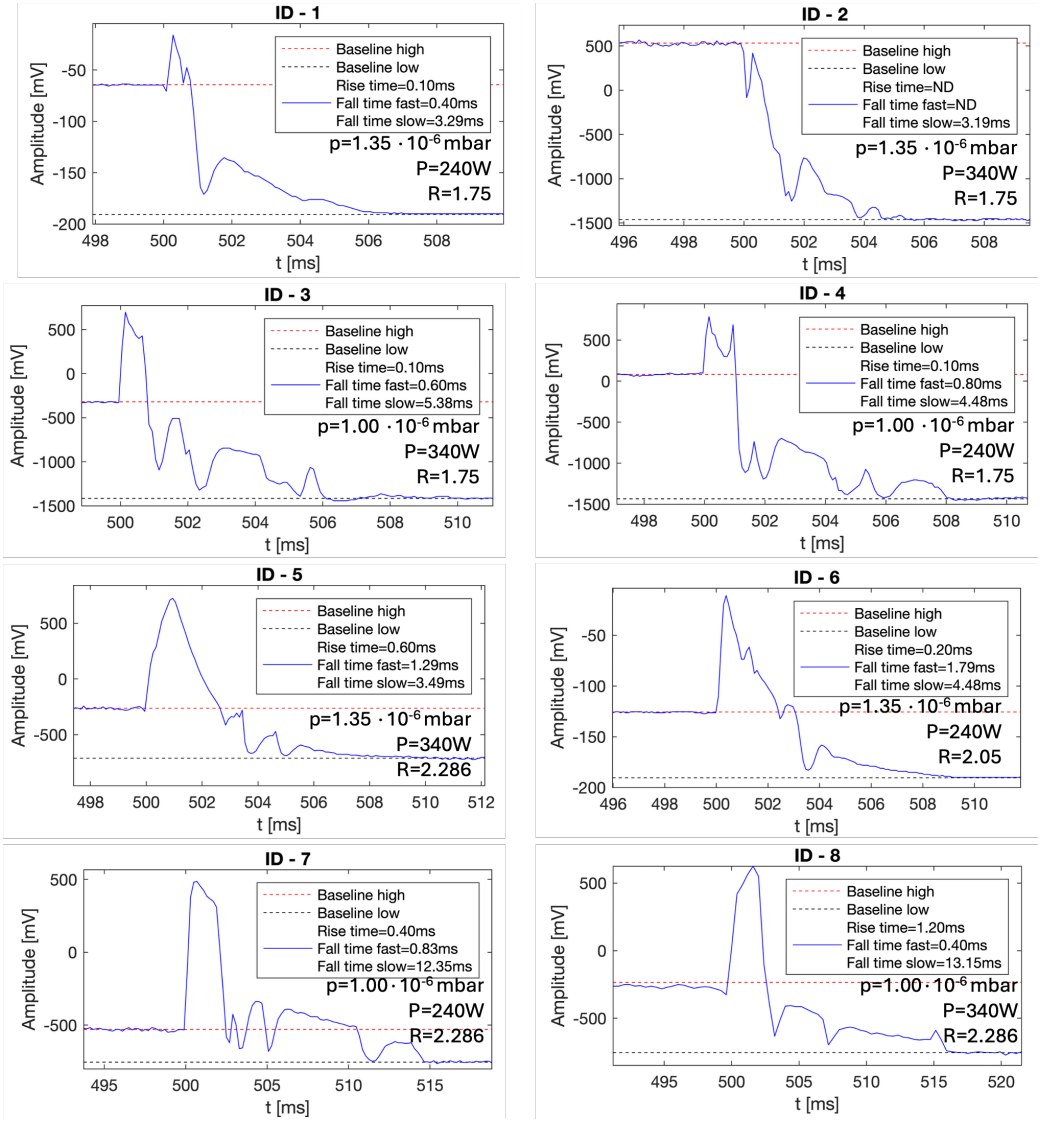


Figure 5.21: Extracted current dynamics of $Ar^{8+}$ of the explored configurations $1-8$.

Table 5.7 summarizes the main features of the extracted current for each configuration, defining the rise time, fall time and aplitude of the afterglow peak.

| Config. ID | Rise time [ms] | Fall time [ms] | Peak amplitude | Pressure [mbar] | RF power [W] | $B_{max}/B_{min}$ |
|---|---|---|---|---|---|---|
| 1 | 0.1 | 0.4 | 3.3 | $1.35 \cdot 10^{-6}$ | 240 | 1.75 |
| 2 | ND | ND | 3.2 | $1.35 \cdot 10^{-6}$ | 340 | 1.75 |
| 3 | 0.1 | 0.6 | 5.4 | $1.00 \cdot 10^{-6}$ | 340 | 1.75 |
| 4 | 0.1 | 0.8 | 4.5 | $1.00 \cdot 10^{-6}$ | 240 | 1.75 |
| 5 | 0.6 | 1.3 | 3.5 | $1.35 \cdot 10^{-6}$ | 340 | 2.29 |
| 6 | 0.2 | 1.8 | 4.5 | $1.35 \cdot 10^{-6}$ | 240 | 2.05 |
| 7 | 0.4 | 0.8 | 12.4 | $1.00 \cdot 10^{-6}$ | 240 | 2.29 |
| 8 | 1.2 | 0.4 | 13.1 | $1.00 \cdot 10^{-6}$ | 340 | 2.29 |

Table 5.7: Main features of the extracted current dynamics on the explored configurations $1 - 8$.

The temporal X-ray emission profile have been studied on several energy ranges:

- Full energy: 0 - 50 keV
- Al $K\alpha$ line (deconfinement fluxes): 1.1 – 1.8 keV
- Ar $K\alpha$ line (confined plasma): 2.4 – 3.4 keV
- Higher energy spectrum: 3.5 – 50 keV

Figure 5.22 shows the extracted current evolution (in green) together with the full-frame integrated intensity of all the plasma emission components, in all configurations.

Each experimental point represents the starting edge of an 8.6 ms exposure time window.

In order to study the relative variation on time, the intensity is normalized to each respective value at the RF-ON time step (t = 400 ms, not shown in the plots). It is interesting to notice that the decay profile differs between one track and another. In particular, the high-energy component (purple track) has a slower decay respect to the others in configurations 1, 2, 3, 4, 6, suggesting a peculiar decay dynamic of the high energy plasma electron components. Moreover, the Ar fluorescence decay in configurations 5, 7, 8 shows a different trend respect to the other components, which determines a different dynamics between confined and deconfined plasma.

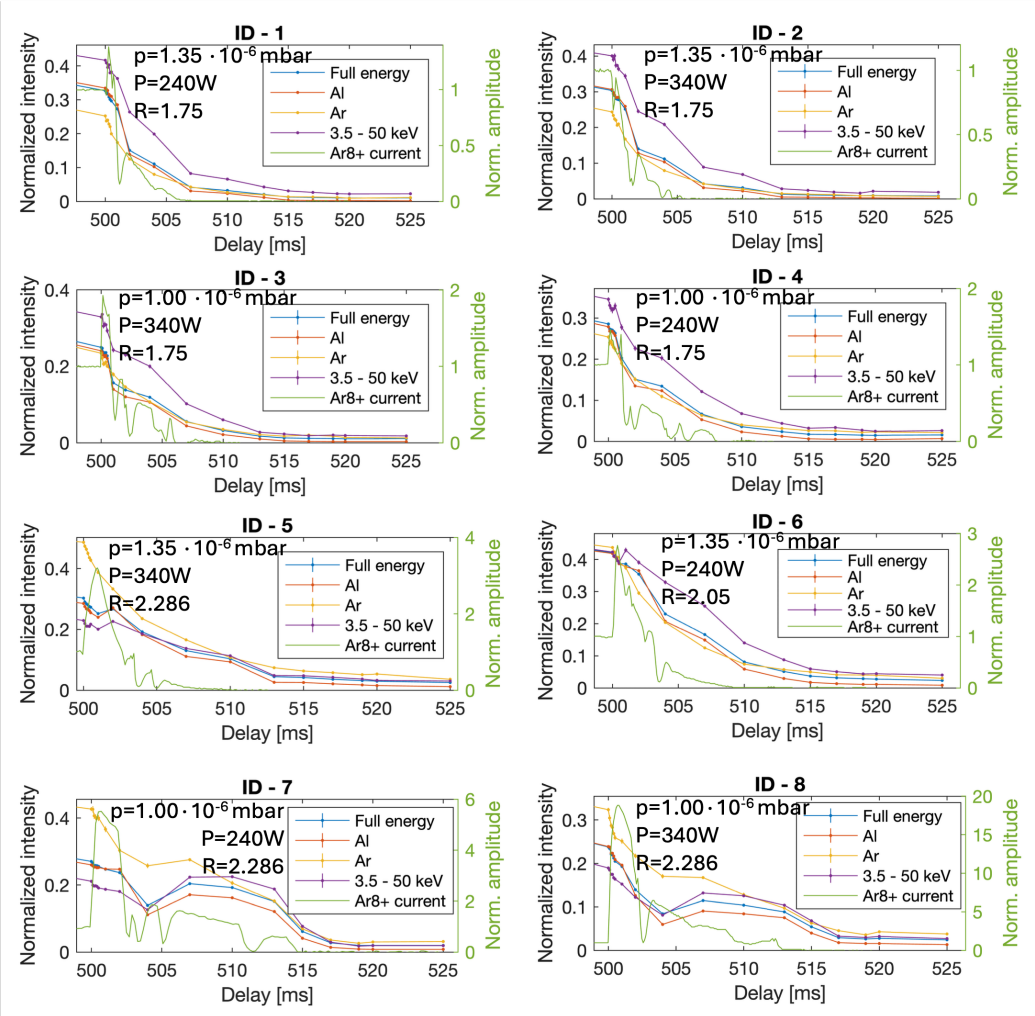


Figure 5.22: Extracted current evolution (in green) and full-frame integrated intensity of all the plasma emission components (full energy, Al, Ar, high energy, in all configurations.

It is interesting to focus on configurations 7 and 8, where all the components show a minimum value at 504 ms, followed by an increase and subsequent decay. This observation suggests a delayed plasma re-ignition in the $5 - 10ms$ time scale.

The corresponding image analysis is now reported. For the sake of

example, a series of 4 images (figure 5.23) is reported about configuration n.7, showing only four time steps: 400.0 ms (RF-ON), 500.0 ms, 500.4 ms, 507.0 ms.

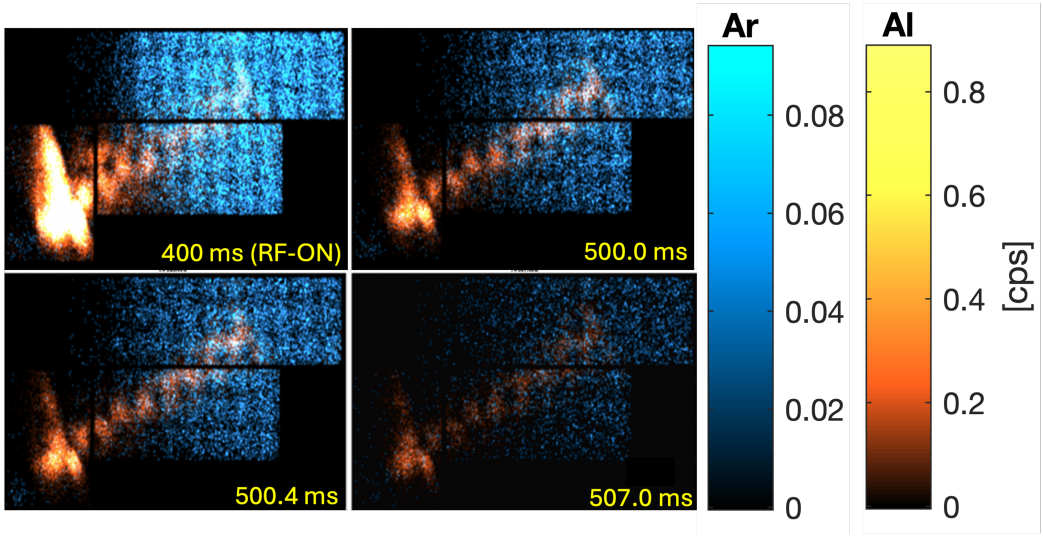


Figure 5.23: Series of images with four representative time windows acquisitions about configuration n.7.

A first comparison is shown in figure 5.24 between the RF-ON (T1 = $400.0 - 408.6ms$) and the first RF-OFF branch profile ($500.0 - 508.5ms$ time window), highlighting the evidence of a different deconfinement morphology between the two plasma regimes. In particular, the balance between the pole ($X \sim 300$) and the branch ($X \sim 700$) emission decreases significantly of a factor $\sim 2.5$, as shown in the previous section (see figure 5.18).

Figure 5.25 shows few images of the Al emission, rotated of 30° to obtain a better projection of the image intensity. The whole RF-OFF decay series ($500.0 - 533.6ms$) of X projection profiles is then shown in figure 5.26, excluding the RF-ON case which wouldn't fit into the same intensity scale. An orange to yellow time scale has been adopted for a clearer plot reading.

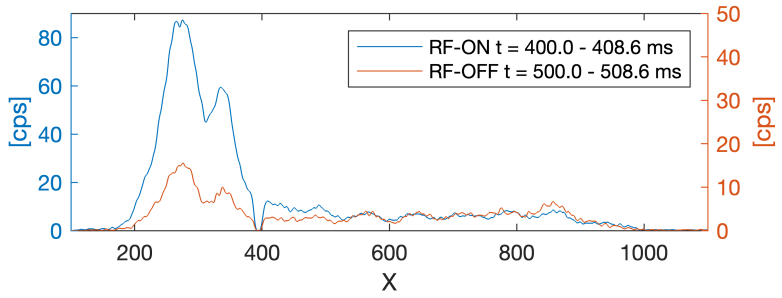


Figure 5.24: Comparison between the x-projection of the Al emission in the two first time windows, corresponding to the steady-state and the first time-step of plasma decay.

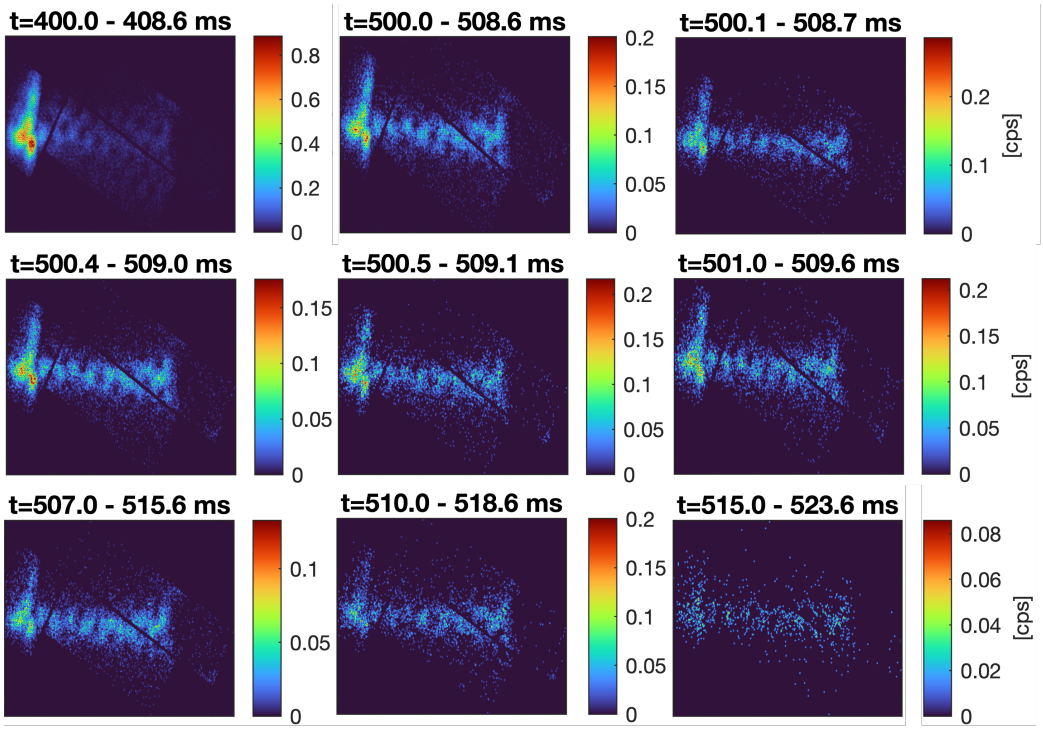


Figure 5.25: Images of the Al emission, rotated of 30° to optimize the x-axis projection of the image intensity. The color bar is auto-scaled on each image.

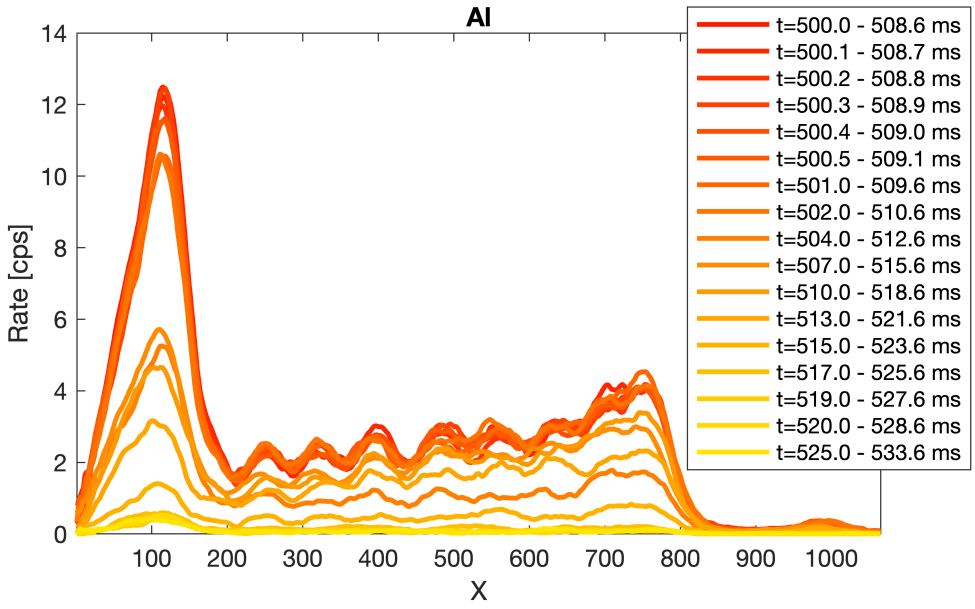


Figure 5.26: RF-OFF decay series ($500.0 - 533.6ms$) of the x-projection profiles (Al emission).

### 5.2.3 Discussion

A time-resolved study of ECR plasma decay transient was presented in this section, observing for the first time the evolution of the confinement structures of plasma.

The first evidence in the present study concerns the decay of the electrostatic confinement structure of plasma: its dynamics is significantly different when observing the confined plasma emission versus the magnetic branches/poles. This is consistent with the removal of the ambipolar barrier of the potential dip (see section 2.5.2), as predicted by the double-layer based models [59], with the consequent expulsion of the high charge state ions that were confined electrostatically in the steady-state.

The decaying plasma appears shrunk in correspondence with the ECR surface, due to the rapid decay of the double layer confinement, determining a lower emissivity from these regions.

This represent a relevant benchmark about the potential dip - double

layer dynamics, since no direct observations of this phenomenon have been found in literature.

The plasma loss dynamics is then governed by the different confinement scheme in the absence of the RF phenomena.

Secondly, the periodic plasma re-ignition during the decay transient has been observed in several configurations, endorsing the hypothesis of the afterglow instabilities occurrence (*Tarvainen et al.* [65] - figure 2.7).

Although the time resolution of $8.6ms$ is not sufficient to well resolve the dynamics of such phenomenon occurring in the time scale of $\sim 1ms$, this is the first time-resolved investigation of the X-ray emission dynamics of a decaying plasma. In perspective, a higher time-resolution measurement is advisable also relinquishing to the spatial resolution (i.e. fast SDD acquisitions), to better understand the differential decay dynamics between confined and deconfined plasma. On the other hand, further developments on faster energy-space-resolved acquisitions could carry to a deeper investigation on the structural dynamics of plasma during afterglow transient.

Finally, the effect of the RF-induced scattering has been quantified by comparing the plasma emission in the steady-state with the first stages of the decaying transient. The morphology of such phenomenon, contributing to the plasma deconfinement, has been studied, observing that the latter is more pronounced in the poles regions when the RF is ON, although the emission from the endplate during the decay is differently balanced between the magnetic branch and pole. In particular, the balance between the pole and the branch emission varies by a factor $\sim 2.5$.

## 5.3 Space-resolved electron density and temperature evaluation

This section shows the application of the emissivity model described in 1.4.3 to study the temperature and the density of plasma. Such a study has been performed on the X-ray imaging data obtained in the year 2018, during a previous experimental campaign on the Atomki B-minimum ECRIS, devoted at investigating the Single vs. Double frequency heating of ECR plasma [66]. Due to the originality of the work, concerning both the development of the technique and the achieved results, this content has been published as an independent study from the original aims of the measurement [67].

### 5.3.1 Experimental configuration

The experimental setup is reported in section 4, being the ECRIS the same of the previously shown measurements, with the difference of the plasma chamber structure. Titanium and tantalum layers have been respectively chosen for the extraction plate and the cylindrical wall, with the aim of distinguishing the radial plasma loss from the axial one [66]. A different CCD camera (Andor iKon-M) with similar spectroscopic features (energy resolution $\sim$ 240$eV$@8$keV$, squared pixel size 13$\mu m$) was used for this measurement, coupled to the plasma chamber with a pin-hole camera obscura without any shutter. This condition required the development of a specific algorithm to reduce the effects of the readout shift on the images [47].

The Ar plasma was excited at the power of 200$W$ and frequency 14.25$GHz$, with a gas pressure of $2.2 \cdot 10^{-6} mbar$.

### 5.3.2 Results

The fluorescence-filtered imaging analysis (figure 5.27) shows the plasma structure, which is analogous to the imaging results of the previous sections, except for the fluorescence lines of the metals involved in the deconfinement phenomena (Ti $K\alpha$ on the magnetic branches and Ta $L\alpha$ on the magnetic poles).

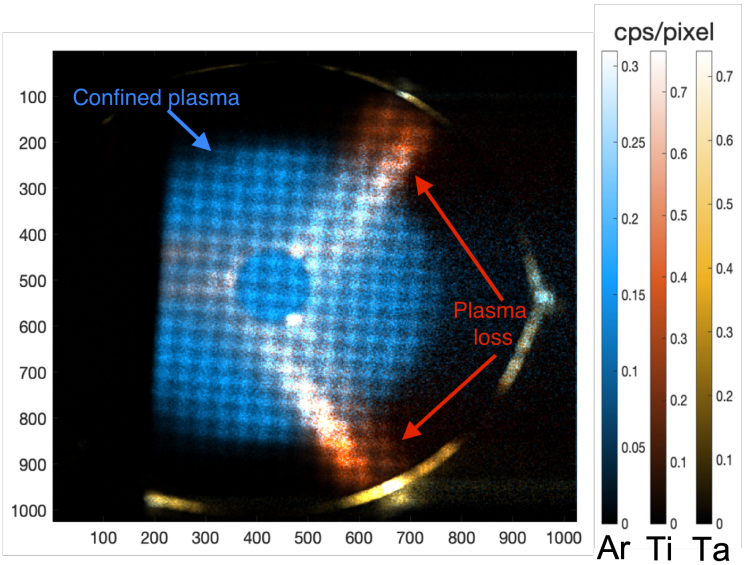


Figure 5.27: Pseudo-colors combined image with all the fluorescence components of Ar, Ti, Ta.

The emissivity model application is focused on the bremsstrahlung component of the spectrum in the energy range of $10 - 15keV$, corresponding to the emission induced by the warm electrons population.

The space-resolved analysis was obtained by defining a set of ROIs corresponding to several plasma regions (figure 5.28). In particular, circular sections of plasma projection were selected in order to study the radial profile of plasma parameters, reasonably assuming the azimuthal symmetry of the plasmoid. Also the right part of the image was excluded, mostly affected by a residual CCD readout effect, containing some traces of titanium emission.

The ROI extension was maximized in order to minimize the spectral statistical error.

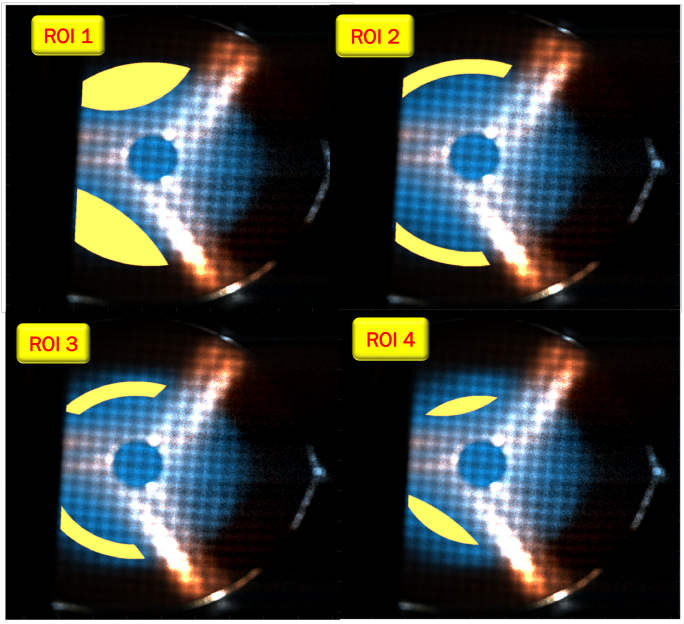


Figure 5.28: Set of ROIs selected (yellow shades) on the CCD image: radial sections of plasmoid projection, excluding the titanium emission and the right side of the image, mostly affected by readout residual effect.

The expression (1.47) was thus used to fit the bremsstrahlung experimental emissivity density in order to extrapolate the electron temperature and density.

The application of this model requires a rigorous determination of the geometrical detection efficiency $\Omega_g/4\pi$ and of the effective plasma volume $V_P$, to be done for each of the selected spatial ROIs in the plasma. On this purpose, a geometrical simulation was required, considering the overall geometry of the pin-hole optical system and the plasma chamber setup.

The plasma volume was identified as the region enclosed by the ECR surface, defined by the 3D-map of the resonant magnetic region. The local geometrical efficiency was defined for each point of a 3D plasma model

as the projection of a given subvolume of the plasma (voxel), projected across the aluminum mesh (hence, assuming its intrinsic transparency) and the pin-hole, onto the CCD detector.

Figure 5.29 shows the aluminum mesh (a), the optical simulation of the plasmoid through it (b) and the equivalent geometrical efficiency projection along the z axis (c).

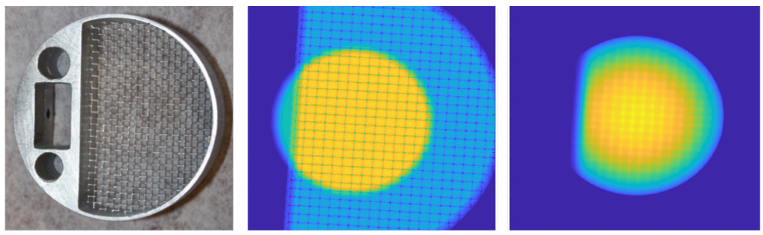


Figure 5.29: a) Aluminum mesh - b) Optical simulation of plasmoid with the mesh - c) Geometrical efficiency projection along the z axis

The emissivity density was studied in the set of ROIs defined in figure 5.28. Each ROI defined a 3D portion of plasma on which the volume $V$ and the efficiency $\Omega_g/4\pi$ have been summed.

The resulting emissivity density spectrum for ROI 1 is shown in figure 5.30 (red line). The blue line reports the weighted fit of $J^{M-B}_{bremss}(h\nu)$ (1.47), constrained in the range of $10-16\ keV$ (green line).

Table 5.8 and figure 5.31 report the extrapolated values of temperature and density in all the 4 ROIs, with respective error bars calculated by the experimental error propagation into the fit parameters.

The plasma electron density and temperature have been extracted with a precision between $9-16\%$ and $15-21\%$, respectively, allowing a preliminary characterization of plasma temperature and density profile.

In particular, the temperature shows a constant trend with an average value of $\sim 12.3\ keV$ in all the selected ROIs. The density profile decreases going from the inner region (ROI 4) to the external one (ROI 2), especially selected on the border of the plasmoid projection. The average values are measured in ROI 1.

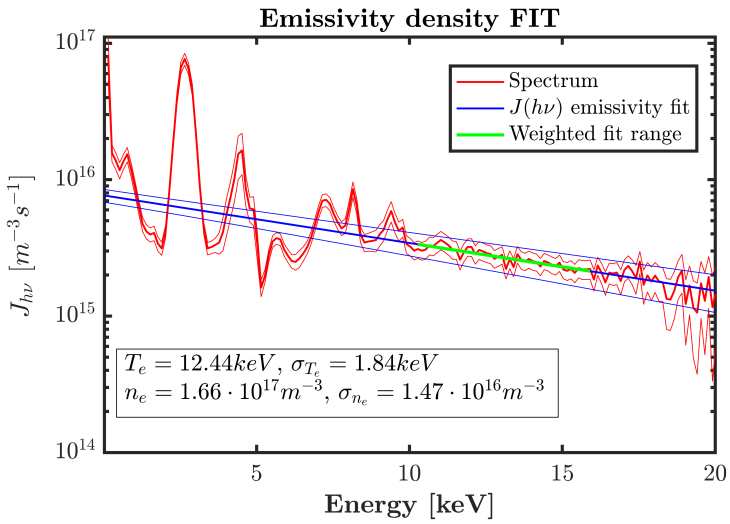


Figure 5.30: Emissivity density spectrum $J_{exp}(h\nu)$ in ROI 1 (red line); Maxwell-Boltzmann emissivity fit $J^{M-B}_{bremss}(h\nu)$ with respective error bars (blue line); fit range (green line). Temperature and density extrapolation is reported below.

| | **Temperature [keV]** | **Density $[m^{-3}]$** |
|---|---|---|
| ROI 1 | $12.44 \pm 1.84$ | $(1.66 \pm 0.15) \cdot 10^{17}$ |
| ROI 2 | $12.10 \pm 2.54$ | $(1.36 \pm 0.16) \cdot 10^{17}$ |
| ROI 3 | $12.67 \pm 2.60$ | $(1.71 \pm 0.27) \cdot 10^{17}$ |
| ROI 4 | $12.01 \pm 2.51$ | $(1.83 \pm 0.25) \cdot 10^{17}$ |

Table 5.8: Plasma electron temperature and density results, extracted in the four ROIs.

Being the experimental error mostly dependent on the spectrum intensity, the measurement can be in principle improved by extending the total measurement time and/or the spatial ROI dimensions, in a trade-off between parameters extrapolation accuracy, measurement time and space resolution.

Furthermore, the results are model-dependent: their significance depends on how the EEDF matches with the Maxwell-Boltzmann distribu-

tion. As mentioned above, further upgrades on the model are still under development, by implementing different distribution functions on simulated plasma environment and blending information coming from line emission part also [5].

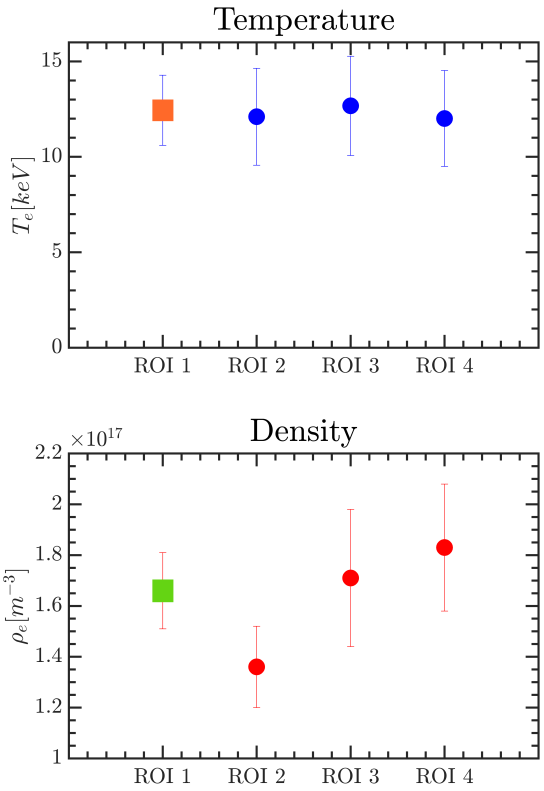


Figure 5.31: Plasma electrons temperature and density results, extracted in the four ROIs. ROIs from 2 to 4 (circles) go from plasmoid edge towards the axis; ROI 1 (square in different color) represents, in short, a kind of space-average of the ROIs 2-4.

### 5.3.3 Discussion

The spatially resolved spectral analysis here shown represents a relevant step forward enabling the study, for the first time, of the local ECR plasma parameters. The achieved results give important features about the ECR plasma structure and confinement.

First, the plasma temperature results to be almost constant over the whole confinement volume, at least within the experimental error ($\sim 10\% - 25\%$), suggesting a smooth distribution of every physical quantities related to it. The radial density profile shows a smooth but clear trend, compatible with a confinement gradient towards the internal regions of the plasmoid. In particular, data of ROI 2 shows a slight drop, highlighting the transition region from the plasmoid to the plasma halo, as suggested in *Ivanov et al.*[74]: a 40 % lower density is measured in proximity of the ECR edge, outside of which the X-ray emission flux is almost zero and so the plasma is practically absent.

An extrapolation can be reasonably done to define temperature and density in not directly measurable regions, by extending the ROIs over the respective axis-symmetrical regions, according to the symmetry of the magnetic field inside the ECR surface.

The resulting density map is shown in figure 5.32, highlighting its gradient in a pseudocolor scale.

It is therefore reasonable to identify the ECR surface as a kind of separatrix, i.e. the boundary between two domains separating the plasma core from the rarefied halo.

The RF ignition power results to be released into the small volume of $\sim 2\ cm^3$, enclosed by the ECR surface, giving a power density of $\sim 100\ W/cm^3$ (part of this power is then released into plasma losses).

The comparison of such results with the volumetric ones highlights the limits of the latter, due to the aforementioned difficulty in the deconvolution of plasma and chamber walls contributions. In general, our local estimate of plasma temperatures, at least for the warm component, indicates a lower value than the one estimated by volumetric measurements.

For the sake of comparison, considering the volumetric measurements in Atomki - Debrecen in the $13 - 14\ GHz$ range at 30 $W$, [49], a relevant increase of the density estimates is observed ($3.0 - 5.5 \cdot 10^{16}\ m^{-3}$ in volu-

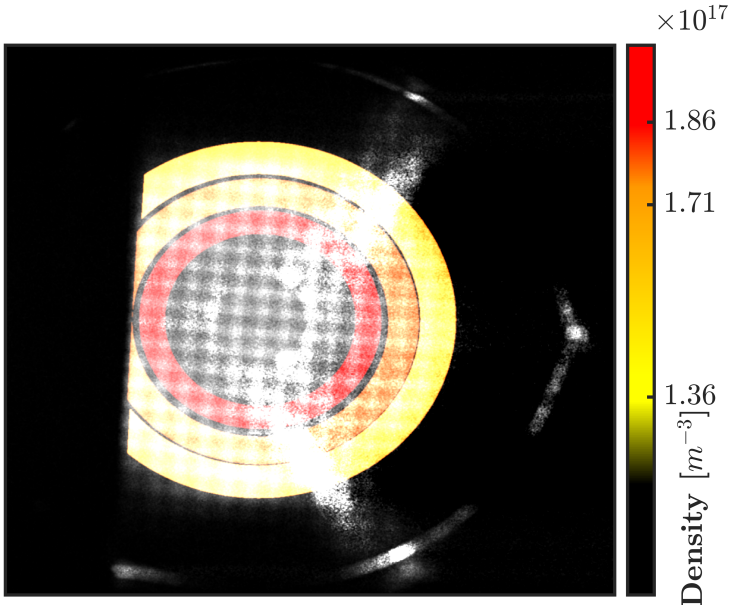


Figure 5.32: Plasma electron density map in pseudo color scale (overlapped on the B-W plasma image), obtained by extrapolating ROI 2, ROI 3 and ROI 4 over respective circular crowns, in the assumption of a spherical symmetry of the system.

metric measurements, compared to $1.4 - 1.9 \cdot 10^{17}\ m^{-3}$, in this work) that could be in principle related with the different ignition power (30 $W$ vs 200 $W$), while the temperature is deemed to be lower than the estimates from volumetric measurements when using the local estimation mode (this paper), despite the higher RF power.

The reason for this latter discrepancy could be linked to the experimental technique. Despite the good collimation in the volumetric measurements, in fact, it could not be excluded that a small contribution to the collected spectra came from the deconfined plasma. This was in fact confirmed by the presence of Fe and Cr fluorescence peaks in the collected spectra.

The present technique can be in principle applied to the measurements shown in the previous sections, although requiring the estimation of the plasma volume in each magnetic configuration.

In general, as a perspective for the Pandora experiments, the results

shown in this section represent a benchmark for the aim of monitoring and mapping the plasma thermodynamics (see section 2.3).

# Conclusions and perspectives

The present thesis has investigated some key-issues of ECR plasma physics, within the framework of the PANDORA project.

Beyond their immediate relevance for the success of PANDORA, the experimental investigations reported here contribute to a broader understanding of plasma dynamics, including gas mixing effects, pulsed transient phenomena, and local thermodynamic properties.

These studies were made possible by the development and application of a dedicated energy- and space-resolved X-ray pin-hole camera diagnostic methodology.

While the technique itself represents a significant advancement, the combination of method and measurement provides new scientific insights into the behavior of magnetically confined plasmas.

The diagnostic allowed detailed probing of plasma confinement structures and emission morphology under several relevant plasma conditions, exploring the elemental mapping of plasma displacement and its time evolution during time-dependent phenomena.

Moreover, the technique has been applied to the extraction of the local thermodynamic parameters of plasma, demonstrating for the first time its potential as a core tool for PANDORA experiment.

Three main categories of experimental results were obtained:

1. **Gas mixing effects:** The measurements confirmed theoretical predictions about the influence of different species on the plasma confinement dynamics. If cross-checked with available literature results on plasma modelling and theory, the experimental findings seem to

be compatible with a direct modification of the potential-dip which is the responsibile of ion confinement in the plasmoid core.

Xe L-line splitting provided the first direct visualization of high-charge-state ion distribution, clarifying the mechanisms behind enhanced extraction in gas-mixing configurations and providing valuable benchmarks for particle-in-cell and double-layer plasma models.

In addition to the relevance for the technique advances and for the ECR plasmas in general, this outcome is particularly promising for PANDORA: it is now validated the approach of monitoring ion distribution in the plasma from different atomic-ionic species, also including the separation/identification of contributions from low vs. high charge state ions.

2. **Time-resolved studies of pulsed plasma transients:** For the first time, the evolution of plasma confinement structures during decay transients was directly observed.

   Differences between confined and deconfined plasma dynamics, afterglow instabilities, and RF-induced scattering effects were observed, offering unique insight into potential-dip and double-layer dynamics that had previously been hypothesized only.

   These new results confirm that the implemented technique is capable of chasing the plasma dynamics in a timescale of 5 msec, which is compatible with X-ray emission transients occurring during turbulent regimes. These turbulences have to be carefully investigated and, then, mitigated, in the future activities of PANDORA commissioning the overall tuning.

3. **Local thermodynamic parameter reconstruction:** Space-resolved mapping of electron density and temperature revealed a nearly uniform temperature distribution and a radial density gradient consistent with the plasmoid-halo structure. These results extend beyond volumetric measurements, providing essential benchmark data for theoretical and computational plasma models, and offering a robust foundation for future PANDORA experiments.

Overall, the combination of these experimental investigations and the diagnostic methodology developed in this work constitutes a significant contribution to the understanding of ECR plasma behavior.

The results not only deepen scientific knowledge about open issues in the physics of ECR ion sources, but also provide essential guidance for the implementation of fully controlled experimental conditions in PANDORA, supporting the project's overarching goal of investigating nuclear processes in ionized media.

Future work will focus on improving temporal resolution for afterglow studies, extending the application of the diagnostics to other ECRIS facilities, and integrating these measurements into advanced simulations, further strengthening the link between laboratory experiments and astrophysically relevant plasma conditions.

# Bibliography


[1] Francis Chen., *Introduction to the Plasma Physics and Controlled Fusion*, second edition ed. (London Press, ADDRESS, 1986).

[2] S. Barbarino and F. Consoli., Moto di una particella carica in campo magnetico (2004).

[3] R. Geller, *Electron Cyclotron Resonance Ion Sources and ECR Plasmas* (J. W. Arrowsmith Ltd, Bristol, UK, ADDRESS, 1996).

[4] M. A. Lieberman. F. Jaeger, A. J. Lichtenberg, Plasma Physics, Pergamon Press **15**, (1972).

[5] B. Mishra, A. Pidatella, S. Biri, A. Galatà, E. Naselli, R. Rácz, G. Torrisi, , and D. Mascali, Physics of Plasmas **102509**, 28 (2021).

[6] H. Kramers, The London, Edinburgh and Dublin Philosophical Magazine and Journal of Science **46:275**, 836–871 (1923).

[7] A. Gumberidze, M. Trassinelli, N. Adrouche, C.I. Szabo, P. Indelicato, F. Haranger, J.-M. Isac, E. Lamour, E.-O. Le Bigot, J. Mérot, C. Prigent, J.-P. Rozet, and D. Vernhet, Rev. Sci. Instrum. **033303**, 81 (2010).

[8] T. Thuillier, J. Benitez, S. Biri, and R. Rácz, Rev. Sci. Instrum. **021102**, 93 (2022).

[9] U. Fantz and O. Tarvainen, Rev. Sci. Instrum. **101601**, 93 (2022).

[10] S. Biri et al., Rev. Sci. Instrum. **83**, 02A341 (2012).

[11] D. Mascali et al., Rev. Sci. Instrum. **095109**, 87 (2016).

[12] E. Takács, B. Radics, C. I. Szabó, S. Biri, L. T. Hudson, J. Imrek, B. Juhász, T. Suta, A. Valek, and J. Pálinkás, Nucl. Instrum. Methods Phys. Res. **B 235**, 120–125 (2005).

[13] M. Anton, Plasma Phys. Control. Fusion **1849**, 38 (1996).

[14] L. Armon McPherson, David J. Ampleford, Christine A. Coverdale, Jeffrey W. Argo, Albert C. Owen, and Deanna M. Jaramillo, Rev. Sci. Instrum. **063502**, 87 (2016).

[15] S. Biri, A. Valek, T. Suta, E. Takács, Cs. Szabó, L. T. Hudson, B. Radics, J. Imrek, B. Juhász, and J. Pálinkás, Rev. Sci. Instrum. **1420**, 75 (2004).

[16] J. Benitez, C. Lyneis, L. Phair, D. Todd, and D. Xie, IEEE Trans. Plasma Sci. **45**, 1746 (2017).

[17] T. Ropponen, O. Tarvainen, I. Izotov, J. Noland, V. Toivanen, G. Machicoane, D. Leitner, H. Koivisto, T. Kalvas, P. Peura, P. Jones, V. Skalyga, and V. Zorin, Plasma Sources Sci. Technol. **055007**, 20 (2011).

[18] B. Isherwood and Guillaume Machicoane, Rev. Sci. Instrum. **025104**, 91 (2020).

[19] Eugenia Naselli, Richard Rácz, Sandor Biri, Maria Mazzaglia, Luigi Celona, Santo Gammino, Giuseppe Torrisi, Zoltan Perduk, Alessio Galatà, and David Mascali, Condens. Matter **7(1)**, 5 (2022).

[20] D. Mascali et al., European Physical Journal A **53**, (2017).

[21] D. Mascali et al., Universe **8(2)**, 80 (2022).

[22] D. Kasen et al., Nature **551**, 80 (2017).

[23] I. Arcavi et al., Nature **551**, 64 (2017).

[24] F. Bosch et al., Phys. Rev. Lett. **5190**, 77 (1996).

[25] Y. Litvinov et al., Rep. Progr. Phys. 74 (2011).

[26] Takahashi et al., Phys Rev C 36 (1987).

[27] J. N. Bahcall et al., Phys Rev. **124**, 495 (1961).

[28] E. Naselli et al., Front. Phys. **10:935728**, (2022).

[29] E. Naselli et al., Universe **11**, 195 (2025).

[30] D. Mascali et al., EPJ Web Conf. **227**, 01013 (2020).

[31] BP Abbott et al., Phys. Rev. Lett. **119**, 161101 (2017).

[32] E. Naselli, D. Mascali, S. Biri, C. Caliri, G. Castro, L. Celona, L.G. Cosentino, A. Galatà, S. Gammino, M. Giarrusso, F. Leone, M. Mazzaglia, R. Rácz, R. Reitano, F.P. Romano, and G. Torrisi, JINST **C10008**, 14 (2019).

[33] R. G. Gratton et al., Experimental Astronomy **12**, 107 (2001).

[34] M. Giarrusso et al., Journal of Instrumentation **13**, C11020 (2018).

[35] A. Pidatella et al., Frontiers in Astronomy and Space Sciences **9**, 931744 (2022).

[36] S. Tsikata et al., Frontiers in Astronomy and Space Sciences **9**, 936532 (2022).

[37] D. Mascali et al., J. Instrum. **12**, C12047 (2017).

[38] A. Goasduff et al., Front. Phys. **10**, 936081 (2022).

[39] A.G. Shalashov et al., Phys. Plasmas **24**, 032111 (2017).

[40] I. Izotov et al., Plasma Sources Sci. Technol. **24**, 045017 (2015).

[41] G. Torrisi et al., Front. Astron. Space Sci. **9**, 949920 (2022).

[42] D. Mascali et al., Condens.Matter **9**, 28 (2024).

[43] I. Izotov, O. Tarvainen, V. Skalyga, D. Mansfeld, T. Kalvas, H. Koivisto, and R. Kronholm, Plasma Sources Sci. Technol. **025012**, 27 (2018).

[44] K. Bernhardi and K. Wiesemann, Rev Sci Instrum. **02A337**, 83(2) (2012).

[45] R. Racz et al., Plasma Sources Sci. Technol. **26**, 075011 (2017).

[46] E. Naselli et al., Condens. Matter **7(1)**, 5 (2022).

[47] E. Naselli, , R. Rácz, S. Biri, M. Mazzaglia, A. Galatà, L. Celona, S. Gammino, G. Torrisi, and D. Mascali, JINST **C10009**, 17 (2022).

[48] D. Mascali, E. Naselli, R. Rácz, S. Biri, L. Celona, A. Galatà, S. Gammino, M. Mazzaglia, and G. Torrisi, Plasma Phys. Control. Fusion **035020**, 64 (2022).

[49] D. Mascali, G. Castro, S. Biri, R. Rácz, J. Pálinkás, C. Caliri, L. Celona, L. Neri, F. P. Romano, G. Torrisi, and S. Gammino, Review of Scientific Instruments **02A510**, 87 (2016).

[50] A. G. Drentje et al., Phys. Res. B **9**, 526 (1985).

[51] A. G. Drentje et al., Rev. Sci. Instrum. **74**, 2631 (2003).

[52] G. D. Shirkhov et al., Plasma Sources Sci. Technol. **2**, 250 (1993).

[53] T. A. Antaya et al., Rev. Sci. Instrum. **65**, 2947 (1994).

[54] A. G. Drentje et al., Rev. Sci. Instrum. **63**, 2875 (1992).

[55] A. G. Drentje et al., Rev. Sci. Instrum. **67(3)**, 953–955 (1996).

[56] D. R. Whaley et al., Physics of Fluids B: Plasma Physics **2**, 1195 (1990).

[57] G. Melin et al., Journal of Applied Physics **86**, 4772 (1999).

[58] V. Mironov et al., Physical Review Accelerators and Beams **20**, 013402 (2017).

[59] D. Mascali et al., Review of Scientific Instruments **85**, 02A511 (2014).

[60] A. G. Dimonte et al., Physical Review Letters **48**, 1352 (1982).

[61] A. A. Ivanov and K. Wiesemann, IEEE Transactions on Plasma Science **33**, 1743 (2005).

[62] T. Nakagawa, Y. Higurashi, M. Kidera, A. Efremov, V. Mironov, and G. Shirkov, in *Proceedings of the Workshop on the Production of Intense Beams of Highly Charged Ions (PIBHI2000)*, edited by Italian Physical Society (PUBLISHER, Bologna, 2001), p. 105, catania, Italy, 2000.

[63] O. Tarvainen et al., Plasma Physics and Controlled Fusion **67**, 035012 (2025).

[64] G. Melin et al., Review of Scientific Instruments **61**, 236 (1990).

[65] O. Tarvainen et al., Plasma Sources Science and Technology **19**, 045027 (2010).

[66] E. Naselli et al., Plasma Sources Science and Technology **28(8)**, 085021 (2019).

[67] G. Finocchiaro et al., Physics of Plasmas **31**, 062506 (2024).

[68] Glenn F. Knoll, *Radiation Detection and Measurement*, 3rd ed. (Wiley, New York, 2000), pp. xiv+802.

[69] James R. Janesick, *Scientific Charge-Coupled Devices* (SPIE Press, Bellingham, WA, 2001), comprehensive reference on CCD physics and applications.

[70] F. P. Romano et al., Analytical Chemistry **86(21)**, 10892 (2014).

[71] Ville Toivanen et al., Journal of Physics: Conference Series **2743**, 012047 (2024).

[72] A.C. Thompson, J. Kirz, D.T. Attwood, E.M. Gullikson, Y. Liu, et al., X-Ray Data Booklet, 2001, second edition, revised and updated.

[73] H.-K. Chung, M. H. Chen, W. L. Morgan, Y. Ralchenko, and R. W. Lee, High Energy Density Physics **1**, 3 (2005).

[74] A. A. Ivanov and K. Wiesemann, IEEE Trans. Plasma Sci. **33**, 1743 (2005).